# 論文 / 著書情報
# Article / Book Information

| | |
|---|---|
| 題目(和文) | 単一高分子薬物キャリアの設計と合成および癌標的治療への応用 |
| Title(English) | Design and Synthesis of Self-folding Macromolecular Drug Carriers and their Biological Applications for Tumor-directed Treatment |
| 著者(和文) | GaoShan |
| Author(English) | Shan Gao |
| 出典(和文) | 学位:博士(工学),<br>学位授与機関:東京工業大学,<br>報告番号:甲第12769号,<br>授与年月日:2024年3月26日,<br>学位の種別:課程博士,<br>審査員:西山 伸宏,三浦 裕,北本 仁孝,田中 克典,神谷 真子,岡田 智 |
| Citation(English) | Degree:Doctor (Engineering),<br>Conferring organization: Tokyo Institute of Technology,<br>Report number:甲第12769号,<br>Conferred date:2024/3/26,<br>Degree Type:Course doctor,<br>Examiner:,,,,, |
| 学位種別(和文) | 博士論文 |
| Type(English) | Doctoral Thesis |

博士論文

# 単一高分子薬物キャリアの設計と合成および癌標的治療への応用

# Design and Synthesis of Self-folding Macromolecular Drug Carriers and their Biological Applications for Tumor-directed Treatment

**Gao Shan**

東京工業大学 西山· 三浦研究室

# 目次

# *List of abbreviations*

AIBN: 2,2′-azobis(2-methylpropionitrile)

ATRP: atom transfer radical polymerization

BNCT: boron neutron capture therapy

BSA: bovine serum albumin

BZA: benzyl acrylate

BZA/PEGA: quantity ratios of hydrophobic segments to hydrophilic segments

CEA: 2-carboxyethyl acrylate

CMC: critical micelle concentration

CTA: chain transfer agent

DA: degree of aggregation

DDMAT: 2-(dodecylthiocarbonothioylthio)-2-methylpropionic acid

DDS: drug delivery system

DLS: dynamic light scattering

DMF: *N*,*N*-dimethylformamide

DMT-MM: 4-(4,6-dimethoxy-1,3,5-triazin-2-yl)-4-methyl-morpholinium chloride

DP: degree of polymerization

EPR: enhanced permeability and retention

$GdCl_3 \cdot 6H_2O$: gadolinium trichloride hexahydrate

Gd-DOTA: gadolinium chelated tetraxetan

Gd-NCT: gadolinium neutron capture therapy

GPC: gel permeation chromatography

ICP-MS: inductively coupled plasma mass spectrometry

i.v.: intravenous

MCR: mean count rate

MRI: magnetic resonance imaging

NCT: neutron capture therapy

NMP: nitroxide mediated polymerization

NMR: nuclear magnetic resonance

PBS: phosphate-buffered saline

PDI: polydispersity index

PEGA: poly (ethylene glycol) methyl ether acrylate

*p*-$NH_2$-Bn-DOTA-*t*-Bu: s-2-(4-Aminobenzyl)-1,4,7,10-tetraazacyclododecane tetra-*tert*-butylacetate

RAFT: reversible addition fragmentation chain transfer

SAXS: small angle X-ray scattering

SCPNs: single chain polymeric nanoparticles

SEC-MALS: Size-exclusion chromatography coupled to multi-angle light scattering

SMDC: self-folding macromolecular drug carrier

SMDC-Gd: Gd-DOTA loaded SMDC

TFA: trifluoroacetic acid

TMS: tetramethylsilane

TEM: transmission electron microscope

%ID/g: percentage injection dose per gram.

%ID/mL: percentage injection dose per milliliter.

# Chapter 1. Introduction

## 1.1 Background

The drug delivery system (DDS) refers to a drug-based system (formulation or device) designed to transport drugs to the specific site of a disease [1]. This system finds applications in diagnosing and treating various diseases like cancer and cardiovascular disease. Its primary objective is to modify the pharmacokinetics and specificity of drugs, ultimately improving bioavailability, drug efficacy, safety, convenience, and patient compliance [2-3]. The tumor-targeting is an essential clinical application of DDS, with its effectiveness often attributed to the enhanced permeability and retention (EPR) effect in tumor tissues [4-5]. To elaborate, tumor tissues exhibit abundant newly formed blood vessels that differ significantly in structure from vessels in normal tissues. Notably, this difference manifest as large intercellular spaces in the tumor vessel wall, enabling the passage of nanoparticles that would otherwise be hindered in normal tissues. This phenomenon facilitates targeted accumulation of nanosized particles or micelles in tumors (**Figure 1.1**) [6-7].

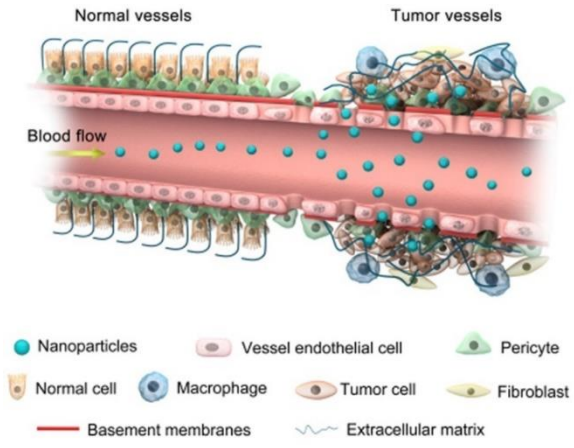


**Figure 1.1**. Schematic diagram of the EPR effect [6].

Presently, a multitude of tumor-targeting DDSs has emerged, employing diverse materials such as polymers, liposomes, metals, carbon nanotubes, and nanogels [8]. Among DDSs constructed from these materials, drug-loaded polymeric micelles stand out as extensively developed and applied, showcasing exceptional performance in cancer imaging and therapy [9]. These micelles achieve heightened biocompatibility by using suitable hydrophilic polymer segments, notably polyethylene glycol (PEG), as the outer shell, while performing a high drug loading capacity by encapsulating drugs in the core [10]. Furthermore, polymeric micelles enhance their tumor-targeting abilities by incorporating additional site-specific functional segments during synthesis [11].

During the development of polymeric micelles as tumor-targeting DDSs for cancer, particularly those administered via intravenous (i.v.) injection, the micelle size is the crucial design and control parameter. Typically, the size should be maintained within the range of 5 to 100 nanometers. The upper size limit of 100 nm is derived from the upper critical size of the EPR effect in tumor tissues, especially in poorly permeable solid tumors. Only micelles smaller than this threshold are guaranteed to benefit from the EPR effect [12-13]. On the other hand, the lower size limit of 5 nm is dictated by the upper critical size of the glomerular multiple-layer filtration structure during renal excretion. Micelles larger than this size can evade rapid excretion, ensuring they are transported to the tumor before elimination [14]. Within the size range of 5-100 nm, current research findings suggest that smaller sizes enhance penetration of polymeric drug carriers into tumor tissues [15].

Contemporary polymeric drug carriers commonly adopt a shell-core micellar structure, where drugs are encapsulated within the core, and multiple polymer molecules assemble to form the micellar shell (**Figure 1.2**) [16-17]. This structure, however, presents two limitations when applied as a DDS: one concerns size minimization, and the other involves the critical micelle concentration (CMC). Concerning size minimization, the current polymeric micellar structure tends to yield final sizes typically ranging from

20 to 100 nm, posing challenges in reducing them to the optimal range of 5 to 10 nm for improved tumor penetration [18-19]. As for the issue of CMC, micelles undergo degradation and release polymer chains and drug particles when the micelle concentration falls below the CMC value. This process is beneficial for the degradation of large-sized micelles and prevents prolonged retention in the body [20]. However, the concentration of polymeric micelles in the systemic circulation remains consistently low, making it susceptible to dropping below the CMC. Consequently, micelles may prematurely degrade and release the drug before reaching the targeted tumor, impacting drug delivery efficiency.

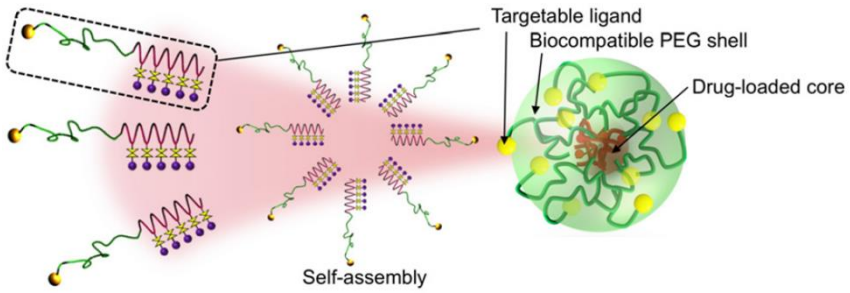


**Figure 1.2**. Shell-core structure of polymeric micelles [9].

While the efficacy of EPR effect has been questioned in certain clinical applications [21-22], EPR-based DDSs still suggested ongoing potential based on the observed and confirmed experimental tumor-targeted penetration and accumulation behavior. Hence, addressing the limitations of the polymeric micelles utilized as DDSs remains a valuable avenue for research, aiming to enhance their performance in clinical cancer diagnosis and treatment.

## 1.2 Purpose and method

To overcome the limitations of polymeric micelles as tumor-targeting DDS, a novel self-folding macromolecular drug carrier (SMDC) structure is proposed for cancer

imaging and therapy. As shown in **Figure 1.3**, the designed macromolecule comprises random hydrophilic segments, hydrophobic segments, and drug-loaded segments. This macromolecule was expected to autonomously form an SMDC through intramolecular self-folding. The size of this SMDC is meticulously controlled within the range of 5 to 10 nm, aiming to exploit the EPR effect and avoid rapid renal excretion, and more importantly, achieve exceptional tumor penetration. Moreover, due to its unique structure, this SMDC does not exhibit a CMC, enabling it to facilitate relatively prolonged and targeted delivery to the tumor site.

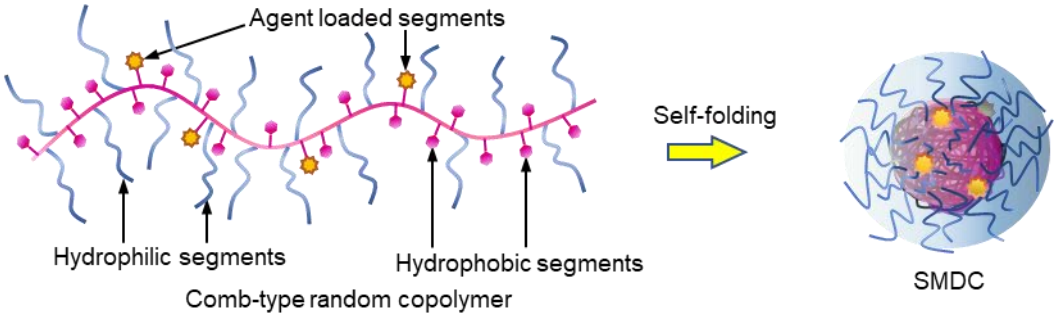


**Figure 1.3**. Structure and formation of SMDC.

To achieve the designation and preparation of the intended SMDC and its utilization in cancer imaging and therapy, the research will proceed according to the following methodology:

(1) Macromolecules intended for SMDC formation are synthesized using reversible addition fragmentation chain transfer (RAFT) polymerization. The reaction kinetics are scrutinized to ensure product quality control.

(2) The relationship between polymer parameters (degree of polymerization and ratio between segments) and SMDC forming conditions (size and degree of aggregation) is elucidated. Subsequently, gadolinium chelate-loaded SMDC (SMDC-Gd) is prepared and characterized.

(3) *In vitro* and *in vivo* properties (cytotoxicity, biotoxicity, and biodistribution) of

SMDC-Gd are clarified, serving as the foundation for selecting parameters in practical application.

(4) To assess the architecture of SMDC and predict the performance of SMDC-Gd enhanced MRI, the relaxivity of SMDC-Gd is measured, and the corresponding improvement mechanism is discussed. Consequently, SMDC-Gd is employed in magnetic resonance imaging (MRI) on tumor-bearing mice to investigate the feasibility and performance of SMDC-Gd in cancer imaging.

(5) SMDC-Gd is utilized in gadolinium neutron capture therapy (Gd-NCT) on tumor-bearing mice to investigate the feasibility of SMDC-Gd in cancer therapy.

## 1.3 References

[1] Liu D, Yang F, Xiong F, Gu N. The smart drug delivery system and its clinical potential. Theranostics, **2016**, 6(9): 1306.

[2] Matoba T, Koga J, Nakano K, Egashira K, Tsutsui H. Nanoparticle-mediated drug delivery system for atherosclerotic cardiovascular disease. Journal of cardiology, **2017**, 70(3): 206-211.

[3] Wilhelm S, Tavares AJ, Dai Q, Ohta S, Audet J, Dvorak HF, Chan WC. Analysis of nanoparticle delivery to tumours. Nature reviews materials. **2016**, 1(5): 1-12.

[4] Wang AZ, Langer R, Farokhzad OC. Nanoparticle delivery of cancer drugs. Annual review of medicine, **2012**, 63: 185-198.

[5] Cho K, Wang XU, Nie S, Chen Z, Shin DM. Therapeutic nanoparticles for drug delivery in cancer. Clinical cancer research, **2008**, 14(5): 1310-1316.

[6] Abdalla AME, Xiao L, Ullah MW, Yu M, Ouyang C, Yang G. Current challenges of cancer anti-angiogenic therapy and the promise of nanotherapeutics. Theranostics, **2018**, 8(2): 533.

[7] Hashida M. Advocation and advancements of EPR effect theory in drug delivery science: A commentary. Journal of Controlled Release, **2022**, 346: 355-357.

[8] Senapati S, Mahanta AK, Kumar S, Maiti P. Controlled drug delivery vehicles for

cancer treatment and their performance. Signal transduction and targeted therapy, **2018**, 3(1): 1-19.

[9] Nishiyama N, Matsumura Y, Kataoka K. Development of polymeric micelles for targeting intractable cancers. Cancer science, **2016**, 107(7): 867-874.

[10] Overchuk M, Zheng G. Overcoming obstacles in the tumor microenvironment: Recent advancements in nanoparticle delivery for cancer theranostics. Biomaterials, **2018**, 156: 217-237.

[11] Li J, Kataoka K. Chemo-physical strategies to advance the *in vivo* functionality of targeted nanomedicine: the next generation[J]. Journal of the American Chemical Society, **2020**, 143(2): 538-559.

[12] Cabral H, Matsumoto Y, Mizuno K, Chen Q, Murakami M, Kimura M, Terada Y, Kano MR, Miyazono K, Uesaka M, Nishiyama N, Kataoka K. Accumulation of sub-100 nm polymeric micelles in poorly permeable tumours depends on size. Nature nanotechnology, **2011**, 6(12): 815-823.

[13] Majumder N, Das NG, Das SK. Polymeric micelles for anticancer drug delivery. Therapeutic delivery, **2020**, 11(10): 613-635.

[14] Du B, Jiang X, Das A, Zhou Q, Yu M, Jin R, Zheng J. Glomerular barrier behaves as an atomically precise bandpass filter in a sub-nanometre regime. Nature nanotechnology, **2017**, 12(11): 1096-1102.

[15] Dreher MR, Liu W, Michelich CR, Dewhirst MW, Yuan F, Chilkoti A. Tumor vascular permeability, accumulation, and penetration of macromolecular drug carriers. Journal of the National Cancer Institute, **2006**, 98(5): 335-344.

[16] Ghosh B, Biswas S. Polymeric micelles in cancer therapy: State of the art[J]. Journal of Controlled Release, **2021**, 332: 127-147.

[17] Ghezzi M, Pescina S, Padula C, Santi P, Del Favero E, Cantù L, Nicoli S. Polymeric micelles in drug delivery: An insight of the techniques for their characterization and assessment in biorelevant conditions. Journal of Controlled Release, **2021**, 332: 312-336.

[18] Hwang D, Ramsey JD, Kabanov AV. Polymeric micelles for the delivery of poorly

soluble drugs: From nanoformulation to clinical approval. Advanced drug delivery reviews, **2020**, 156: 80-118.

[19] Bagheri M, Bresseleers J, Varela-Moreira A, Sandre O, Meeuwissen SA, Schiffelers RM, Metselaar JM, van Nostrum CF, van Hest JCM, Hennink WE. effect of formulation and processing parameters on the size of mPEG-b-p (HPMA-Bz) polymeric micelles. Langmuir, **2018**, 34(50): 15495-15506.

[20] Lu Y, Yue Z, Xie J, Wang W, Zhu H, Zhang E, Cao Z. Micelles with ultralow critical micelle concentration as carriers for drug delivery. Nature biomedical engineering, **2018**, 2(5): 318-325.

[21] Nichols JW, Bae YH. EPR: Evidence and fallacy. Journal of Controlled Release, **2014**, 190: 451-464.

[22] Danhier F. To exploit the tumor microenvironment: Since the EPR effect fails in the clinic, what is the future of nanomedicine? Journal of Controlled Release, **2016**, 244: 108-121.

# Chapter 2. RAFT polymerization of macromolecules for SMDC formation

## 2.1 Introduction

Living radical polymerization is a widely employed polymerization method in both research and production due to its effectiveness in controlling the structure and quality of polymer products [1]. Depending on the utilized monomers and specific product requirements, this method encompasses atom transfer radical polymerization (ATRP), nitroxide mediated polymerization (NMP), and reversible addition fragmentation chain transfer (RAFT) polymerization methods [2-4]. Given that the polymers designed in my research are random copolymers and random terpolymers with controllable types and quantities of monomers, RAFT polymerization emerges as the most suitable method. This approach involves the use of a chain transfer agent (CTA) in the form of a thiocarbonylthio compound to regulate the molecular weight and polydispersity index (PDI) generated during the process of living radical polymerization [5]. In the case of homopolymers, the present findings indicate that the PDI generally decreases with the increase of conversion [6]. Conversely, for copolymers, the PDI may sometimes increase with the increase of conversion due to the distinct characteristics of the two or more monomers and the elevated viscosity of reaction mixture [7]. Consequently, maintaining control of stability and PDI should be crucial in the context of a designed RAFT polymerization.

In this research, a series of random copolymers with hydrophilic segments and hydrophobic segments will be synthesized through RAFT polymerization to serve as the backbone of SMDC. Poly (ethylene glycol) methyl ether acrylate (PEGA) is chosen as

the monomer for the hydrophilic segments and benzyl acrylate (BZA) is selected as the monomer for the hydrophobic segments. The research focuses on investigating the controllability of the reaction process and ensuring product quality. Furthermore, random terpolymers are polymerized, and similar investigations into the controllability of the reaction process and product quality are conducted. In these terpolymers, varying amounts of 2-carboxyethyl acrylate (CEA) are employed in place of PEGA in synthetic route of copolymer backbone to incorporate gadolinium chelated tetraxetan (Gd-DOTA) into the macromolecules. These macromolecules serve as candidates for dual use as the imaging agent in MRI and therapeutic agent in Gd-NCT.

## 2.2 Materials and methods

### 2.2.1 Materials

Poly (ethylene glycol) methyl ether acrylate (PEGA, $M_n$ = 480 g/mol), 2-carboxyethyl acrylate (CEA), and 2-(dodecylthiocarbonothioylthio)-2-methylpropionic acid (DDMAT) were purchased from Sigma-Aldrich Corporation (ST. Louis, Missouri, USA). 2,2′-Azobis(2-methylpropionitrile) (AIBN), *N*,*N*-dimethylformamide (DMF), and toluene were purchased from Fujifilm Wako Pure Chemical Corporation (Osaka, Japan). Benzyl acrylate (BZA) was purchased from Tokyo Chemical Industry Co., Ltd. (Tokyo, Japan). Before utilization, PEGA was purified by aluminum oxide-packed column funnel to remove the inhibitor and degassed by five vacuum and argon backfill cycles. CEA was purified by an inhibitor remover prepacked column 30631-2 (Sigma-Aldrich Corporation, St. Louis, Missouri, USA) and degassed by five vacuum and argon backfill cycles. AIBN was purified by recrystallisation and dried by vacuum. BZA, DMF, and toluene were purified by vacuum distillation. Other reagents and solvents were used as received.

### 2.2.2 Analysis

The $^1$H nuclear magnetic resonance (NMR) spectra were recorded using a Bruker biospin AVANCE III 400A (400 MHz) (Bruker Corporation, Billerica, Massachusetts, USA) instrument with $CDCl_3$, $D_2O$, and DMSO-$d_6$ containing tetramethylsilane (TMS)

as the internal standard. GPC was performed at 40 °C using a JASCO Extrema HPLC system (LC-Net II/ADC, Co-4060, AS-4050, PU-4180, UV-4070, and RI-4030, JASCO Corporation, Tokyo, Japan) equipped with a TSKgel α-2500 column (linear, 7.8 mm × 300 mm; pore size, 2.5 nm; bead size, 7 μm; exclusion limit, $1 \times 10^4$ g/mol, Tosoh Corporation, Tokyo, Japan), a TSKgel α-4000 column (linear, 7.8 mm × 300 mm; pore size, 45 nm; bead size, 10 μm; exclusion limit, $1 \times 10^6$ g/mol, Tosoh Corporation, Tokyo, Japan), and TSKgel guardcolumn-α guard column (Tosoh Corporation, Tokyo, Japan) in DMF containing lithium bromide (10 mM) at a flow rate of 1.0 mL/min. Data were analyzed using JASCO ChromNAV ver. 2.04.03 (JASCO Corporation, Tokyo, Japan).

### 2.2.3 Typical polymerization procedure

2.2.3.1 Synthesis of $BZA_m$-$PEGA_n$ (**P1-P20**)

For the synthesis of $BZA_{50}$-$PEGA_{50}$ (**P3**), all manipulations of the air-sensitive materials were performed with the rigorous exclusion of oxygen and moisture in flame- or oven-dried glassware on a high vacuum-line or in an argon-filled gas recycle purification system equipped a glovebox (DBO-1.5KH-TSO, Miwa Manufacturing Co., Ltd., Osaka, Japan). The synthetic route is shown in **Scheme 2.1**. A mixture of AIBN (0.5 mg, 0.003 mmol) and DDMAT (2.2 mg, 0.006 mmol) in dry toluene (1 mL) was added into the polymerization test tube equipped with a magnetic stirring bar in the glovebox. BZA (48.7 mg, 0.3 mmol) and PEGA (144.0 mg, 0.3 mmol) were added into the test tube, and polymerization was then started in a 70 °C oil bath and continued for 16 h. The polymerization reaction was terminated by liquid nitrogen. The conversion was confirmed by $^1$H NMR. The product was purified by dialysis (Spectra/Por dialysis membrane, MWCO of 6-8 kD) against methanol and Milli-Q water. After lyophilization, the obtained $BZA_{50}$-$PEGA_{50}$ was analyzed by $^1$H NMR (**Figure 2.1**), GPC and SEC-MALS. $^1$H NMR ($CDCl_3$ with 0.03% TMS, 400 MHz): $\delta$ (ppm) = 0.88 (*t*, 3H, -S-$CH_2$-$(CH_2)_{10}$-C$\underline{H}_3$), 1.10-1.29 (*m*, 20H, -S-$CH_2$-(C$\underline{H}_2$)$_{10}$-$CH_3$), 1.33-1.99 (*m*, 206H, -(C$\underline{H}_2$-CH(BZA segment))$_{50}$-, -(C$\underline{H}_2$-CH(PEGA segment))$_{50}$-, (C$\underline{H}_3$)$_2$-C(COOH)-), 2.19-2.53 (*m*, 100H, -($CH_2$-C$\underline{H}$(BZA segment))$_{50}$-, -($CH_2$-C$\underline{H}$(PEGA segment))$_{50}$-), 3.31-3.40 (*m*,

152H, -$CH_2$-$CH_2$-O-($CH_2$-$CH_2$-O)$_8$-C$\underline{H}_3$, -S-C$\underline{H}_2$-($CH_2$)$_{10}$-$CH_3$), 3.42-3.74 (*m*, 1700H, -$CH_2$-C$\underline{H}_2$-O-(C$\underline{H}_2$-C$\underline{H}_2$-O)$_8$-$CH_3$), 3.90-4.35 (*m*, 100H, -C$\underline{H}_2$-$CH_2$-O-($CH_2$-$CH_2$-O)$_8$-$CH_3$), 4.81-5.16 (*m*, 100H, -COO-C$\underline{H}_2$-$C_6H_5$), 7.17-7.40 (*m*, 250H, -COO-$CH_2$-$C_6\underline{H}_5$). Conv.,$_{BZA}$ = 96.0 %, Conv.,$_{PEGA}$ = 92.0 %, $M_{n,NMR}$ = 30,200 g/mol, $M_w/M_n$ = 1.82.

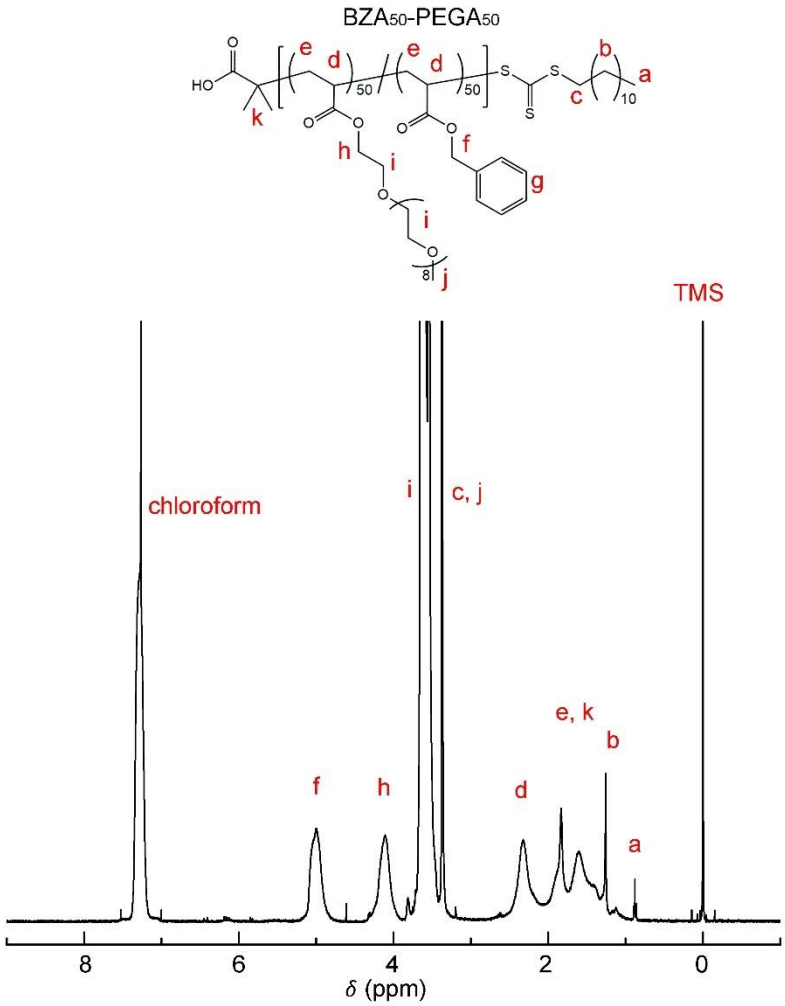


**Figure 2.1**. $^1$H NMR spectrum of $BZA_{50}$-$PEGA_{50}$ in chloroform-*d* at 25 °C.

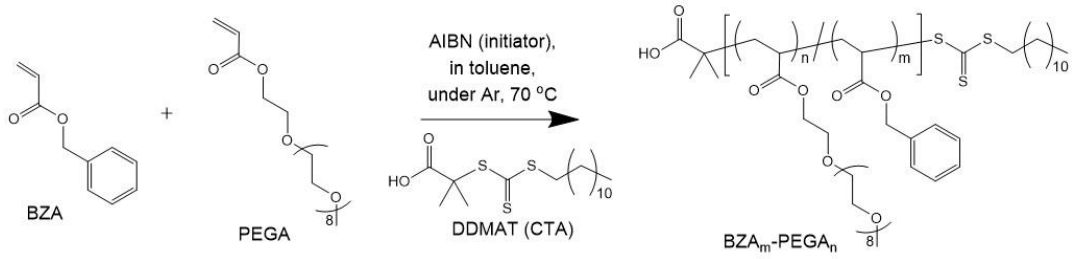


**Scheme 2.1**. Synthesis of $BZA_m$-$PEGA_n$ (**P1**-**P20**) using RAFT polymerization.

2.2.3.2 Synthesis of $BZA_m$-$CEA_k$

The procedure of $BZA_{24}$-$CEA_{36}$ synthesis is shown in **Scheme 2.2**. A mixture of AIBN (0.5 mg, 0.003 mmol) and DDMAT (2.2 mg, 0.006 mmol) in dry DMF (1 mL) was added into the polymerization test tube equipped with a magnetic stirring bar in the glovebox. BZA (38.9 mg, 0.24 mmol) and CEA (51.9 mg, 0.36 mmol) were added into the test tube, and polymerization was then started in a 70 °C oil bath and continued for 20 min. The polymerization reaction was terminated by liquid nitrogen. The product was purified by dialysis (Spectra/Por dialysis membrane, MWCO of 3.5 kD) against methanol and Milli-Q water. After lyophilization, the obtained $BZA_{40}$-$CEA_{60}$ and conversion were analyzed by $^1$H NMR (**Figure 2.2**). $^1$H NMR (DMSO-$d_6$ with 0.03% TMS, 400 MHz): $\delta$ (ppm) = 0.88 (*t*, 3H, -S-$CH_2$-$(CH_2)_{10}$-C$\underline{H}_3$), 1.01-1.29 (*m*, 20H, -S-$CH_2$-(C$\underline{H}_2$)$_{10}$-$CH_3$), 1.33-1.99 (*m*, 126H, -(C$\underline{H}_2$-CH(BZA segment))$_m$-, -(C$\underline{H}_2$-CH(CEA segment))$_k$-, (C$\underline{H}_3$)$_2$-C(COOH)-), 2.18-2.47 (*m*, 60H, -($CH_2$-C$\underline{H}$(BZA segment))$_m$-, -($CH_2$-C$\underline{H}$(CEA segment))$_k$-), 2.49-2.75 (*m*, 72H, -COO-$CH_2$-C$\underline{H}_2$-COOH), 3.30 (*d*, 2H, -S-C$\underline{H}_2$-$(CH_2)_{10}$-$CH_3$), 3.80-4.60 (*m*, 72H, -COO-C$\underline{H}_2$-$CH_2$-COOH), 4.72-5.19 (*m*, 48H, -COO-C$\underline{H}_2$-$C_6H_5$), 7.08-7.38 (*m*, 120H, -COO-$CH_2$-$C_6\underline{H}_5$). Conv.,$_{BZA}$ = 64.1 %, Conv.,$_{CEA}$ = 61.0 %, $M_{n,NMR}$ = 9,600 g/mol.

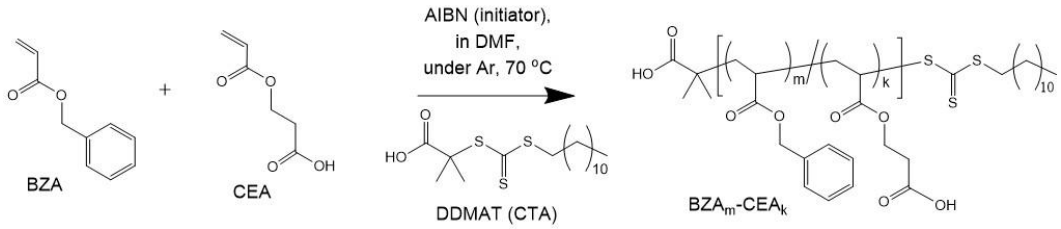


**Scheme 2.2**. Synthesis of $BZA_m$-$CEA_k$ using RAFT polymerization.

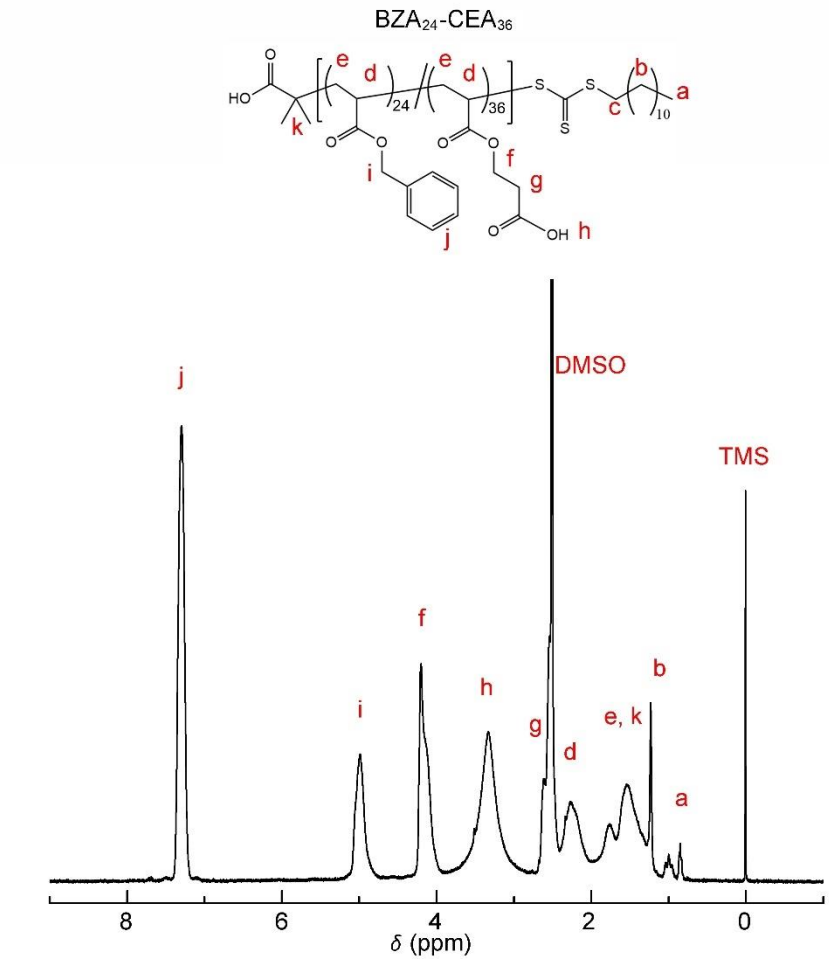


**Figure 2.2**. $^1$H NMR spectrum of $BZA_{24}$-$CEA_{36}$ in DMSO-$d_6$ at 25 °C.

2.2.3.3 Synthesis of $PEGA_n$-$CEA_k$

The procedure of $PEGA_{100}$-$CEA_{100}$ synthesis is shown in **Scheme 2.3**. A mixture of AIBN (0.5 mg, 0.003 mmol) and DDMAT (2.2 mg, 0.006 mmol) in dry DMF (1 mL) was added into the polymerization test tube equipped with a magnetic stirring bar in the

glovebox. PEGA (432.0 mg, 0.90 mmol) and CEA (129.7 mg, 0.90 mmol) were added into the test tube, and polymerization was then started in a 70 °C oil bath and continued for 20 min. The polymerization reaction was terminated by liquid nitrogen. The product was purified by dialysis (Spectra/Por dialysis membrane, MWCO of 6-8 kD) against methanol and Milli-Q water. After lyophilization, the obtained $PEGA_{100}$-$CEA_{100}$ and conversion were analyzed by $^1$H NMR (**Figure 2.3**). $^1$H NMR (DMSO-$d_6$ with 0.03% TMS, 400 MHz): $\delta$ (ppm) = 0.88 (*t*, 3H, -S-$CH_2$-$(CH_2)_{10}$-C$\underline{H}_3$), 1.07-1.31 (*m*, 20H, -S-$CH_2$-(C$\underline{H}_2$)$_{10}$-$CH_3$), 1.33-2.02 (*m*, 406H, -(C$\underline{H}_2$-CH(PEGA segment))$_n$-, -(C$\underline{H}_2$-CH(CEA segment))$_k$-, (C$\underline{H}_3$)$_2$-C(COOH)-), 2.08-2.58 (*m*, 200H, -($CH_2$-C$\underline{H}$(PEGA segment))$_n$-, -($CH_2$-C$\underline{H}$(CEA segment))$_k$-), 2.59-2.77 (*m*, 200H, -COO-$CH_2$-C$\underline{H}_2$-COOH), 3.31-3.40 (*m*, 302H, -$CH_2$-$CH_2$-O-($CH_2$-$CH_2$-O)$_8$-C$\underline{H}_3$, -S-C$\underline{H}_2$-$(CH_2)_{10}$-$CH_3$), 3.42-3.74 (*m*, 3400H, -$CH_2$-C$\underline{H}_2$-O-(C$\underline{H}_2$-C$\underline{H}_2$-O)$_8$-$CH_3$), 3.98-4.47 (*m*, 400H, -C$\underline{H}_2$-$CH_2$-O-($CH_2$-$CH_2$-O)$_8$-$CH_3$, -COO-C$\underline{H}_2$-$CH_2$-COOH). Conv.,$_{PEGA}$ = 70.1 %, Conv.,$_{CEA}$ = 69.7 %, $M_{n,NMR}$ = 64,400 g/mol.

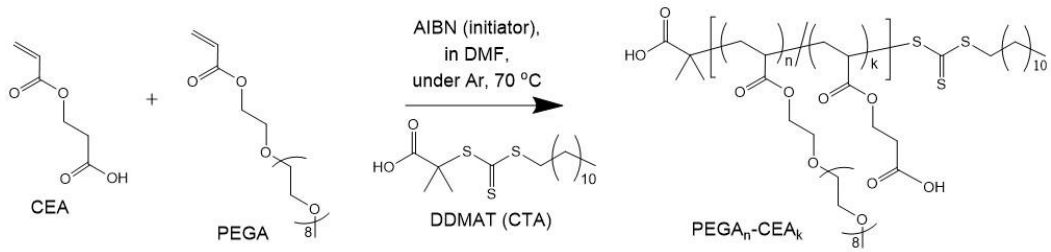


**Scheme 2.3**. Synthesis of $PEGA_n$-$CEA_k$ using RAFT polymerization.

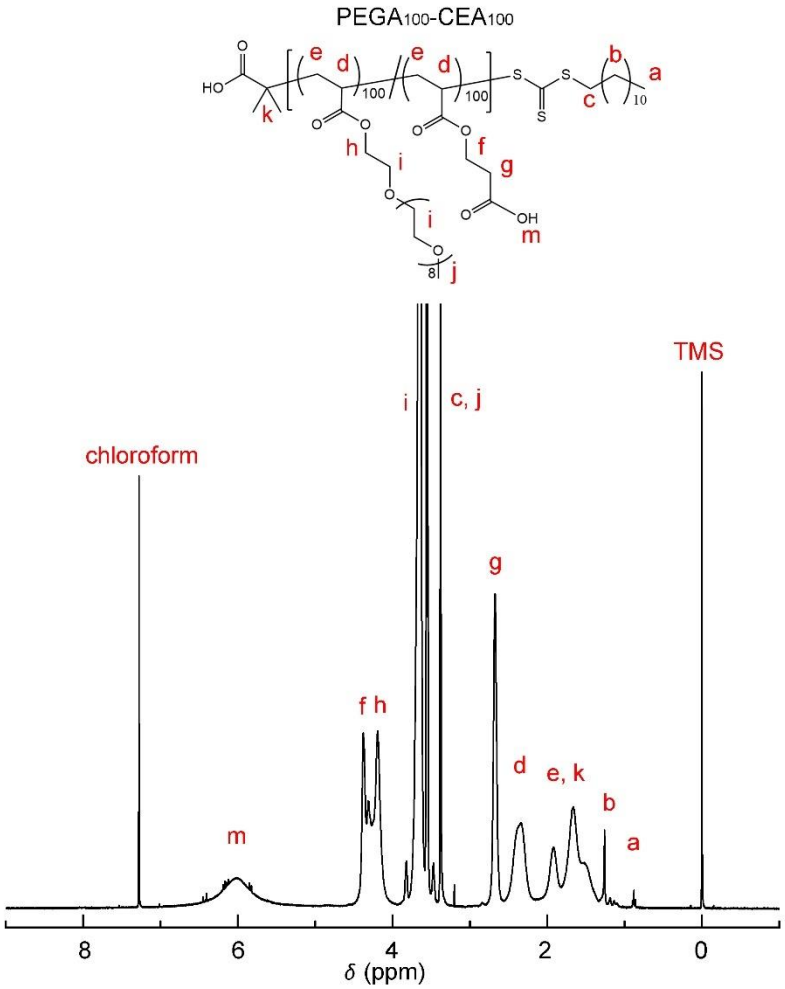


**Figure 2.3**. $^{1}$H NMR spectrum of $PEGA_{100}$-$CEA_{100}$ in chloroform-*d* at 25 °C.

2.2.3.4 Synthesis of $BZA_m$-$PEGA_n$-$CEA_k$ (**TP1**-**TP3**)

The terpolymers, $BZA_{100}$-$PEGA_{90}$-$CEA_{10}$ (**TP1**), $BZA_{100}$-$PEGA_{80}$-$CEA_{20}$ (**TP2**) and $BZA_{100}$-$PEGA_{70}$-$CEA_{30}$ (**TP3**), were prepared to introduce Gd complexes and form the SMDC in aqueous solution. The typical procedure for the synthesis of **TP1** is shown in **Scheme 2.4**. A mixture of AIBN (0.5 mg, 0.003 mmol) and DDMAT (2.2 mg, 0.006 mmol) in dry DMF (1 mL) was added into the polymerization test tube equipped with a magnetic stirring bar in the glovebox. BZA (146.0 mg, 0.90 mmol), PEGA (388.8 mg, 0.81 mmol) and CEA (13.0 mg, 0.09 mmol) were added into the test tube, and polymerization was then started in a 70 °C oil bath and continued for 20 min. The

polymerization reaction was terminated by liquid nitrogen. The product was purified by dialysis (Spectra/Por dialysis membrane, MWCO of 6-8 kD) against methanol and Milli-Q water. After lyophilization, the obtained $BZA_{100}$-$PEGA_{90}$-$CEA_{10}$ and conversion were analyzed by $^1$H NMR (**Figure 2.4**), GPC and SEC-MALS. $^1$H NMR (DMSO-$d_6$ with 0.03% TMS, 400 MHz): $\delta$ (ppm) = 0.88 (*t*, 3H, -S-$CH_2$-$(CH_2)_{10}$-C$\underline{H}_3$), 1.10-1.29 (*m*, 20H, -S-$CH_2$-(C$\underline{H}_2$)$_{10}$-$CH_3$), 1.33-1.99 (*m*, 406H, -(C$\underline{H}_2$-CH(BZA segment))$_m$-, -(C$\underline{H}_2$-CH(PEGA segment))$_n$-, -(C$\underline{H}_2$-CH(CEA segment))$_k$-, (C$\underline{H}_3$)$_2$-C(COOH)-), 2.19-2.53 (*m*, 200H, -($CH_2$-C$\underline{H}$(BZA segment))$_m$-, -($CH_2$-C$\underline{H}$(PEGA segment))$_n$-, -($CH_2$-C$\underline{H}$(CEA segment))$_k$-), 2.60-2.75 (*m*, 20H, -COO-$CH_2$-C$\underline{H}_2$-COOH), 3.31-3.40 (*m*, 272H, -$CH_2$-$CH_2$-O-($CH_2$-$CH_2$-O)$_8$-C$\underline{H}_3$, -S-C$\underline{H}_2$-$(CH_2)_{10}$-$CH_3$), 3.42-3.74 (*m*, 3060H, -$CH_2$-C$\underline{H}_2$-O-(C$\underline{H}_2$-C$\underline{H}_2$-O)$_8$-$CH_3$), 3.90-4.40 (*m*, 200H, -C$\underline{H}_2$-$CH_2$-O-($CH_2$-$CH_2$-O)$_8$-$CH_3$, -COO-C$\underline{H}_2$-$CH_2$-COOH), 4.81-5.16 (*m*, 200H, -COO-C$\underline{H}_2$-$C_6H_5$), 7.17-7.40 (*m*, 500H, -COO-$CH_2$-$C_6\underline{H}_5$). Conv.,$_{BZA}$ = 73.3 %, Conv.,$_{PEGA}$ = 65.7 %, Conv.,$_{CEA}$ = 57.1 %, $M_{n,NMR}$ = 62,700 g/mol, $M_w/M_n$ = 1.62.

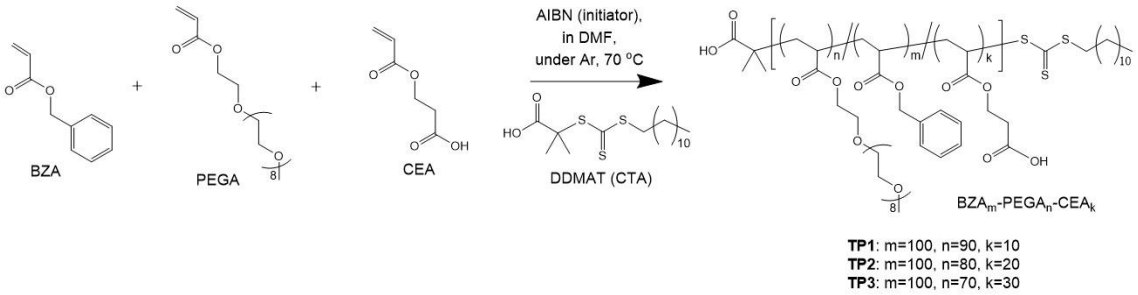


**Scheme 2.4**. Synthesis of $BZA_m$-$PEGA_n$-$CEA_k$ (**TP1**-**TP3**) using RAFT polymerization.

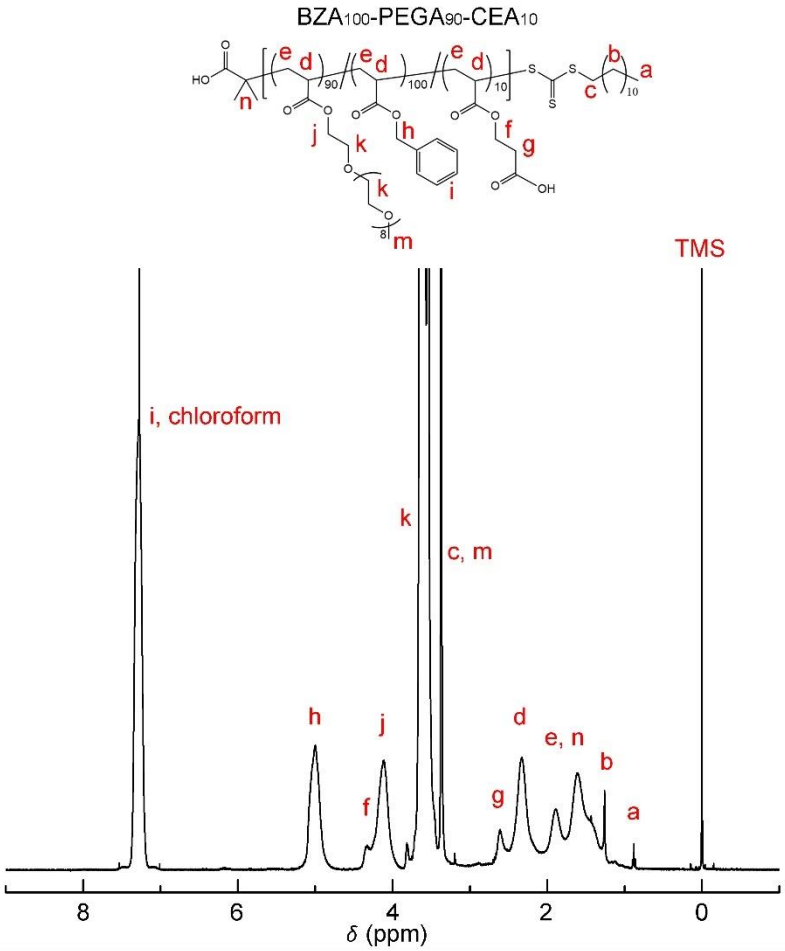


**Figure 2.4**. $^{1}$H NMR spectrum of **TP1** in chloroform-*d* at 25 °C.

## 2.3 RAFT polymerization of random copolymer $BZA_m$-$PEGA_n$

### 2.3.1 Reactivity ratios

Base copolymers were synthesized through RAFT polymerization using PEGA and BZA. To achieve uniform SMDC formation, the randomness of the polymer sequence in the base polymer and living nature of polymerization are important. Thus, the polymerization behaviors and reactivity ratios of BZA/PEGA system were confirmed. First, four copolymers, $BZA_m$-$PEGA_n$, were synthesized according to the polymerization procedure described above "(1) Synthesis of $BZA_m$-$PEGA_n$ (**P1**-**P20**)" excluding the monomer feed ratio (BZA/PEGA = 2/8, 4/6, 6/4 and 8/2) and the polymerization time (t

= 20 min). The mole fractions of monomers ($M_a$ and $M_b$) in feed and copolymer were obtained by $^1$H NMR, where the BZA and PEGA monomers were defined as $M_a$ and $M_b$, respectively. Generally, the reactivity ratio $r_a$ is a measure of the tendency toward self-propagation of $M_a$-chain ends to add additional $M_a$. Likewise, the reactivity ratio for the $M_b$-chain end is given by $r_b$. The Fineman-Ross method was used for data analysis to generate and fit reactivity ratios [8]. The relationship between the molecular fraction of the monomer and the reactivity ratio is shown as following equation.

$$F_a = \frac{r_a {f_a}^2 + f_a f_b}{r_a {f_a}^2 + 2 f_a f_b + r_b {f_b}^2} \qquad \textbf{(Equation 2.1)}$$

Where $f_a$ and $f_b$ are Mole fractions of $M_a$ and $M_b$ in feed after the short time reaction, $F_a$ and $F_b$ are Mole fractions of $M_a$ and $M_b$ in copolymers after the short time reaction, $r_a$ and $r_b$ are the reactivity ratios of $M_a$ and $M_b$. These $r_a$ and $r_b$ values could be calculated by the following equation.

$$\frac{f_a^2(1-F_a)}{(1-f_a)^2 F_a} r_a - r_b = \frac{f_a(2F_a-1)}{(1-f_a)F_a} \qquad \textbf{(Equation 2.2)}$$

The Mole fractions $f_a$, $f_b$, $F_a$, and $F_b$ were obtained from NMR results. Four relation equations were drawn in a coordinate axis ($r_b$ versus $r_a$), the final $r_a$ and $r_b$ values are the center point of the area enclosed by the four straight lines, subsequently, the copolymerization curve was obtained according to **Equation 2.1**. The obtained reactivity ratios of BZA/PEGA copolymerization are shown in **Figure 2.5**; $r_a$ was equal to 1.28 and $r_b$ was equal to 0.73. As both $r_a$ and $r_b$ were close to 1.0, it is reasonable to conclude that the obtained copolymer had a totally random sequence, while slightly affected by steric hindrance.

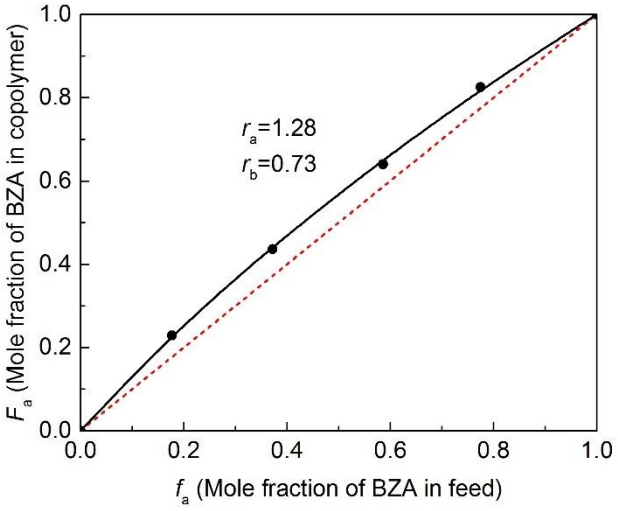


**Figure 2.5**. Plot of the mole fraction of BZA in copolymers versus that in the feed to determine the reactivity ratios of BZA/PEGA copolymers (**P1**-**P20**).

### 2.3.2 Polymerization kinetics and quality control

To investigate the effect of polymer parameters on the formation of SMDC, twenty copolymers, $BZA_m$-$PEGA_n$ (**P1**-**P20**), with different degrees of polymerization (DPs) and BZA/PEGA ratios were synthesized by RAFT polymerization. Target DP, monomer feed ratios and product names are shown in **Table 2.1**.

**Table 2.1**. List of $BZA_m$-$PEGA_n$ (**P1**-**P20**) random copolymers with different DPs.

| No. | Total DP[a)] | BZA/PEGA[b)] | Polymer |
|---|---|---|---|
| **P1** | 100 | 2/8 | $BZA_{20}$-$PEGA_{80}$ |
| **P2** | 100 | 4/6 | $BZA_{40}$-$PEGA_{60}$ |
| **P3** | 100 | 5/5 | $BZA_{50}$-$PEGA_{50}$ |
| **P4** | 100 | 6/4 | $BZA_{60}$-$PEGA_{40}$ |
| **P5** | 200 | 2/8 | $BZA_{40}$-$PEGA_{160}$ |
| **P6** | 200 | 4/6 | $BZA_{80}$-$PEGA_{120}$ |
| **P7** | 200 | 5/5 | $BZA_{100}$-$PEGA_{100}$ |

| | | | |
|---|---|---|---|
| **P8** | 200 | 6/4 | $BZA_{120}$-$PEGA_{80}$ |
| **P9** | 300 | 2/8 | $BZA_{60}$-$PEGA_{240}$ |
| **P10** | 300 | 4/6 | $BZA_{120}$-$PEGA_{180}$ |
| **P11** | 300 | 5/5 | $BZA_{150}$-$PEGA_{150}$ |
| **P12** | 300 | 6/4 | $BZA_{180}$-$PEGA_{120}$ |
| **P13** | 400 | 2/8 | $BZA_{80}$-$PEGA_{320}$ |
| **P14** | 400 | 4/6 | $BZA_{160}$-$PEGA_{240}$ |
| **P15** | 400 | 5/5 | $BZA_{200}$-$PEGA_{200}$ |
| **P16** | 400 | 6/4 | $BZA_{240}$-$PEGA_{160}$ |
| **P17** | 500 | 2/8 | $BZA_{100}$-$PEGA_{400}$ |
| **P18** | 500 | 4/6 | $BZA_{200}$-$PEGA_{300}$ |
| **P19** | 500 | 5/5 | $BZA_{250}$-$PEGA_{250}$ |
| **P20** | 500 | 6/4 | $BZA_{300}$-$PEGA_{200}$ |

*a)* Total degree of polymerization (DP); *b)* Feed ratio of the BZA monomer to the PEGA monomer in the design.

The kinetic analysis of BZA/PEGA copolymerization (**Figures 2.6, 2.7, and 2.8**, where **P3**, **P7**, **P11**, **P15** and **P19** were selected as examples) revealed that these polymerizations were preceded by following living nature, however, the polydispersity value increased over 70% conversion because of the increase in viscosity. Therefore, to control the quality of produced random copolymers, the conversion rates were controlled below 70% in this research. As an example, for the polymerization of $BZA_{100}$-$PEGA_{100}$ (**P7**), using the raw materials of $[BZA]_0 : [PEGA]_0 : [DDMAT(CTA)]_0 = 150:150:1$, the RAFT polymerization was carried out for 30 min when the conversion rate was about 67%.

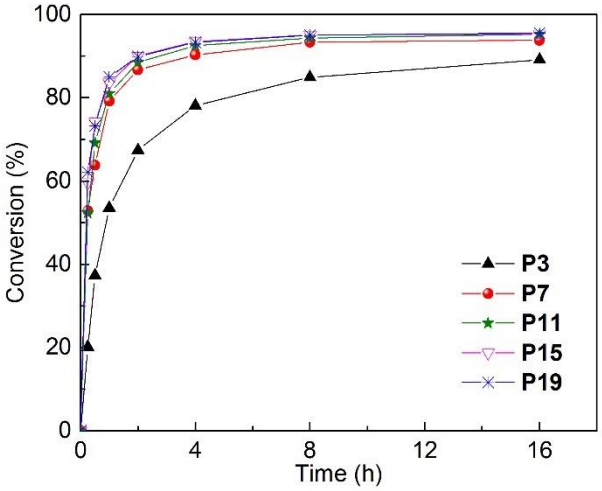


**Figure 2.6**. Plots of conversion versus time in the polymerization of $BZA_m$-$PEGA_n$ copolymers (**P3**, **P7**, **P11**, **P15**, and **P19**).

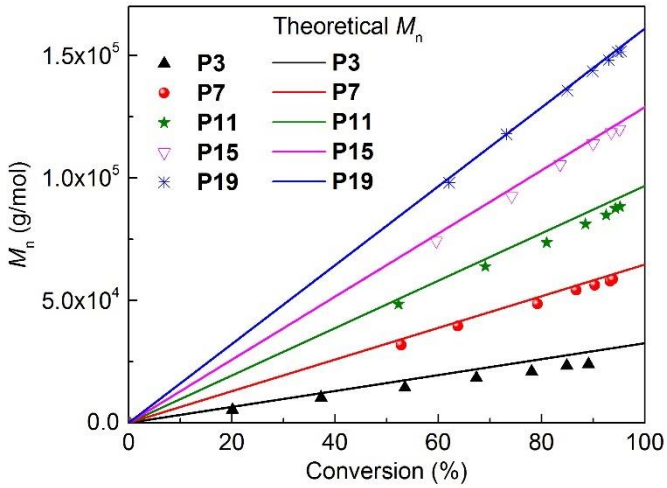


**Figure 2.7**. Evolution of molecular weight with conversion for $BZA_m$-$PEGA_n$ polymerizations (**P3**, **P7**, **P11**, **P15**, and **P19**). Solid lines indicate the theoretical number average molecular weight ($M_n$), assuming the formation on one living polymer per one radical initiator.

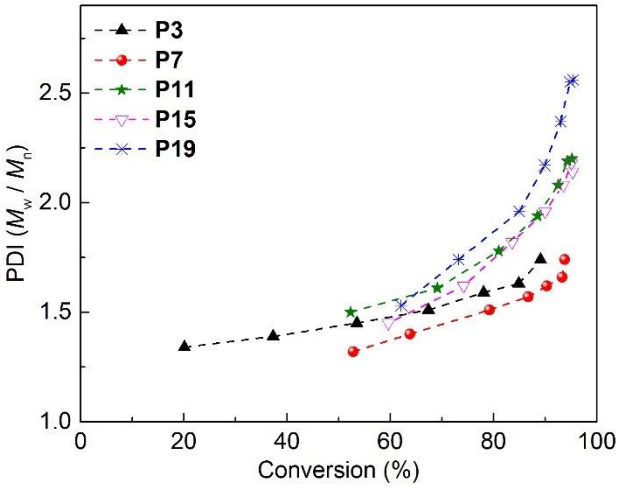


**Figure 2.8**. Evolution of polydispersity with conversion for $BZA_m$-$PEGA_n$ polymerizations (**P3**, **P7**, **P11**, **P15**, and **P19**).

## 2.4 RAFT polymerization of random terpolymer $BZA_m$-$PEGA_n$-$CEA_k$

### 2.4.1 Reactivity ratios

Based on the results above, terpolymers $BZA_m$-$PEGA_n$-$CEA_k$ were synthesized through RAFT polymerization technique using PEGA, BZA, and CEA. The reactivity and randomization of each monomer in radical copolymerization were separately confirmed by a polymerization reaction with $BZA_m$-$CEA_k$ and $PEGA_n$-$CEA_k$. The same analysis was adopted to the BZA/CEA and PEGA/CEA copolymerization, and all indicated good randomness of sequence (**Figures 2.9 and 2.10**). Because the randomness of the polymer sequence was evidenced by analysis of BZA/PEGA, BZA/CEA, and PEGA/CEA copolymerization, all polymers, $BZA_m$-$PEGA_n$-$CEA_k$, might be inferred as terpolymers equipped with a random order of monomer units.

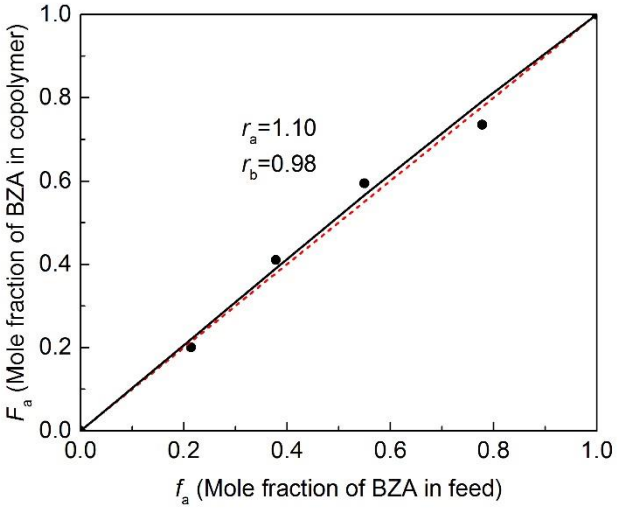


**Figure 2.9**. Plot of the mole fraction of BZA in copolymers versus that in the feed to determine the reactivity ratios of BZA/CEA copolymers.

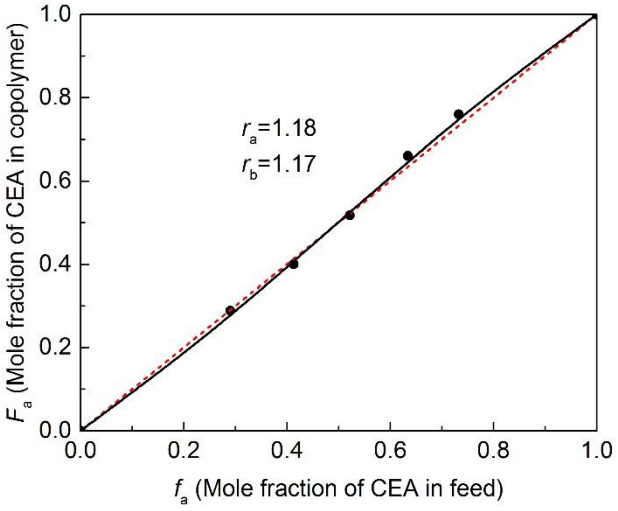


**Figure 2.10**. Plot of the mole fraction of CEA in copolymers versus that in the feed to determine the reactivity ratios of PEGA/CEA copolymers.

### 2.4.2 Polymerization kinetics and quality control

random-terpolymers, including $BZA_{100}$-$PEGA_{90}$-$CEA_{10}$ (**TP1**), $BZA_{100}$-$PEGA_{80}$-$CEA_{20}$ (**TP2**), and $BZA_{100}$-$PEGA_{70}$-$CEA_{30}$ (**TP3**), were prepared by RAFT

polymerization, and these preparations were also evaluated by kinetic plots using total conversion versus $M_n$/polymerization time. As shown in **Figures 2.11** and **2.12**, these reactions also showed controlled/living polymerization behaviors with relatively narrow polydispersity when their conversion values were <70%. As an example, for the polymerization of $BZA_{100}$-$PEGA_{90}$-$CEA_{10}$ (**TP1**), using the raw materials of $[BZA]_0$ : $[PEGA]_0$ : $[CEA]_0$ : $[DDMAT(CTA)]_0$ = 150:135:15:1, the RAFT polymerization was carried out for 20 min when the conversion rate was about 69%. Overall, all polymerization reactions were precisely analyzed and an appropriate condition for preparing terpolymers was determined.

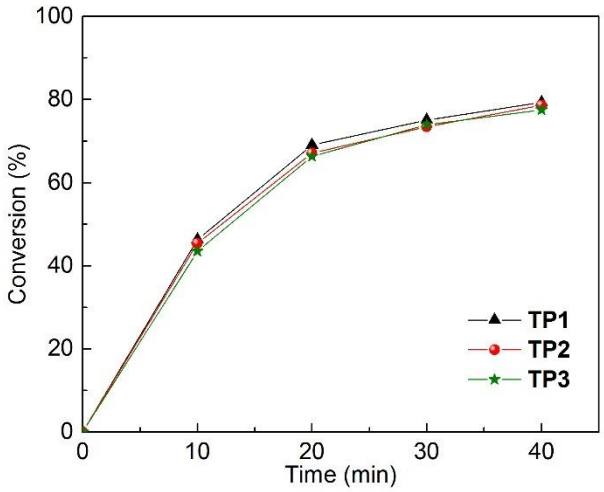


**Figure 2.11**. Plots of conversion versus time in the polymerization of **TP1**-**TP3**.

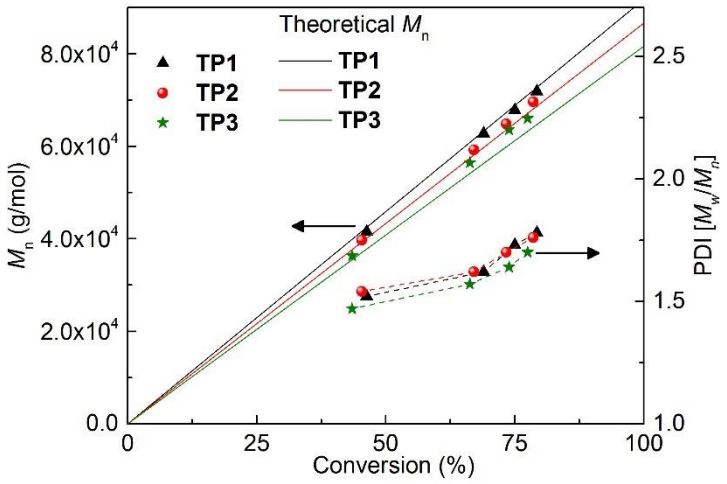


**Figure 2.12**. Evolution of molecular weight and polydispersity with conversion for **TP1**-**TP3** polymerizations. Solid lines indicate the theoretical number average molecular weight ($M_n$), assuming the formation on one living polymer per one radical initiator.

## 2.5 Summary

The random copolymer $BZA_m$-$PEGA_n$ was designed and polymerized as the base copolymer to achieve SMDC formation. The randomness of the polymer sequence was confirmed by reactivity ratios monomers, and living nature of polymerization are determined by the investigation of reaction kinetics. To load the imaging/therapeutic agent in the macromolecule, a random terpolymer $BZA_m$-$PEGA_n$-$CEA_k$ was designed based on the RAFT polymerization process of $BZA_m$-$PEGA_n$. The randomness of the polymer sequence was evidenced, and the polymerization kinetics was analyzed to determine an appropriate condition for preparing terpolymers; thus, these polymers were used as platforms for further synthesis, analysis, and characterization in this study.

## 2.6 References

[1] Corrigan N, Jung K, Moad G, Hawker CJ, Matyjaszewski K, Boyer C. Reversible-

deactivation radical polymerization (Controlled/living radical polymerization): From discovery to materials design and applications. Progress in Polymer Science, **2020**, 111: 101311.

[2] Truong NP, Jones GR, Bradford KGE, Konkolewicz D, Anastasaki A. A comparison of RAFT and ATRP methods for controlled radical polymerization. Nature Reviews Chemistry, **2021**, 5(12): 859-869.

[3] Audran G, Bagryanskaya EG, Marque SRA, Postnikov P. New variants of nitroxide mediated polymerization. Polymers, **2020**, 12(7): 1481.

[4] Nothling MD, Fu Q, Reyhani A, Allison-Logan S, Jung K, Zhu J, Kamigaito M, Boyer C, Qiao GG. Progress and perspectives beyond traditional RAFT polymerization. Advanced Science, **2020**, 7(20): 2001656.

[5] Moad G, Rizzardo E. A 20th anniversary perspective on the life of RAFT (RAFT coming of age). Polymer International, **2020**, 69(8): 658-661.

[6] Moad G, Rizzardo E, Thang SH. Living radical polymerization by the RAFT process. Australian journal of chemistry, **2005**, 58(6): 379-410.

[7] Relógio P, Charreyre MT, Farinha JPS, Martinho JMG, Pichot C. Well-defined polymer precursors synthesized by RAFT polymerization of N, N-dimethylacrylamide/ N-acryloxysuccinimide: random and block copolymers. Polymer, **2004**, 45(26): 8639-8649.

[8] Lynd NA, Ferrier Jr RC, Beckingham BS. Recommendation for accurate experimental determination of reactivity ratios in chain copolymerization. Macromolecules, **2019**, 52(6): 2277-2285.

# Chapter 3. Formation and characterization of SMDC and SMDC-Gd

## 3.1 Introduction

The SMDC structure was proposed with reference to recently presented single chain polymeric nanoparticles (SCPNs). SCPNs represent nanoparticles formed by a single polymer chain through the self-folding of the chain or intramolecular cross-linking of function segments [1-3]. This structural design has demonstrated the feasibility of producing nanoparticles with significantly smaller sizes compared to current polymeric micelles, positioning it as a potential drug carrier [4-5]. However, despite its promise, SCPNs face challenges in realizing drug loading, releasing, and application in cancer imaging and therapy due to their structural characteristics. Meanwhile, as highlighted, the smaller particle size, beyond the critical value for renal excretion, offers enhanced penetration into tumor tissue. To fully exploit the size advantages of SCPNs, the precise control of formation morphology and size by identifying appropriate polymer parameters should be the focal point, a consideration that has yet to be thoroughly examined.

In this research, the investigation was carried out about the relationships between SMDC formation conditions and polymer parameters, specifically the DP and the quantity ratio between different monomers. This clarification aimed to identify the optimal macromolecular structure conducive to the formation of SMDC with a size close to 5-7 nm. Subsequently, Gd-DOTA was incorporated into the macromolecule as the imaging and therapeutic agent for cancer. The realized drug-loaded SMDC, with a size within the range of 5-7 nm, referred to as Gd-DOTA loaded SMDC (SMDC-Gd) in this research, underwent characterization by evaluating forming conditions, including degree

of aggregation (DA) and size.

## 3.2 Materials and methods

### 3.2.1 Materials

*N*,*N*-dimethylformamide (DMF), chloroform, methanol, 4-(4,6-dimethoxy-1,3,5-triazin-2-yl)-4-methyl-morpholinium chloride (DMT-MM), gadolinium trichloride hexahydrate ($GdCl_3 \cdot 6H_2O$) and phosphate-buffered saline (PBS (-)) were purchased from Fujifilm Wako Pure Chemical Corporation (Osaka, Japan). s-2-(4-Aminobenzyl)-1,4,7,10-tetraazacyclododecane tetra-*tert*-butylacetate (p-$NH_2$-Bn-DOTA-*t*Bu) was obtained from Macrocyclics, Inc. (Plano, TX, USA). Trifluoroacetic acid (TFA) was purchased from Tokyo Chemical Industry Co., Ltd. (Tokyo, Japan). PBS (-) tablet was fully dissolved into Milli-Q water (1 tablet into 100 mL water), other reagents and solvents were used as received.

### 3.2.2 Analysis

The $^1H$ nuclear magnetic resonance (NMR) spectra were recorded using a Bruker biospin AVANCE III 400A (400 MHz) (Bruker Corporation, Billerica, MA, USA) instrument with $CDCl_3$, $D_2O$, and DMSO-$d_6$ containing tetramethylsilane (TMS) as the internal standard. Size-exclusion chromatography coupled to multi-angle light scattering (SEC-MALS) was used by two solvent systems. SEC-MALS with PBS system was performed at 40 °C using a JASCO Extrema HPLC system (LC-Net II/ADC, Co-4060, AS-4050, PU-4180, UV-4070, and RI-4030; JASCO Corporation) and DAWN 8 MALS detector (Wyatt Technology Corporation, Santa Barbara, CA, USA) equipped with an OHpak SB-804HQ column (linear, 8 mm × 300 mm; pore size, 20 nm; bead size, 10 μm; exclusion limit, $1 \times 10^6$ g/mol; Showa Denko K. K., Tokyo, Japan), OHpak SB-806MHQ column (linear, 8 mm × 300 mm; pore size, 1.5 μm; bead size, 13 μm; exclusion limit, $2 \times 10^7$ g/mol; Showa Denko K. K.), and OHpak SB-G 6B guard column (Showa Denko K. K.) at a flow rate of 1.0 mL/min. SEC-MALS with chloroform was performed at 40 °C using a TOSOH HLC-8220 GPC system (Tosoh Corporation) and DAWN HELEOS II

MALS detector (Wyatt Technology Corporation) equipped with an LF-804 column (linear, 8 mm × 300 mm; pore size, 300 nm; bead size, 6 μm; exclusion limit, $2 \times 10^6$ g/mol; Showa Denko K. K.), and an LF-G guard column (Showa Denko K. K.) at a flow rate of 1.0 mL/min. Data from these two SEC-MALS systems were analyzed using ASTRA ver. 8.0.0.25 (Wyatt Technology Corporation, Santa Barbara, CA, USA). The Gd concentration in each sample was measured by inductively coupled plasma mass spectrometry (ICP-MS) using an Agilent 7700x ICP-MS (Agilent Technologies Inc., Santa Clara, CA, USA). Dynamic light scattering and ζ potential measurement was performed using Malvern Zetasizer Nano ZSP (Malvern Panalytical, Malvern, Worcestershire, UK) equipped with a 10 mW He–Ne laser operating at 633 nm with 173° collecting optics. Data were analyzed using Zetasizer Software ver. 7.03 (Malvern Panalytical). The radius of gyration ($R_g$) values was obtained by small angle X-ray scattering (SAXS) measurement. A nano-viewer SAXS system (Rigaku Corporation, Tokyo, Japan) was used with the scattering angle ranging from 0° to 4° at 25 °C. The results were analyzed by Smartlab Studio II ver. 4.3.239.0 (Rigaku Corporation). $R_g$ values were calculated by the Guinier plot, and a self-folding macromolecular drug carrier (SMDC) formation performance was observed using a Kratky plot. Transmission electron microscope (TEM) measurement was performed using the JEM-2100F TEM system (JEOL, Ltd., Akishima, Tokyo). For TEM measurement, each sample was stained on formvar/carbon supported-copper grids (Sigma-Aldrich Corporation) and dried overnight. Data were analyzed using ImageJ ver.1.53k (National Institutes of Health, Bethesda, MD, USA).

### 3.2.3 Typical polymerization procedure

3.2.3.1 Synthesis of $BZA_m$-$PEGA_n$-$CEA_k(Gd\text{-}DOTA)_j$ (**TP4**-**TP6**)

Gd loaded terpolymers, $BZA_{100}$-$PEGA_{90}$-$CEA_{10}(Gd\text{-}DOTA)_4$ (**TP4**), $BZA_{100}$-$PEGA_{80}$-$CEA_{20}(Gd\text{-}DOTA)_9$ (**TP5**) and $BZA_{100}$-$PEGA_{70}$-$CEA_{30}(Gd\text{-}DOTA)_{17}$ (**TP6**) were synthesized to prepare SMDC-Gds in aqueous solutions according to the following

typical polymerization procedure of **TP4**: in detail, **TP4** for SMDC-$Gd_4$, **TP5** for SMDC-$Gd_9$, and **TP6** for SMDC-$Gd_{17}$.

The typical synthetic route of **TP4** for preparing SMDC-$Gd_4$ is shown in **Scheme 3.1**. In the first step, *p*-$NH_2$-Bn-DOTA-*t*Bu was conjugated to the CEA segment in random terpolymer **TP1** by a condensation reaction. A mixture of **TP1** (2449 mg, 0.04 mmol) and DMT-MM (132.8 mg, 0.48 mmol) in methanol/DMF mixture (20 mL, methanol:DMF = 1:1) was added into a mighty vial equipped with a magnetic stirring bar and stirred for 1 h at 0 °C. Subsequently, *p*-$NH_2$-Bn-DOTA-*t*Bu (339.2 mg, 0.4 mmol) was added in the solution, and the reaction continued overnight at room temperature. The product was purified by dialysis (Spectra/Por dialysis membrane, MWCO of 6-8 kD) against methanol and Milli-Q water. Then, $BZA_{100}$-$PEGA_{90}$-$CEA_{10}$(DOTA-*t*Bu)$_4$ was obtained by lyophilization.

In the second synthesis step of **TP4**, DOTA-*t*Bu segments were deprotected by adding all the purified $BZA_{100}$-$PEGA_{90}$-$CEA_{10}$(DOTA-*t*Bu)$_4$ in the TFA/chloroform mixture (20 mL, TFA:chloroform = 1:1), vigorously stirred in a mighty vial overnight at room temperature. The product was purified by dialysis (Spectra/Por dialysis membrane, MWCO of 6-8 kD) against methanol and Milli-Q water. And then the $BZA_{100}$-$PEGA_{90}$-$CEA_{10}$(DOTA)$_4$ was obtained by lyophilization and analyzed by $^1$H NMR (**Figure 3.1**). $^1$H NMR (DMSO-$d_6$ with TMS, 400 MHz): $\delta$ (ppm) = 0.88 (*t*, 3H, -S-$CH_2$-$(CH_2)_{10}$-C$\underline{H}_3$), 0.93-1.27 (*m*, 20H, -S-$CH_2$-(C$\underline{H}_2$)$_{10}$-$CH_3$), 1.30-1.98 (*m*, 406H, -(C$\underline{H}_2$-CH(BZA segment))$_m$-, -(C$\underline{H}_2$-CH(PEGA segment))$_n$-, -(C$\underline{H}_2$-CH(CEA segment))$_k$-, (C$\underline{H}_3$)$_2$-C(COOH)-), 2.05-2.43 (*m*, 200H, -($CH_2$-C$\underline{H}$(BZA segment))$_m$-, -($CH_2$-C$\underline{H}$(PEGA segment))$_n$-, -($CH_2$-C$\underline{H}$(CEA segment))$_k$-), 2.54-2.68 (*m*, 20H, -COO-$CH_2$-C$\underline{H}_2$-COOH, -COO-$CH_2$-C$\underline{H}_2$-CO-DOTA segment), 3.18-3.27 (*m*, 422H, -$CH_2$-$CH_2$-O-($CH_2$-$CH_2$-O)$_8$-C$\underline{H}_3$, -C$\underline{H}_2$-C$\underline{H}_2$-N($CH_2$COOH)-, -S-C$\underline{H}_2$-$(CH_2)_{10}$-$CH_3$), 3.28-3.71 (*m*, 3100H, -$CH_2$-C$\underline{H}_2$-O-(C$\underline{H}_2$-C$\underline{H}_2$-O)$_8$-$CH_3$, -$CH_2$-$CH_2$-N(C$\underline{H}_2$COOH)-, -NH-$C_6H_4$-C$\underline{H}_2$-), 3.85-4.35 (*m*, 200H, -C$\underline{H}_2$-$CH_2$-O-($CH_2$-$CH_2$-O)$_8$-$CH_3$, -COO-C$\underline{H}_2$-$CH_2$-COOH, -COO-C$\underline{H}_2$-$CH_2$-CO-

DOTA segment), 4.77-5.15 (*m*, 200H, -COO-C$\underline{H}_2$-$C_6H_5$), 7.00-7.60 (*m*, 540H, -COO-$CH_2$-$C_6\underline{H}_5$, -NH-$C_6\underline{H}_4$-$CH_2$-).

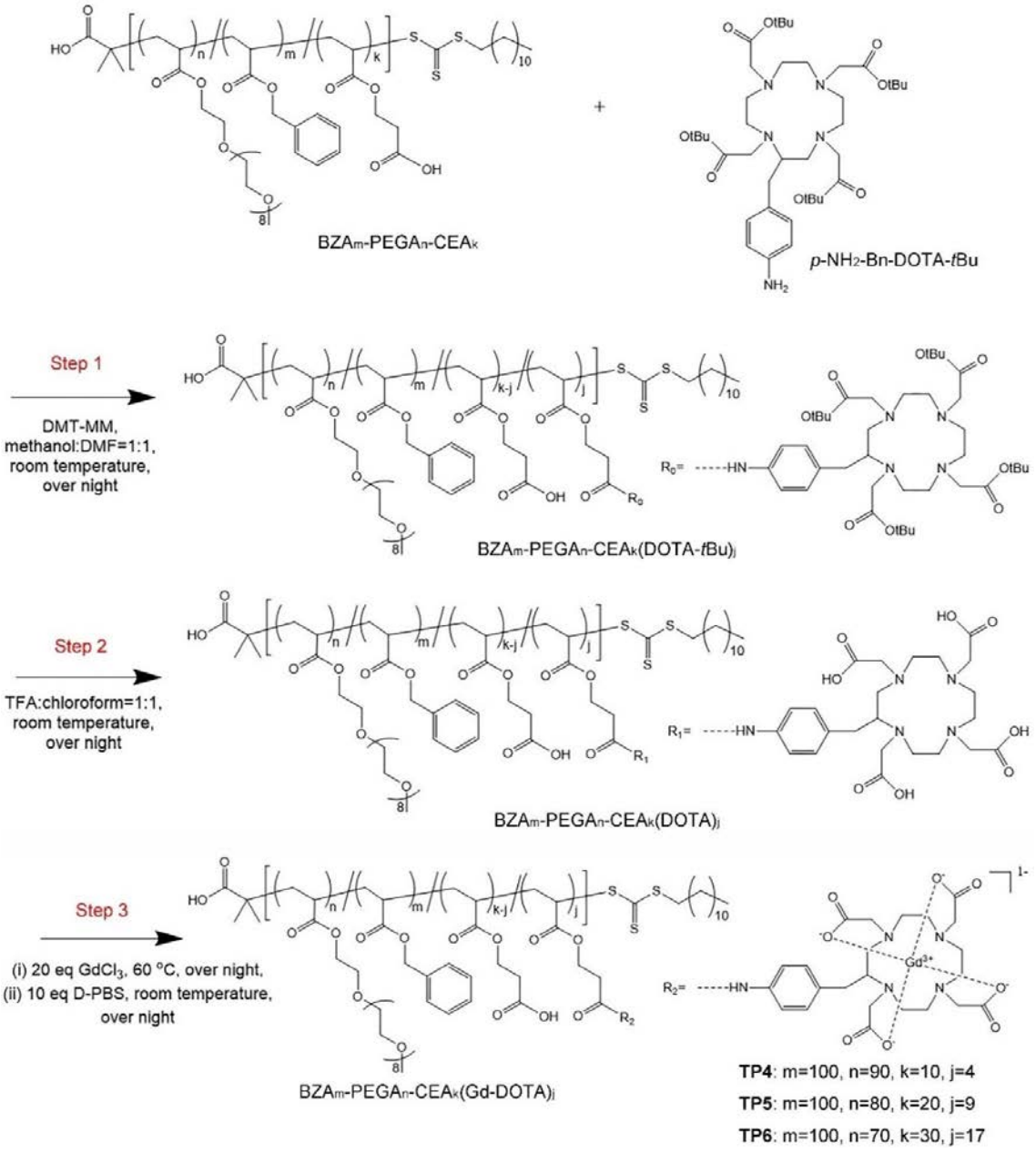


**Scheme 3.1**. Reaction pathways for the synthesis of **TP4**-**TP6**.

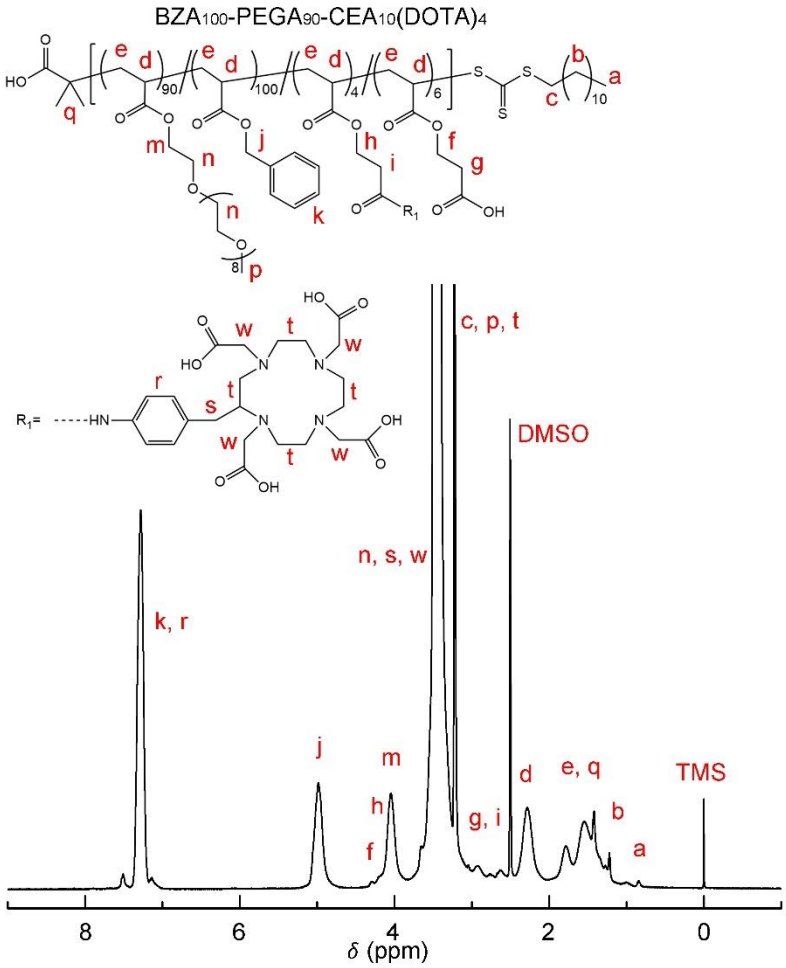


**Figure 3.1**. $^{1}$H NMR spectrum of $BZA_{100}$-$PEGA_{90}$-$CEA_{10}(DOTA)_4$ in DMSO-$d_6$ at 25 °C.

In the final synthesis step of **TP4**, Gd was chelated to the DOTA ligand. A mixture of all the deprotected $BZA_{100}$-$PEGA_{90}$-$CEA_{10}(DOTA)_4$ and $GdCl_3 \cdot 6H_2O$ (2973.6 mg, 8.0 mmol) in Milli-Q water was added into a mighty vial equipped with a magnetic stirring bar. The chelation reaction was started in a 60 °C water bath and continued overnight. To remove Gd that was not chelated to DOTA but reacted with the residual carboxyl group in CEA segments, the product was subjected to dialysis (Spectra/Por dialysis membrane, MWCO of 6-8 kD) against Milli-Q water, mixed with PBS (-) (100 mL) and vigorously stirred overnight at room temperature. The product was purified by filtration (syringe-driven filter unit) and dialysis (Spectra/Por dialysis membrane, MWCO of 6-8 kD)

against Milli-Q water. Then the **TP4** was obtained by lyophilization. The amount of Gd loaded into each polymer was confirmed by ICP-MS.

3.2.3.2 Synthesis of $PEGA_n$-$CEA_k(Gd\text{-}DOTA)_j$ (**PEGA-Gd$_4$** and **PEGA-Gd$_{12}$**)

Utilized as polymer control groups, $PEGA_{124}$-$CEA_{10}(Gd\text{-}DOTA)_4$, named PEGA-$Gd_4$, and $PEGA_{104}$-$CEA_{30}(Gd\text{-}DOTA)_{12}$, named PEGA-$Gd_{12}$, were polymerized by the following typical polymerization procedure of PEGA-$Gd_4$. These two copolymers only contained hydrophilic segments, where were expected to be dissolved in water as polymer chains without construct particles.

The typical synthetic route of PEGA-$Gd_4$ is shown in **Scheme 3.2**. In the first step, a mixture of $PEGA_{124}$-$CEA_{10}$ (2452 mg, 0.04 mmol) and DMT-MM (132.8 mg, 0.48 mmol) in a methanol/DMF mixture (20 mL, methanol:DMF = 1:1) was added into a mighty vial equipped with a magnetic stirring bar and stirred for 1 h at 0 °C. Subsequently, *p*-$NH_2$-Bn-DOTA-*t*Bu (339.2 mg, 0.4 mmol) was added in the solution, and the reaction continued overnight at room temperature. The product was purified by dialysis (Spectra/Por dialysis membrane, MWCO of 6-8 kD) against methanol and Milli-Q water. Then, $PEGA_{124}$-$CEA_{10}(DOTA\text{-}t\text{Bu})_4$ was obtained by lyophilization.

In the second synthesis step of PEGA-$Gd_4$, DOTA-*t*Bu segments were deprotected by adding all the purified $PEGA_{124}$-$CEA_{10}(DOTA\text{-}t\text{Bu})_4$ in the TFA/chloroform mixture (20 mL, TFA:chloroform = 1:1), vigorously stirred in a mighty vial overnight at room temperature. The product was purified by dialysis (Spectra/Por dialysis membrane, MWCO of 6-8 kD) against methanol and Milli-Q water. Then, the $PEGA_{124}$-$CEA_{10}(DOTA)_4$ was obtained by lyophilization and analyzed by $^1$H NMR (**Figure 3.2**). $^1$H NMR (DMSO-$d_6$ with TMS, 400 MHz): $\delta$ (ppm) = 0.88 (*t*, 3H, -S-$CH_2$-$(CH_2)_{10}$-C$\underline{H}_3$), 0.93-1.27 (*m*, 20H, -S-$CH_2$-(C$\underline{H}_2$)$_{10}$-$CH_3$), 1.30-1.98 (*m*, 274H, -(C$\underline{H}_2$-CH(PEGA segment))$_n$-, -(C$\underline{H}_2$-CH(CEA segment))$_k$-, (C$\underline{H}_3$)$_2$-C(COOH)-), 2.05-2.43 (*m*, 134H, -($CH_2$-C$\underline{H}$(PEGA segment))$_n$-, -($CH_2$-C$\underline{H}$(CEA segment))$_k$-), 2.54-2.68 (*m*, 20H, -COO-$CH_2$-C$\underline{H}_2$-COOH, -COO-$CH_2$-C$\underline{H}_2$-CO-DOTA segment), 3.18-3.27 (*m*, 524H, -$CH_2$-$CH_2$-O-($CH_2$-$CH_2$-O)$_8$-C$\underline{H}_3$, -C$\underline{H}_2$-C$\underline{H}_2$-N($CH_2$COOH)-, -S-C$\underline{H}_2$-$(CH_2)_{10}$-$CH_3$), 3.28-

3.71 (*m*, 4256H, -$CH_2$-C$\underline{H}_2$-O-(C$\underline{H}_2$-C$\underline{H}_2$-O)$_8$-$CH_3$, -$CH_2$-$CH_2$-N(C$\underline{H}_2$COOH)-, -NH-$C_6H_4$-C$\underline{H}_2$-), 3.85-4.35 (*m*, 268H, -C$\underline{H}_2$-$CH_2$-O-($CH_2$-$CH_2$-O)$_8$-$CH_3$, -COO-C$\underline{H}_2$-$CH_2$-COOH, -COO-C$\underline{H}_2$-$CH_2$-CO-DOTA segment), 7.00-7.60 (*m*, 40H, -NH-$C_6\underline{H}_4$-$CH_2$-).

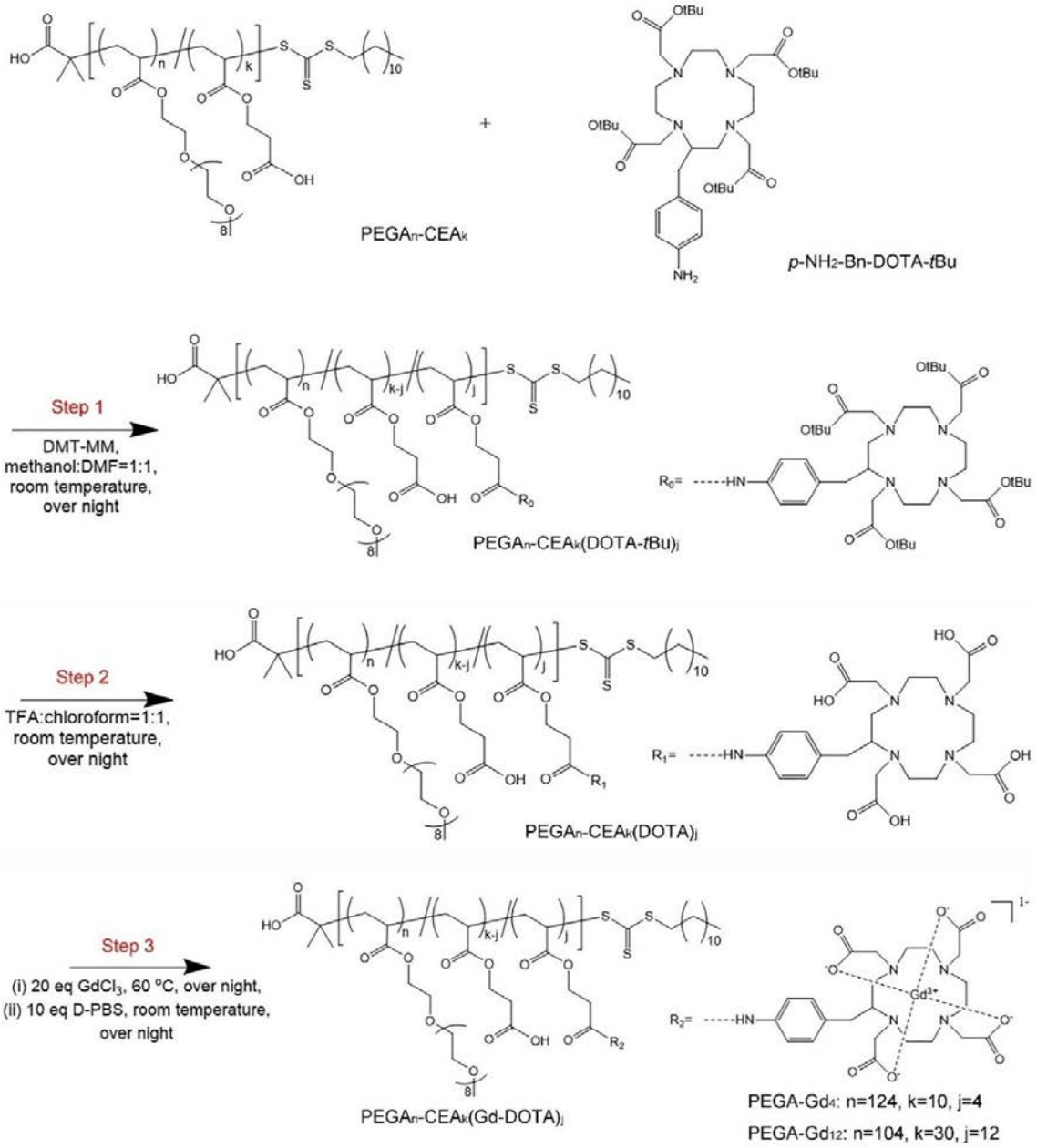


**Scheme 3.2**. Reaction pathways for the synthesis of PEGA-$Gd_4$ and PEGA-$Gd_{12}$.

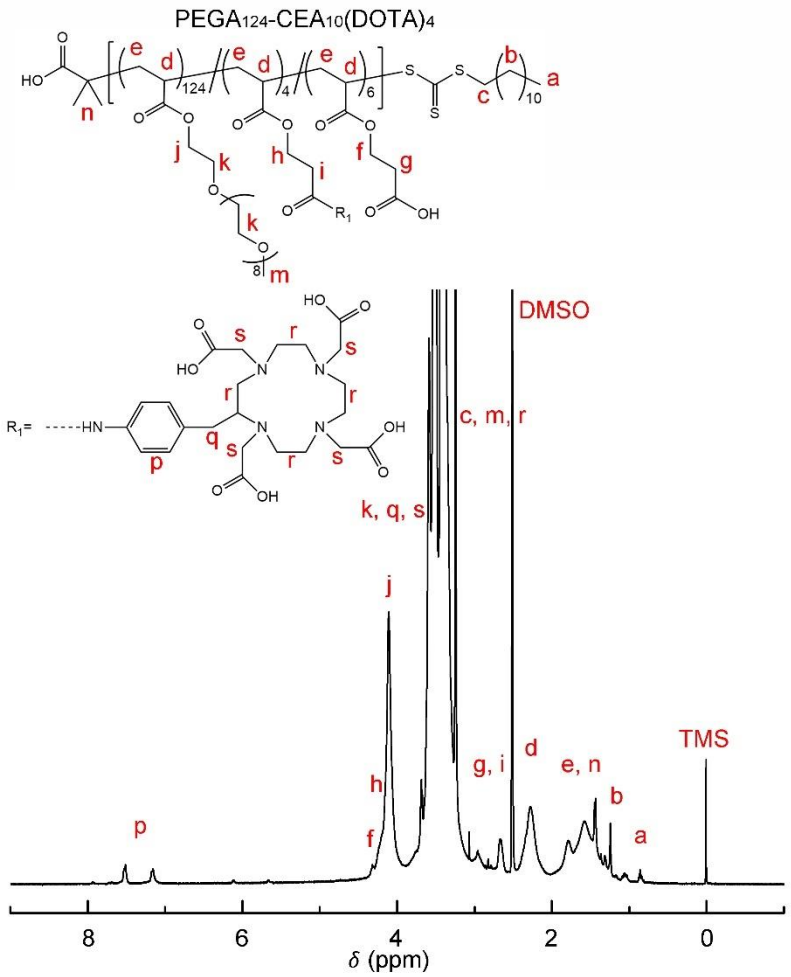


**Figure 3.2**. $^{1}$H NMR spectrum of PEGA$_{124}$-CEA$_{10}$(DOTA)$_4$ in DMSO-$d_6$ at 25 °C.

In the final synthesis step of PEGA-Gd$_4$, Gd was chelated to the DOTA ligand. A mixture of all the deprotected PEGA$_{124}$-CEA$_{10}$(DOTA)$_4$ and $GdCl_3 \cdot 6H_2O$ (2973.6 mg, 8.0 mmol) in Milli-Q water was added into a mighty vial equipped with a magnetic stirring bar. The chelation reaction was started in a 60 °C water bath and continued overnight. To remove Gd that was not chelated to DOTA but reacted with the residual carboxyl group in CEA segments, the product was subjected to dialysis (Spectra/Por dialysis membrane, MWCO of 6-8 kD) against Milli-Q water, mixed with PBS (-) (100 mL) and kept vigorously stirring overnight at room temperature. The product was purified by filtration (syringe-driven filter unit) and dialysis (Spectra/Por dialysis membrane,

MWCO of 6-8 kD) against Milli-Q water. And then the PEGA-$Gd_4$ was obtained by lyophilization. The amount of loaded-Gd in each polymer was confirmed by ICP-MS.

### 3.2.4 Preparation of SMDC and SMDC-Gd samples

SMDCs and SMDC-Gds were prepared by adding random copolymers into Milli-Q water, shaking for 1 h to fully dissolve, and sonicating for 1 min at room temperature (25 °C). The samples were stored in a 4 °C refrigerator and filtered before use.

## 3.3 SMDC formed by random copolymer $BZA_m$-$PEGA_n$

Twenty $BZA_m$-$PEGA_n$ samples, **P1-P20** illustrated in **Table 2.1**, with different DPs and BZA/PEGA values were polymerized by RAFT polymerization to investigate the effect of polymer parameters on the formation of SMDC. These $BZA_m$-$PEGA_n$ samples were processed by the described preparation methods to form micelles in water. Then, the characteristics, including degree of aggregation (DA), hydrodynamic radius ($R_h$), and radius of gyration ($R_g$), of these micelles were evaluated to determine the appropriate macromolecule structure for the formation of SMDC with the size of 5-7 nm.

### 3.3.1 Formation conditions of SMDC

In the aqueous solution, $BZA_m$-$PEGA_n$ has the potential to either construct the SMDC through intramolecular self-folding or construct the micelle through intermolecular self-assembly as shown in **Figure 3.3**. The DA value of micellar particles formed by $BZA_m$-$PEGA_n$ samples was elucidated to assess the forming conditions. DA represents the ratio of $M_w$ measured by SEC-MALS in a PBS solution to $M_w$ measured by SEC-MALS in a chloroform solution, denoted as $M_{w,\text{ MALS in PBS}}$ / $M_{w,\text{ MALS in chloroform}}$. Since copolymers can dissolve in the relaxed polymer chain state in chloroform solutions but form micelles in aqueous solutions, $M_w$ measured by SEC-MALS in chloroform solution indicated the molecular weight of $BZA_m$-$PEGA_n$ macromolecules, while $M_w$ measured by SEC-MALS in water solution indicated the molecular weight of micellar particles. Therefore, the DA value signified the average number of molecules in one micellar particle in the aqueous solution. The DA value corresponding to the ideal SMDC is one,

and the closer the value is to one, the more favorable the SMDC formation conditions are.

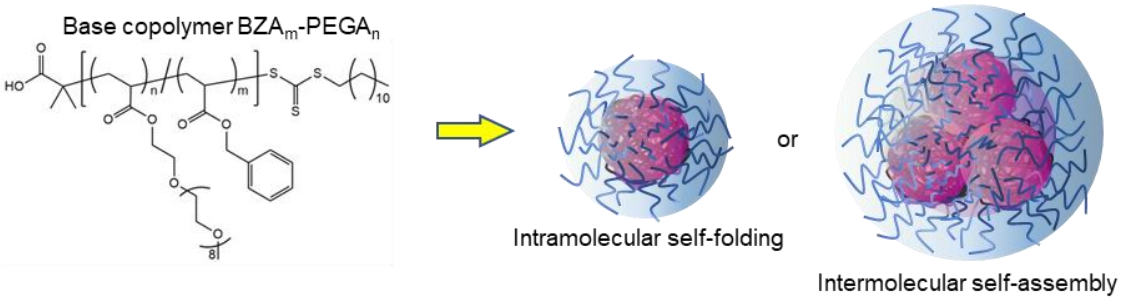


**Figure 3.3**. SMDC constructed through intramolecular self-folding, and the polymeric micelle constructed through intermolecular self-assembly.

The detailed DA values are shown in **Table 3.1**, and the $M_w$ distribution curves in both solvents are depicted in **Figure 3.4**, providing insights into the formation conditions of SMDC. Given that the DP value corresponding to the ideal SMDC backbone should be one. Considering that the formation conditions of SMDC may alter after utilizing CEA as an additional monomer and loading Gd-DOTA as a drug, SMDC with a DA value less than 2.0 can be considered a potential candidate for the backbone structure of SMDC-Gd.

**Table 3.1**. Characterization of random copolymers **P1**-**P20**.

| No. | *dn*/*dc* in PBS[a)] [mL/g] | *dn*/*dc* in $CHCl_3$[b)] [mL/g] | $M_w$ by MALS-PBS[c)] [g/mol] | $M_w$ by MALS-$CHCl_3$[d)] [g/mol] | DA[e)] |
|---|---|---|---|---|---|
| **P1** | 0.1311 | 0.0477 | 22,300 | 27,000 | 0.83 |
| **P2** | 0.1338 | 0.0603 | 26,000 | 17,100 | 1.52 |
| **P3** | 0.1396 | 0.0591 | 47,900 | 16,600 | 2.89 |
| **P4** | 0.1361 | 0.0698 | 149,500 | 17,600 | 8.49 |
| **P5** | 0.1357 | 0.0498 | 42,100 | 40,300 | 1.04 |
| **P6** | 0.1370 | 0.0609 | 47,600 | 42,100 | 1.13 |
| **P7** | 0.1336 | 0.0680 | 62,100 | 35,700 | 1.74 |

| | | | | | |
|---|---|---|---|---|---|
| **P8** | 0.1419 | 0.0697 | 104,500 | 37,900 | 2.76 |
| **P9** | 0.1300 | 0.0496 | 76,600 | 80,800 | 0.95 |
| **P10** | 0.1312 | 0.0596 | 74,400 | 71,300 | 1.04 |
| **P11** | 0.1297 | 0.0651 | 81,800 | 60,100 | 1.36 |
| **P12** | 0.1359 | 0.0684 | 110,000 | 64,400 | 1.71 |
| **P13** | 0.1192 | 0.0537 | 127,100 | 126,600 | 1.00 |
| **P14** | 0.1246 | 0.0519 | 118,200 | 130,200 | 0.91 |
| **P15** | 0.1354 | 0.0547 | 108,300 | 107,600 | 1.01 |
| **P16** | 0.1366 | 0.0686 | 139,000 | 97,800 | 1.42 |
| **P17** | 0.1210 | 0.0535 | 152,800 | 155,500 | 0.98 |
| **P18** | 0.1376 | 0.0641 | 145,800 | 149,000 | 0.98 |
| **P19** | 0.1365 | 0.0614 | 139,300 | 126,900 | 1.10 |
| **P20** | 0.1386 | 0.0701 | 144,700 | 140,700 | 1.03 |

[a)] Refractive index increment of copolymers in phosphate-buffered saline (PBS) solutions; [b)] Refractive index increment of copolymers in chloroform solutions; [c)] Absolute weight-average molecular weight measured by SEC-MALS in PBS; [d)] Absolute weight-average molecular weight measured by SEC-MALS in chloroform; [e)] Degree of aggregation (DA) in water: DA = $M_w$ from SEC-MALS in PBS / $M_w$ from SEC-MALS in chloroform.

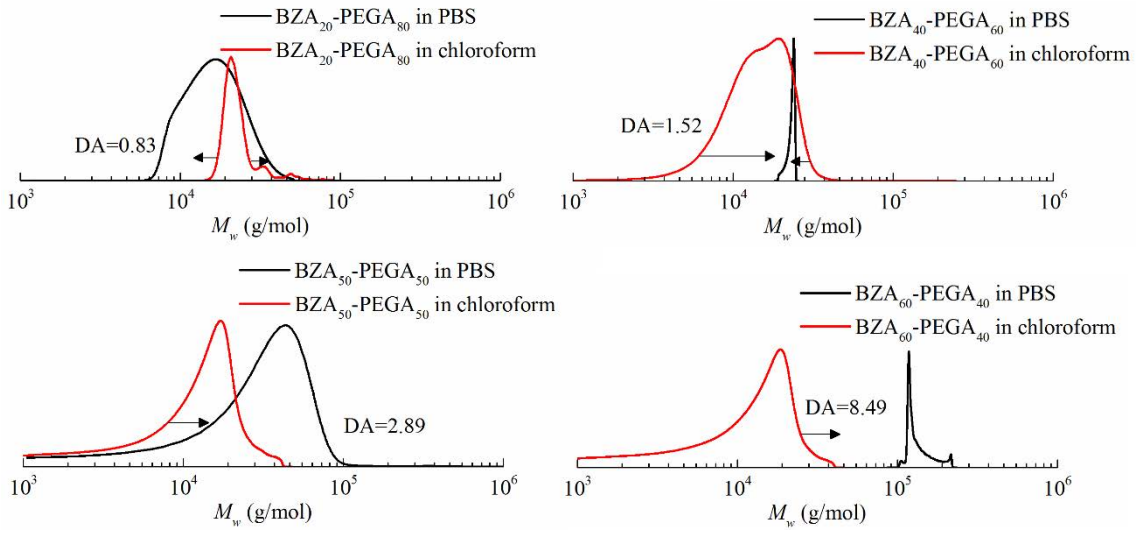

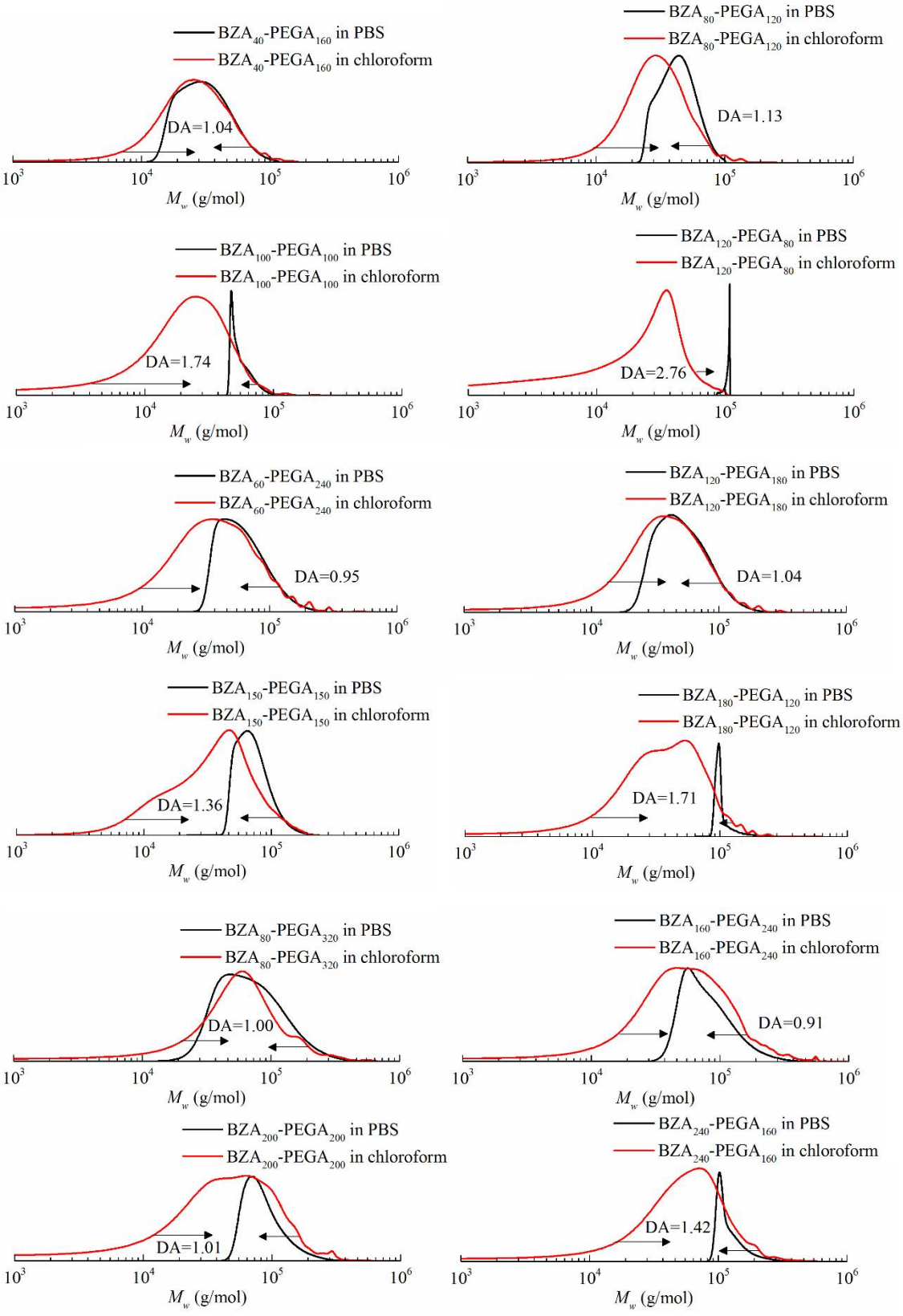
BZA40-PEGA160 in PBS
BZA40-PEGA160 in chloroform
DA=1.04
BZA80-PEGA120 in PBS
BZA80-PEGA120 in chloroform
DA=1.13
BZA100-PEGA100 in PBS
BZA100-PEGA100 in chloroform
DA=1.74
BZA120-PEGA80 in PBS
BZA120-PEGA80 in chloroform
DA=2.76
BZA60-PEGA240 in PBS
BZA60-PEGA240 in chloroform
DA=0.95
BZA120-PEGA180 in PBS
BZA120-PEGA180 in chloroform
DA=1.04
BZA150-PEGA150 in PBS
BZA150-PEGA150 in chloroform
DA=1.36
BZA180-PEGA120 in PBS
BZA180-PEGA120 in chloroform
DA=1.71
BZA80-PEGA320 in PBS
BZA80-PEGA320 in chloroform
DA=1.00
BZA160-PEGA240 in PBS
BZA160-PEGA240 in chloroform
DA=0.91
BZA200-PEGA200 in PBS
BZA200-PEGA200 in chloroform
DA=1.01
BZA240-PEGA160 in PBS
BZA240-PEGA160 in chloroform
DA=1.42
10^3
10^4
10^5
10^6
Mw (g/mol)

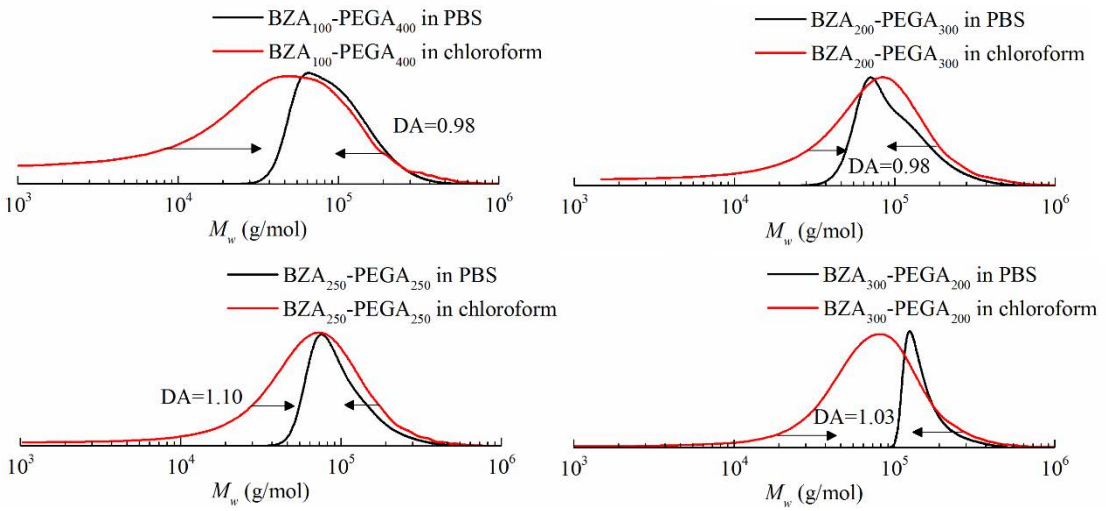


**Figure 3.4**. $M_w$ distribution curves of **P1**-**P20** by MALS in PBS and chloroform.

The three-dimensional plot (**Figure 3.5**) showing the DA values of copolymers with different DP and BZA/PEGA in water, clearly delineated the relationship between SMDC forming conditions and polymer parameters. The result indicated that higher DP values and lower BZA/PEGA ratios tend to bring the DA value closer to 1.0, signifying more optimal conditions for SMDC formation.

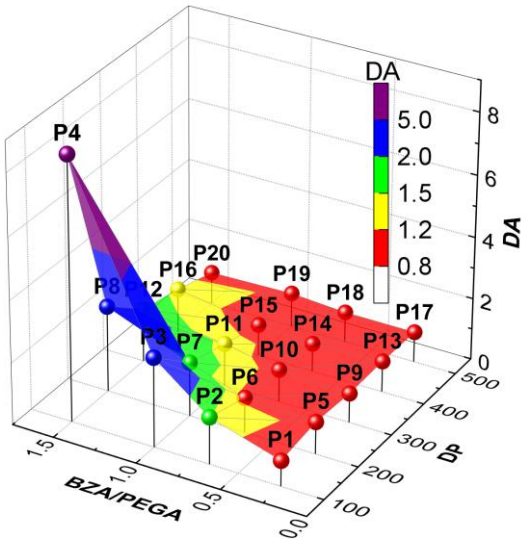


**Figure 3.5**. Three-dimensional plot for DA of **P1**-**P20** versus both DP and BZA/PEGA. The color scale (DA) is a secondary representation of the vertical axis of DA. [copolymer] = 5 mg/mL.

### 3.3.2 The size of SMDC

The size of the SMDC was evaluated, inclusive of $R_h$ measured by dynamic light scattering (DLS) and $R_g$ measured by SEC-MALS and small angle X-ray scattering (SAXS). Considering the critical size for renal excretion is approximately 5 nm in diameter, it is imperative to ensure that the size of the SMDC exceeds 5 nm to prevent rapid excretion before targeting the tumor. This implies that both $R_h$ and $R_g$ should be larger than 2.5 nm. Simultaneously, while a smaller SMDC size enhances penetration into tumor tissue, it is crucial that $R_h$ and $R_g$ are close to, but still larger than 2.5 nm to strike the right balance between efficient tumor targeting and avoidance of premature renal excretion. The $R_h$ measured by DLS and $R_g$ measured by SEC-MALS were assessed for the micellar particles formed by $BZA_m$-$PEGA_n$. The outcomes are presented in **Table 3.2**. Given that diameters below 10 nm approach the minimum accuracy limits of both measurement methods, the recorded values are suitable for relative comparisons but may not precisely characterize the true size of the micelles.

**Table 3.2**. Radius of **P1**-**P20** in water measured by DLS and SEC-MALS.

| No. | $R_g$ (nm)[a)] | $R_h$ (nm)[b)] |
|---|---|---|
| **P1** | 5 | 3 |
| **P2** | 6 | 3 |
| **P3** | 3 | 3 |
| **P4** | 3 | 4 |
| **P5** | 7 | 5 |
| **P6** | 6 | 4 |
| **P7** | 5 | 4 |
| **P8** | 7 | 4 |
| **P9** | 7 | 6 |
| **P10** | 7 | 6 |

| | | |
|---|---|---|
| **P11** | 6 | 4 |
| **P12** | 7 | 4 |
| **P13** | 8 | 9 |
| **P14** | 10 | 7 |
| **P15** | 8 | 6 |
| **P16** | 7 | 5 |
| **P17** | 8 | 10 |
| **P18** | 11 | 8 |
| **P19** | 8 | 7 |
| **P20** | 7 | 7 |

[a)] Radius of gyration of copolymers in phosphate-buffered saline measured by SEC-MALS; [b)] Hydrodynamic radius of copolymers in water measured by DLS.

The 3D distribution maps illustrating $R_h$ and $R_g$ concerning both DP and BZA/PEGA (**Figures 3.6 and 3.7**) clearly depicted the relationship between the size of SMDC and polymer parameters. The findings revealed that higher DP values and lower BZA/PEGA ratios tended to result in larger micelle sizes, both in terms of $R_h$ and $R_g$, indicating less favorable SMDC properties. This trend contrasted with the situation observed in the case of DA, which reflected the SMDC formation conditions.

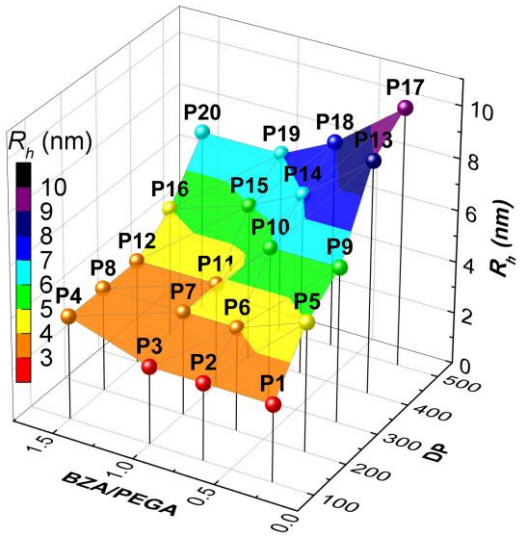


**Figure 3.6**. Three-dimensional plot showing the $R_h$ of copolymers (**P1**-**P20**) with different DP and BZA/PEGA in water. The color scale is a secondary representation of the vertical axis of $R_h$. The $R_h$ was measured by DLS in water at 25 °C. [copolymer] = 5 mg/mL.

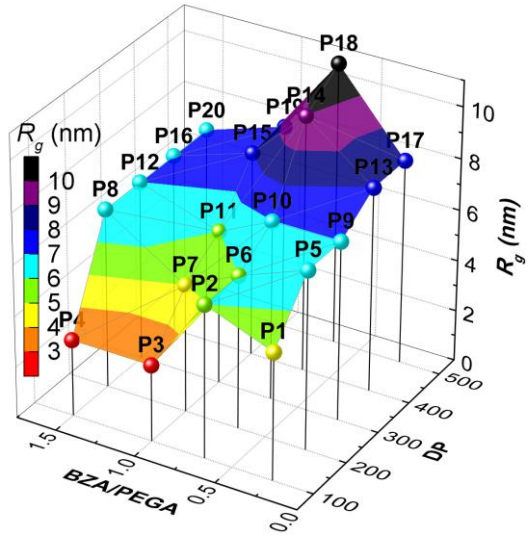


**Figure 3.7**. Three-dimensional plot showing the $R_g$ of copolymers (**P1**-**P20**) with different DP and BZA/PEGA in water. The color scale is a secondary representation of the vertical axis of $R_g$. The $R_g$ was measured by SEC-MALS in PBS at 40 °C. [copolymer] = 5 mg/mL.

In the pursuit of sub-10 nm SMDCs in aqueous environments, the hydrophobic/

hydrophilic ratios and DP values within the ranges of 4/6–5/5 and 200–400 repeating units, respectively, were selected for consideration. Given that hydrophilicity increases upon the utilization of CEA and incorporation of Gd-DOTA, copolymers with a BZA/PEGA value equal to one were chosen as the preferred backbone candidates for the macromolecule to ensure successful SMDC formation. To determine an optimal DP value, the size of SMDC formed by $BZA_m$-$PEGA_n$, where m=n varies from 50 to 250, was meticulously examined using a highly accurate measurement method, namely small-angle X-ray scattering (SAXS). **Figures 3.8** and **3.9** illustrated the Kratky plot, revealing the folding state in water and the relaxed state in the organic solution DMF. The particle size, calculated from the Guinier plot, exhibited a tendency to increase with the increase of DP. To approach the critical glomerular filtration value of 5 nm in diameter, I selected the copolymer **P7** with a DP of 200, specifically $BZA_{100}$-$PEGA_{100}$, as the backbone for the final macromolecule to form SMDC.

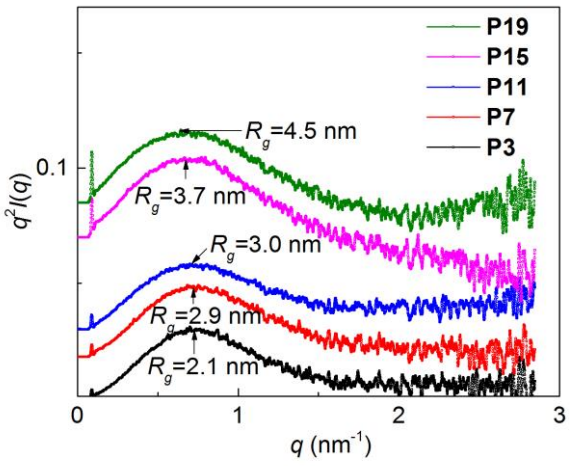


**Figure 3.8**. SAXS Kratky plots of copolymers (**P3**, **P7**, **P11**, **P15**, and **P19**) in water at 25 °C: [copolymer] = 10 mg/mL.

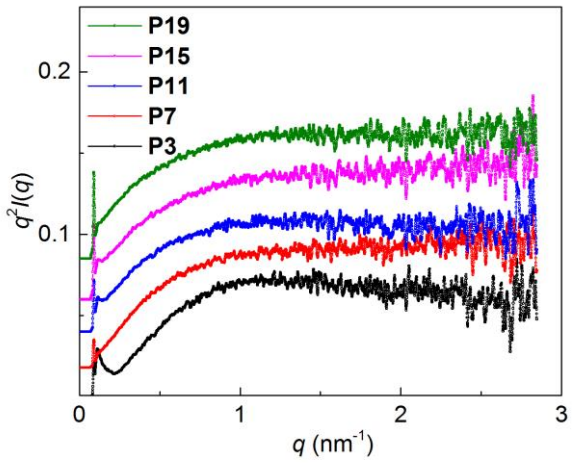


**Figure 3.9**. SAXS Kratky plots of copolymers (**P3**, **P7**, **P11**, **P15**, and **P19**) in DMF at 25 °C: [copolymer] = 10 mg/mL.

For a clearer visual assessment of the resulting SMDC, TEM images of **P7** were acquired. Over 10 images, featuring more than 500 particles, were compiled to provide a comprehensive size distribution. **Figure 3.10** illustrates the size distribution and the formation conditions of the SMDC, showcasing direct observations of both SMDC and small quantities of aggregated micelles.

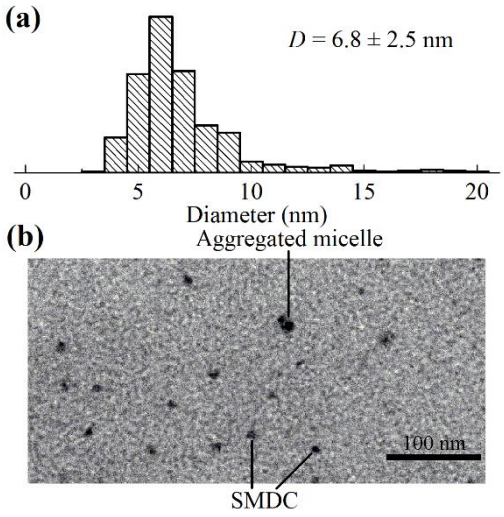


**Figure 3.10**. (a) Size distribution and (b) image by TEM measurement of the base copolymer **P7** at 25 °C. The scale bar, 100 nm.

### 3.3.3 Stability and shelf-life of SMDC

The stability of SMDC samples was evaluated by $R_h$ in 50 days and the shelf-life was calculated using mean count rate (MCR) value, which meant the actual average number of photons per second arriving at the detector, measured by DLS as shown in **Figure 3.11**. The size of SMDC could keep stable for 50 days at 4 °C, 25 °C, and 40 °C. Samples stored at 60 °C were observed to rapidly undergo a liquid-solid phase transition in Milli-Q solution, thus only the parameters of samples stored at 4 °C, 25 °C, and 40 °C in 50 days were used to calculate the shelf-life.

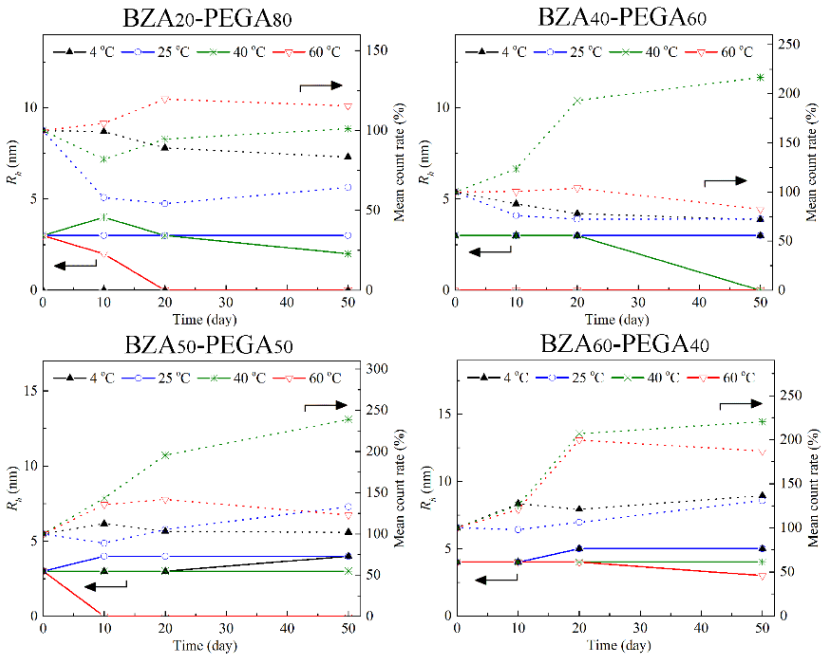

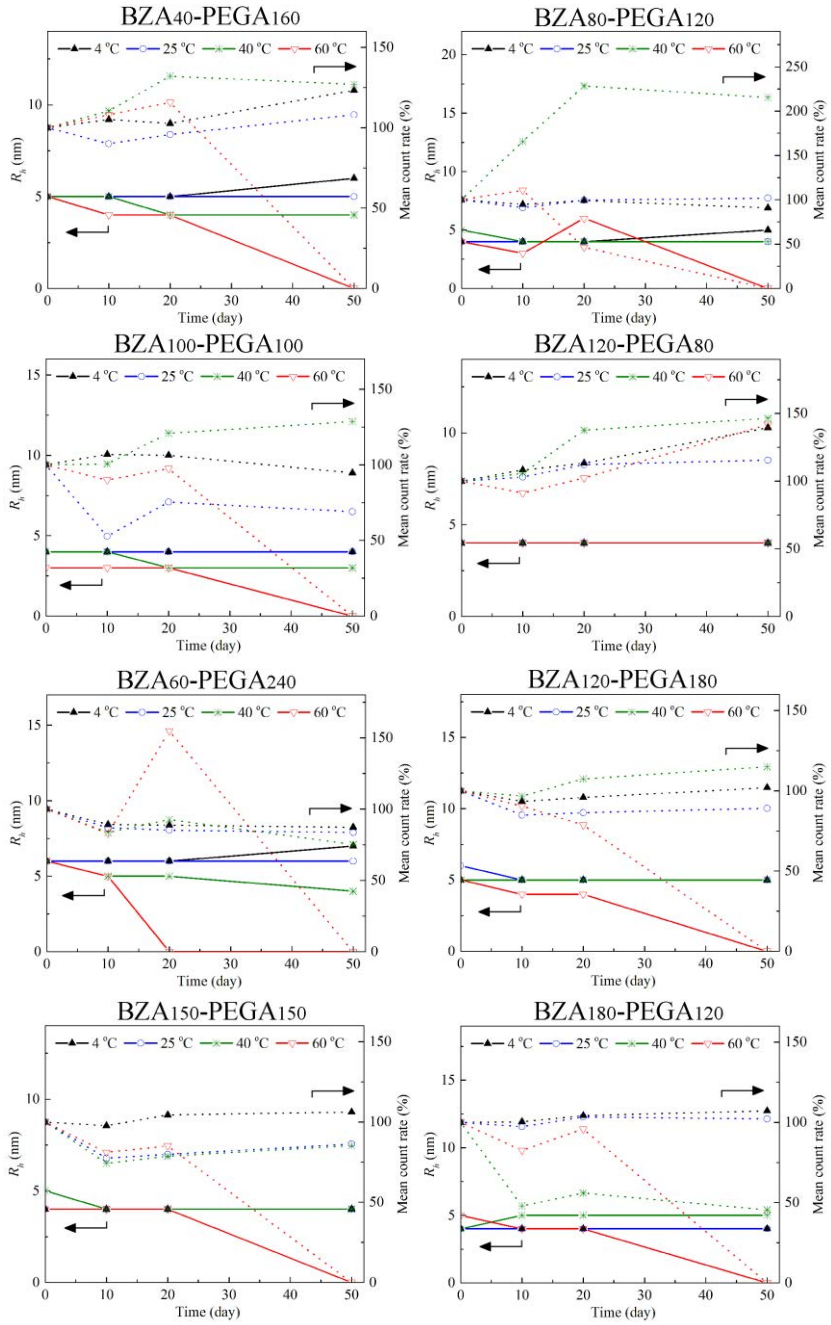
BZA40-PEGA160
BZA80-PEGA120
BZA100-PEGA100
BZA120-PEGA80
BZA60-PEGA240
BZA120-PEGA180
BZA150-PEGA150
BZA180-PEGA120
4 °C
25 °C
40 °C
60 °C
Time (day)
Mean count rate (%)

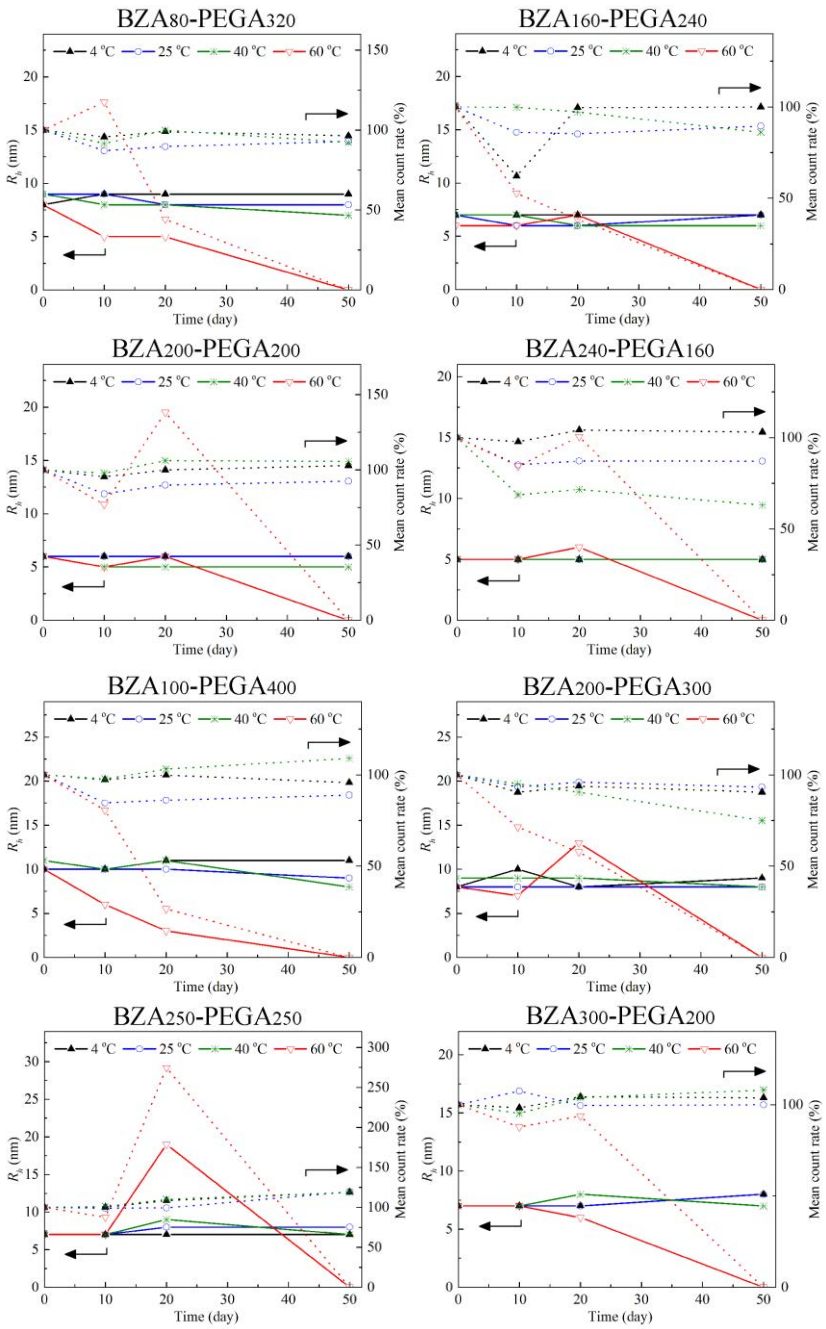


**Figure 3.11**. $R_h$ and MCR of copolymers P1-P20 in water by DLS at 4 °C, 25 °C, and 40 °C within 50 days: [copolymer] = 10 mg/mL.

The shelf life of samples was calculated according to Arrhenius law [6]. 50% change of MCR was set as the threshold for evaluating sample deterioration. The linear relationship between temperature $1/T$ and the reaction rate constant log $K$ is shown as

following equation.

$$\log K = \log A - Ea/2.303RT \qquad \textbf{(Equation 3.1)}$$

Where $K$ is degradation rate constant, $A$ is pre-exponential factor, $Ea$ is energy of activation, $R$ is gas constant, and $T$ is temperature. As the degradation and deterioration of SMDC do not depend on the sample concentration, the degradation/deterioration of SMDC was treat as a zero-order reaction. Plot the MCR versus day distribution of samples at different temperatures ($T$), calculate the day ($S$) when MCT exceeds the threshold value on the fitting straight line. Then plot the log $S$ versus $1/T$ distribution and draw a fitting straight line, the $S$ value corresponding to 4 °C on the straight line is the shelf life of the sample under refrigeration.

The result as shown in **Table 3.3**, SMDC samples stored as 4 °C could always achieve a long-time stable in both size and MCR. Since the size of SMDC formed by samples with low DP values was close to the critical value of DLS measurement, the calculated low stability of samples with DP=100 was mainly caused by the inaccurate measurement results. However, the too high DP value (DP=500) will cause the stability lower than other samples irrespective of measurement accuracy. On the other hand, the balance of hydrophilicity and hydrophobicity (BZA/PEGA equal to 5/5 or 4/6) was observed to contribute to the better stability. Proper parameter selection could allow the SMDC to achieve a shelf life of more than one year at 4 °C.

**Table 3.3**. Shelf life of **P1**-**P20** in water at 4 °C.

| No. | Fitting line[a)] | Log[S] at 4 °C[b)] | Shelf life (day)[c)] |
|---|---|---|---|
| **P1** | Y = -1.290X+6.584 | 1.930 | 85 |
| **P2** | Y = 1.341X-2.873 | 1.965 | 92 |
| **P3** | Y = 3.585X-10.170 | 2.765 | 582 |
| **P4** | Y = 1.087X-2.017 | 1.905 | 83 |
| **P5** | Y = 0.211X+1.539 | 2.300 | 200 |
| **P6** | Y = 2.073X-4.384 | 3.095 | 1246 |

| | | | |
|---|---|---|---|
| **P7** | Y = 3.595X-9.840 | 3.131 | 1351 |
| **P8** | Y = 0.163X+1.331 | 1.919 | 83 |
| **P9** | Y = 0.480X+0.460 | 2.192 | 156 |
| **P10** | Y = 3.148X-8.023 | 3.335 | 2163 |
| **P11** | Y = 1.461X-2.716 | 2.555 | 359 |
| **P12** | Y = 1.948X-4.231 | 2.797 | 627 |
| **P13** | Y = 0.789X-0.127 | 2.720 | 524 |
| **P14** | Y = 0.757X-0.203 | 2.528 | 337 |
| **P15** | Y = 1.706X-3.068 | 3.087 | 1222 |
| **P16** | Y = 2.691X-6.860 | 2.849 | 707 |
| **P17** | Y = 0.868X-0.454 | 2.678 | 476 |
| **P18** | Y = 0.666X+0.021 | 2.424 | 265 |
| **P19** | Y = 0.004X+2.133 | 2.147 | 140 |
| **P20** | Y = 0.286X+1.938 | 2.970 | 933 |

[a)] Fitting line for log *S* versus 1/*T* distribution of copolymers at 4 °C; [b)] Log[S] values calculated from the fitting line; [c)] The stability period of micelles at 4 °C calculated from the fitting line.

## 3.4 SMDC-Gd formed by random terpolymer $BZA_m$-$PEGA_n$-$CEA_k$(Gd-DOTA)$_j$

Based on the above results, **P7** was selected as the platform equipped with appropriate balance of hydrophobic/hydrophilic components. Subsequently, Random terpolymers, namely, $BZA_{100}$-$PEGA_{90}$-$CEA_{10}$ (**TP1**), $BZA_{100}$-$PEGA_{80}$-$CEA_{20}$ (**TP2**), and $BZA_{100}$-$PEGA_{70}$-$CEA_{30}$ (**TP3**), were synthesized through RAFT polymerization with PEGA, BZA, and 2-carboxyethyl acrylate (CEA) as monomers. The moiety of *S*-2-(4-aminobenzyl)-DOTA was incorporated into **TP1**-**TP3** by a condensation reaction, followed by the formation of Gd chelates on the side chain of DOTA-conjugated

terpolymers, resulting in the production of $BZA_m$-$PEGA_n$-$CEA_k(Gd\text{-}DOTA)_j$ (**TP4-TP6**). On average, **TP4** equipped four Gd-DOTA molecules, **TP5** equipped nine Gd-DOTA molecules, and **TP6** equipped 17 Gd-DOTA molecules (**Figure 3.12**). Gd-DOTA-conjugated copolymers without hydrophobic components were prepared as control samples (PEGA-$Gd_4$ and PEGA-$Gd_{12}$). The gadolinium chelate-loaded SMDC (SMDC-Gd) formed by **TP4-TP6** through self-folding, referred to as SMDC-$Gd_4$, SMDC-$Gd_9$, and SMDC-$Gd_{17}$, were characterized in terms of DA, hydrodynamic radius ($R_h$), and radius of gyration ($R_g$).

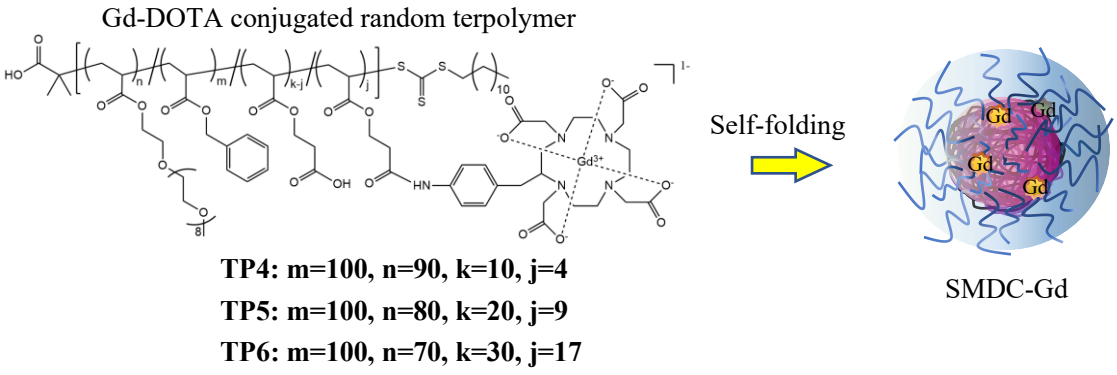


**Figure 3.12**. Chemical structure of Gd-conjugated random terpolymers (**TP4-TP6**) and schematic illustration of the SMDC-Gd formation.

### 3.4.1 Formation conditions of SMDC-Gd

The DA values of **TP4-TP6**, derived from SEC-MALS results, were determined to be 0.91, 0.88, and 0.53, as indicated in **Table 3.4**. Given that the molecular weights of terpolymers measured by SEC-MALS aligned with the intended value and were consistent with molecular weights obtained by GPC and NMR, except for the $M_w$ of **TP6** in chloroform, these DA values strongly suggested the successful formation of SMDC-Gds. Meanwhile, it is noteworthy that **TP6** exhibited partial formation of a reverse micelle structure in chloroform.

**Table 3.4**. Characterization of random copolymers **TP4**-**TP6**.

| No. | *dn*/*dc* in PBS[a)] [mL/g] | *dn*/*dc* in $CHCl_3$[b)] [mL/g] | $M_w$ by MALS-PBS[c)] [g/mol] | $M_w$ by MALS-$CHCl_3$[d)] [g/mol] | DA[e)] |
|---|---|---|---|---|---|
| **TP4** | 0.1334 | 0.0691 | 82,100 | 89,900 | 0.91 |
| **TP5** | 0.1369 | 0.0718 | 75,700 | 86,000 | 0.88 |
| **TP6** | 0.1363 | 0.0778 | 74,900 | 142,400 | 0.53 |

[a)] Refractive index increment of copolymers in phosphate-buffered saline (PBS) solutions; [b)] Refractive index increment of copolymers in chloroform solutions; [c)] Absolute weight-average molecular weight measured by SEC-MALS in PBS; [d)] Absolute weight-average molecular weight measured by SEC-MALS in chloroform. [e)] Degree of aggregation (DA) in water: DA= $M_w$ from SEC-MALS in PBS/$M_w$ from SEC-MALS in chloroform.

### 3.4.2 The size of SMDC-Gd

To compare the character differences among SMDC-Gds with varying amounts of Gd loading in each molecule, SMDC-$Gd_4$ and SMDC-$Gd_{17}$ were selected as candidates for application in MRI and Gd-NCT. The sizes of SMDC-Gds, including $R_h$ measured by DLS, and $R_g$ measured by SAXS, were confirmed. As previously mentioned, both $R_h$ and $R_g$ suggested to be close to but larger than 2.5 nm to achieve optimal penetration into tumor tissue while preventing the rapid excretion of SMDC-Gds before reaching the targeted tumor.

**Figure 3.13** illustrates the $R_h$ of SMDC-Gd samples measured by DLS. Both SMDC-Gds exhibited sizes in the range of 5-7 nm with narrow distributions, almost reaching the critical value for glomerular filtration. Meanwhile, the $R_h$ of SMDC-$Gd_{17}$ was slightly smaller than that of SMDC-$Gd_4$. Furthermore, the ζ potential of SMDC-Gds was measured using the Zetasizer machine (**Figure 3.14**), SMDC-$Gd_4$ and SMDC-$Gd_{17}$ showed a 1.5-fold difference in ζ potential values. Additionally, SMDC-$Gd_4$ and PEGA-

$Gd_4$ displayed similar values. This discrepancy in ζ potential values could be attributed to the differing amounts of $(Gd\text{-}DOTA)^-$ and CEA without Gd-DOTA present in these two of SMDC-Gd samples.

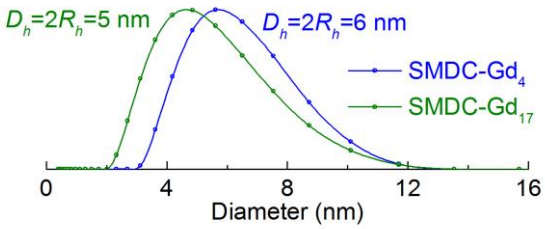


**Figure 3.13**. Size distributions of SMDC-Gds measured by DLS at 25 °C: [copolymer] = 10 mg/mL.

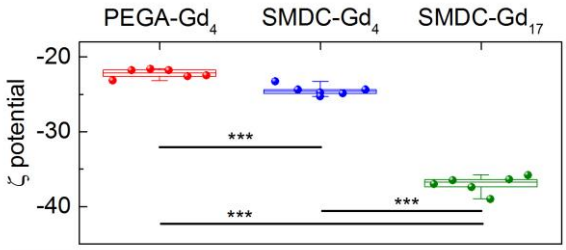


**Figure 3.14**. ζ potentials of SMDC-Gds measured by Zetasizer at 25 °C: [copolymer] = 10 mg/mL. Data are shown as box plot, $n = 6$, $^{***}p < 0.001$.

The $R_g$ and folding state of samples were investigated through SAXS measurements. The Kratky plots from SAXS in water (**Figure 3.15**) indicated the formation of SMDC-Gds by **TP4**-**TP6** in the aqueous solution, with the diameter of 5-6 nm. It also highlighted the relaxed polymer chain conditions of hydrophilic control groups, PEGA-Gds. Simultaneously, the plots from SAXS in DMF (**Figure 3.16**) suggested the relaxed polymer chain state of **TP4** and PEGA-Gds in the organic solvent DMF. Notably, **TP5** and **TP6** exhibited the reverse micelle formation in both water and DMF.

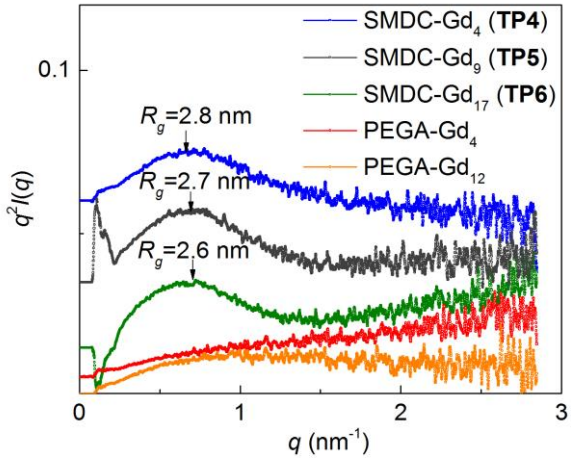


**Figure 3.15**. SAXS Kratky plots of Gd-loaded copolymers in water at 25 °C: [copolymer] = 10 mg/mL.

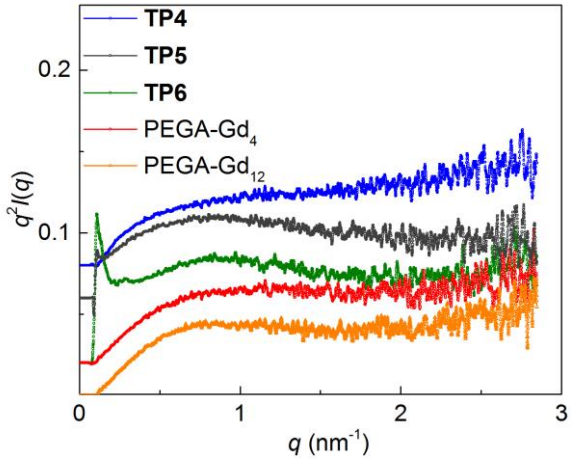


**Figure 3.16**. SAXS Kratky plots of Gd-loaded copolymers in DMF at 25 °C: [copolymer] = 10 mg/mL.

For a more visually accessible examination of the formed SMDC-$Gd_4$ and SMDC-$Gd_{17}$, TEM images were acquired. Over 10 images, more than 500 particles were gathered to depict the size distribution. The size distribution and formation conditions of SMDC-Gd samples were illustrated in **Figure 3.17**. Both SMDC-$Gd_4$ and SMDC-$Gd_{17}$ were directly observed with the diameter of 5-7 nm, and the average size of SMDC-$Gd_{17}$ was approximately 2 nm smaller than that of SMDC-$Gd_4$.

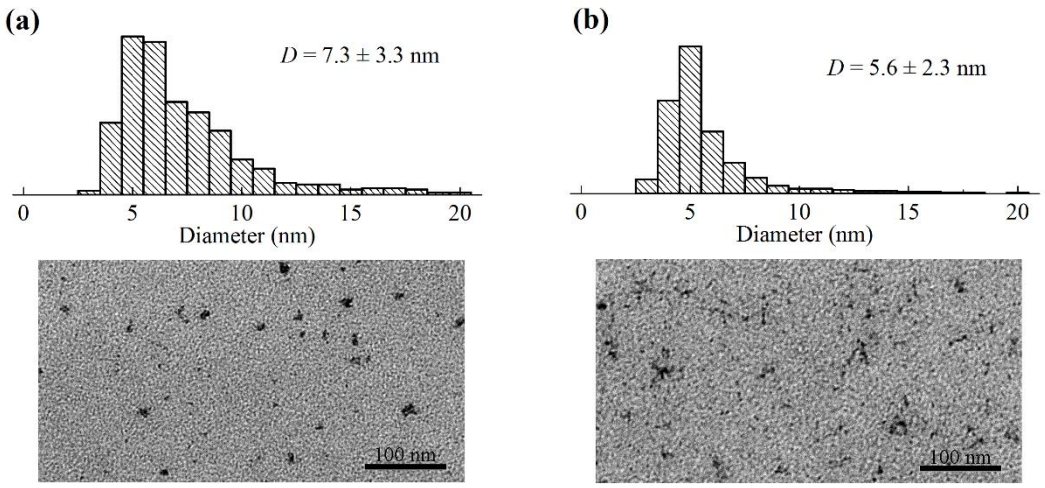


**Figure 3.17**. TEM images and diameter distributions of (d) SMDC-$Gd_4$ and (e) SMDC-$Gd_{17}$ at 25 °C. Scale bars, 100 nm.

### 3.4.3 Stability and shelf-life of SMDC-Gd

The stability of SMDC-$Gd_4$ and SMDC-$Gd_{17}$ was assessed by monitoring the $R_h$ over a period of 50 days, and the shelf life was determined based on the $M_w$ measured by SEC-MALS, as shown in **Figure 3.18**. The samples were stored at 4 °C, 25 °C, and 40 °C, returned to room temperature prior to measurement, and analyzed by DLS at 25 °C and SEC-MALS at 40 °C. The results demonstrated that the size of SMDC-Gds remained stable over the period of 40 days. The shelf life of SMDC-Gds was calculated using the Arrhenius law, with a 10% change in $M_w$ set as the threshold for assessing sample deterioration. The findings revealed that SMDC-$Gd_4$ could remain stable for approximately one year when stored at 4 °C, whereas SMDC-$Gd_{17}$ exhibited a shelf life of only 4 months under the same condition.

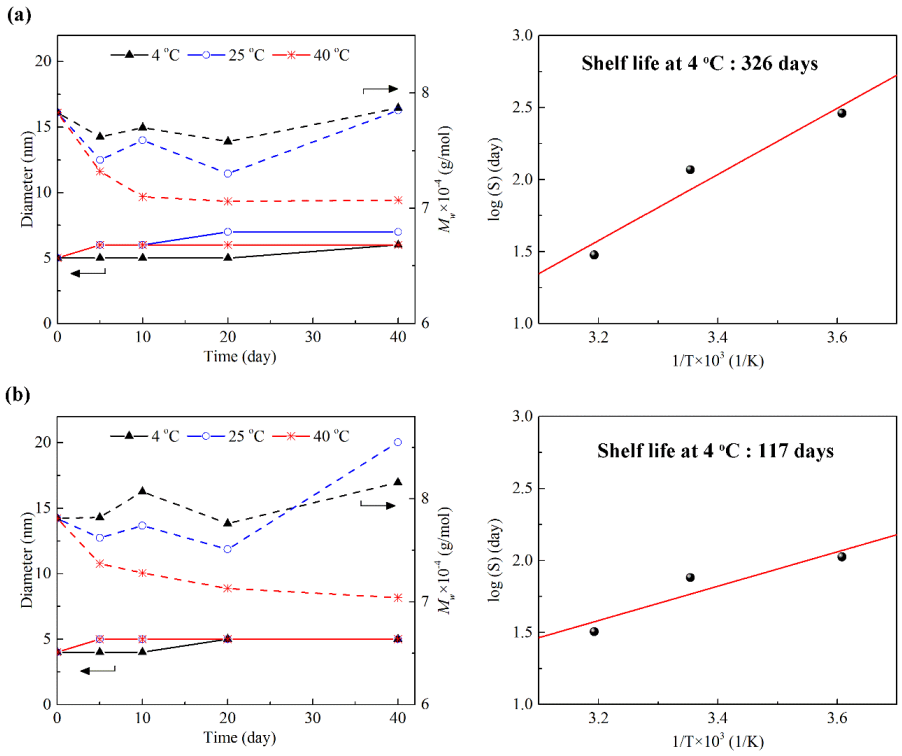


**Figure 3.18**. The stability and shelf life of (a) SMDC-$Gd_4$ and (b) SMDC-$Gd_{17}$.

## 3.5 Summary

The SMDCs, constructed by the synthesized random copolymers $BZA_m$-$PEGA_n$ with varying DPs and BZA/PEGA values, underwent comprehensive characterization. This analysis aimed to elucidate the relationship between the characteristics of SMDC formation and various polymer parameters. Based on an in-depth understanding of SMDC forming traits, this research identified the appropriate polymer parameters for effective SMDC formation, Notably, $BZA_{100}$-$PEGA_{100}$ emerged as the preferred candidate backbone for SMDC. Subsequently, leveraging the identified backbone structure, random terpolymers $BZA_m$-$PEGA_n$-$CEA_k(Gd\text{-}DOTA)_j$ were synthesized and analyzed by SEC-MALS, DLS, SAXS, and TEM. These random terpolymers demonstrated the ability of self-folding to form SMDC-$Gd_4$, SMDC-$Gd_9$, and SMDC-$Gd_{17}$ in water, respectively, with the diameter of 5-7 nm. All these prepared SMDCs and SMDC-Gds could keep

stable for more than 40 days stored at 4 °C.

## 3.6 References

[1] Aiertza MK, Odriozola I, Cabañero G, Grande HJ, Loinaz I. Single-chain polymer nanoparticles. Cellular and Molecular Life Sciences, **2012**, 69(3): 337-346.

[2] Hirai Y, Terashima T, Takenaka M, Sawamoto M. Precision self-assembly of amphiphilic random copolymers into uniform and self-sorting nanocompartments in water. Macromolecules, **2016**, 49(14): 5084-5091.

[3] Ter Huurne GM, Palmans ARA, Meijer EW. Supramolecular single-chain polymeric nanoparticles. CCS Chemistry, **2019**, 1(1): 64-82.

[4] Kröger APP, Paulusse JMJ. Single-chain polymer nanoparticles in controlled drug delivery and targeted imaging. Journal of controlled release, **2018**, 286: 326-347.

[5] Matsumoto M, Terashima T, Matsumoto K, Takenaka M, Sawamoto M. Compartmentalization technologies via self-assembly and cross-linking of amphiphilic random block copolymers in water. Journal of the American Chemical Society, **2017**, 139(21): 7164-7167.

[6] Fan Z, Zhang L. One-and two-stage Arrhenius models for pharmaceutical shelf life prediction. Journal of Biopharmaceutical Statistics, **2015**, 25(2): 307-316.

# Chapter 4. *In vitro* and *in vivo* properties of SMDC-Gd

## 4.1 Introduction

For cancer imaging and therapy in this research, the chosen payload for the SMDC was Gd-DOTA, a widely clinically used and studied Gd chelate in MRI [1-2]. However, Gd chelates have been found to exhibit various forms of bio-toxicity in research and applications, including, but not limited to, nephron-toxicity, hepato-toxicity, and hemato-toxicity [3-5]. Consequently, the key challenge in the development of Gd-based agents is to control the Gd administration dose within safe limits while ensuring optimal imaging/therapeutic effects. Recent studies have highlighted the importance of enhancing the tumor-targeting ability of Gd-loaded DDS to improve the efficiency of Gd-based imaging/therapeutic agents [6-7]. This approach allows for an enhancement of the effectiveness without the need to increase the administration dose.

Within this chapter, an *in vitro* cell viability assay and the Gd leak assay were carried out to evaluate the cytotoxicity and stability of samples. Subsequently, an *in vivo* biodistribution of SMDC-Gds was investigated to analyze their tumor-targeting proficiency, blood clearance rates, and organ accumulation patterns. The goal was to identify the most suitable imaging and therapeutic strategy that ensures optimal tumor targeting accumulation. To validate the safety during imaging and therapy, an *In vivo* biotoxicity single-dose assay was executed using the selected SMDC-Gd sample and administration dose. This assessment involved evaluating blood and plasma indicators. The findings from these experiments were pivotal in determining the strategies aligned with the distinctive properties of SMDC-Gd.

## 4.2 Materials and methods

### 4.2.1 Cell lines and animals

Murine colon carcinoma 26 (CT26) cell was purchased from ATCC (Manassas, VA, USA). The cell was subcultured in Dulbecco's Modified Eagle Medium (DMEM) with 10% fetal bovine serum (FBS) and 1% penicillin (Merck Millipore, Burlington, MA, USA); this was maintained at 37 °C in an incubator (5% $CO_2$, 95% humidified environment). All animal experiments were approved by the Animal Care and Use Committee and performed in accordance with the Guidelines for the Care and Use of Laboratory Animals set forth by Tokyo Institute of Technology, the National Institutes for Quantum Science and Technology, and Kyoto University.

### 4.2.2 Cell viability assay

Cell viability was investigated using cell counting kit-8 (CCK-8; Dojindo Molecular Technologies Inc., Kumamoto, Japan). CT26 cells (10,000 cells/50 μL) were cultured in DMEM containing 10% FBS in a 96-well multiplate. The cells were incubated for 24 h and then exposed to Gd-DOTA, PEGA-$Gd_4$, SMDC-$Gd_4$, and SMDC-$Gd_{17}$ in multiple concentrations (n = 5) for 48 h. The CCK-8 reagent (10 μL) was added, the cells were and then incubated for 1 h. The absorbance of media was measured at 450 nm using an iMark microplate reader (Bio-Rad Laboratories Inc., Hercules, CA, USA).

### 4.2.3 Gd-leakage assay

1 M HEPES buffer (pH 7.4 at 37 °C) with 150 mM NaCl and 10 mg/mL BSA was prepared to simulate the physiological environment. PEGA-$Gd_4$, SMDC-$Gd_4$, and SMDC-$Gd_{17}$ were each dissolved in 5 mL buffer, and the Gd concentration was measured by inductively coupled plasma mass spectrometry (ICP-MS) using a Shimadzu ICPMS-2030 (Shimadzu Corporation, Kyoto, Japan). Each sample solution was put in a dialysis bag (Spectra/Por dialysis membrane, MWCO of 3.5 kD) against 45 mL of the same buffer at 37 °C. 1.5 mL of dialysate outside the dialysis bag were taken at 1, 2, 3, 5, and 10 days, and the Gd concentration was measured by ICP-MS.

### 4.2.4 Biodistribution study

BALB/c mice (6 weeks old, female, Japan SLC Inc., Hamamatsu, Japan) with colon tumors were prepared for a biodistribution study. The mice were inoculated subcutaneously with CT26 ($1 \times 10^6$ cells/mouse) cells. Ten-days post-inoculation, the mice were separated into four groups (n = 6), intravenously injected with Gd-DOTA, PEGA-$Gd_4$, SMDC-$Gd_4$, and SMDC-$Gd_{17}$ *via* the tail vein at 5 mg/kg of Gd. The mice were sacrificed at 1 h, 4 h, 8 h, 24 h, and 72 h after administration. Blood was collected and centrifuged to obtain the plasma. Tumors and organs, including the liver, spleen, kidney, muscle, pancreas, and brain, were excised, washed with PBS, and weighed. All samples were mixed with nitric acid (concentration = 70 %, 1 mL), and acid digestion was carried out using EYELA MG-2300 (Tokyo Rikakikai CO. LTD., Tokyo, Japan). The obtained solutions were diluted by Milli-Q water, and the Gd concentration in each sample was measured by inductively coupled plasma mass spectrometry (ICP-MS) using an Agilent 7700x ICP-MS (Agilent Technologies Inc., Santa Clara, California, USA).

### 4.2.5 Blood parameter assay

BALB/c mice (6 weeks old, female, Japan SLC Inc., Hamamatsu, Japan) were used for biotoxicity assay. The mice were separated into four groups (n = 5). PBS (200 μL), Gd-DOTA, PEGA-$Gd_4$, and SMDC-$Gd_4$ (0.1 mmol/kg based on Gd) were intravenously injected via the tail vein. The mice were sacrificed at 4 h and 48 h after administration. Blood was collected, and 90 μL of blood was placed in a 500 μL tube containing ethylenediaminetetraacetic acid (EDTA, Dojindo Molecular Technologies Inc.) aqueous solution (10 μL, conc. = 12 mg/mL in Milli-Q water). The other blood volume was centrifuged to obtain the plasma. The whole blood with EDTA was measured using an automatic multiple blood cell counter pocH-100iV Diff (Sysmex Corporation, Kobe, Hyogo, Japan) for white blood cell (WBC), red blood cell (RBC), hemoglobin (HGB), hematocrit (HCT) and platelet (PLT) analysis. The plasma was measured by Dri-Chem 7000IZ (Fujifilm Wako Pure Chemical Corporation, Japan) for blood urea nitrogen (BUN), creatinine (CRE), glutamic-pyruvic transaminase (GPT), glutamic-oxaloacetic

transaminase (GOT), alkaline phosphatase (ALP) and total protein (TP) analysis.

## 4.3 *In vitro* performance of SMDC-Gd

### 4.3.1 Cell viability assay

The cytotoxicity of selected Gd-loaded samples, SMDC-$Gd_4$, SMDC-$Gd_{17}$, and PEGA-$Gd_4$, was examined and compared to that of the small molecular control group, Gd-DOTA. The evaluation of cytotoxicity was based on the cell viability of CT26 cells exposed to the samples, as shown in **Figure 4.1**. The results revealed that, even at a Gd concentration of 1 mM, an unusually high concentration rarely surpassed in clinical applications, all samples exhibited no significant cytotoxic effects. The non-significant cytotoxicity of Gd-loaded agents was confirmed, suggesting the safety of this structure for the delivery of various agents. Consequently, the SMDC platform hold promise as a secure means for the transport of diverse agents, enhancing its potential utility in clinical application.

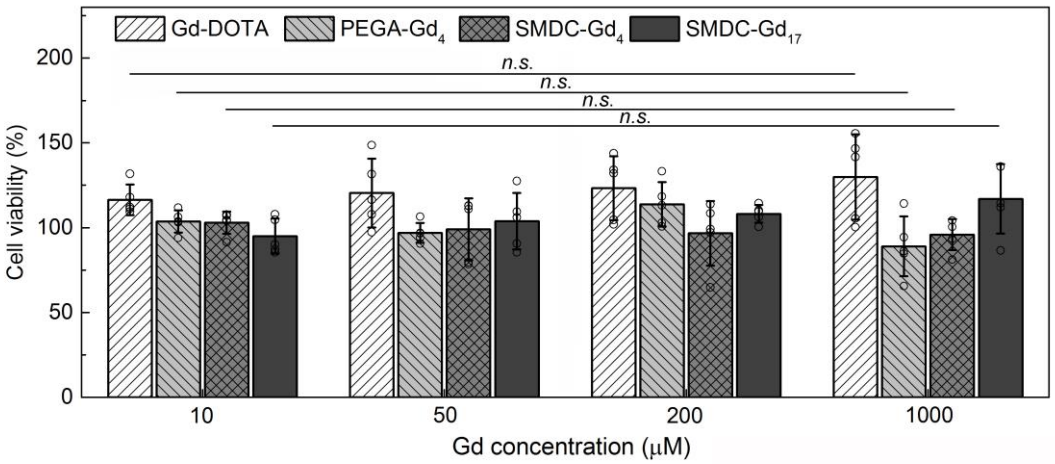


**Figure 4.1**. Cell viability of CT26 cells treated with Gd-conjugated agents.

Data are shown as mean ± s.d., $n = 6$. *n.s.* $p \geq 0.05$.

### 4.3.2 Gd-leakage assay

Since the Gd chelate was incorporated in SMDC by a peptide bond and the release of Gd was not required in body for MRI and Gd-NCT. Therefore, the Gd-leakage of SMDC-Gds caused by the break of peptide bond or chelate structure was evaluated. Ten-days incubation in physiological conditions, i.e., HEPES buffer (1 M, pH 7.4 at 37 °C) with NaCl (150 mM) and BSA (10 mg/mL), showed almost no release of Gd ion from SMDC (**Figure 4.2**), indicating an appropriate tolerance of SMDC-Gds as systemically injectable agents.

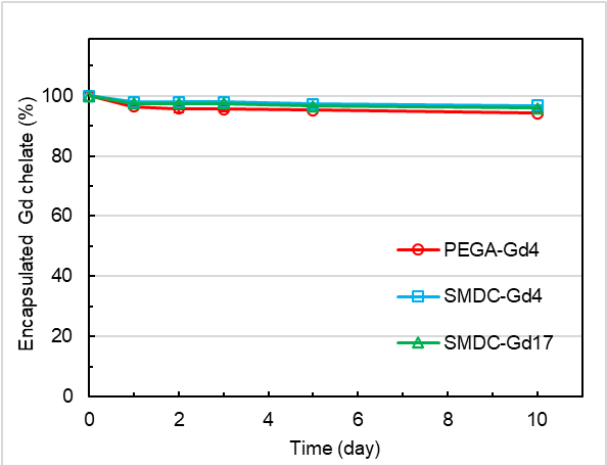


**Figure 4.2**. Gd-leakage in HEPES buffer (1 M, pH 7.4) with NaCl (150 mM) and BSA (10 mg/mL) at 37 °C in 10 days. Data are means ± s.d., $n$ =3.

## 4.4 *In vivo* performance of SMDC-Gd

### 4.4.1 Biodistribution study

The research on biodistribution with the SMDC system aimed to elucidate the advantages of self-folding for tumor-targeting applications. SMDC-Gds were tested against CT26-bearing mice and compared with control groups, PEGA-$Gd_4$ and Gd-DOTA. As anticipated, Gd-DOTA exhibited rapid blood clearance and low accumulation in the tumor model and organs. Plasma clearance profiles demonstrated comparable blood

circulation and clearance abilities for SMDC-$Gd_4$ (10.2±2.1%ID/g at 24 h and 1.3±0.3%ID/g at 72 h) and PEGA-$Gd_4$ (11.7±1.4%ID/g at 24 h and 3.5±1.3%ID/g at 72 h), while SMDC-$Gd_{17}$ (0.5±0.06%ID/g at 24 h and 0.05±0.004%ID/g at 72 h) displayed relatively rapid elimination (**Figure 4.3**). Enhanced tumor accumulation was observed for SMDC-$Gd_4$ (13.1±4.4%ID/g at 24 h), with over two-fold Gd concentration compared to that of SMDC-$Gd_{17}$ (6.1±0.7%ID/g at 24 h) and PEGA-$Gd_4$ (5.3±2.2%ID/g at 24 h) at 24 h post-administration (**Figure 4.4**). These findings strongly suggested that self-folding could create a PEGylated outer layer around SMDC, allowing anti-aggregation and anti-protein binding functionality after intravenous injection.

The accumulation patterns of SMDC-$Gd_4$ in other major organs were comparable to typical nanomedicines [8-10]. Meanwhile, SMDC-$Gd_{17}$ exhibited higher accumulation in the liver, spleen, and kidney (**Figures 4.5-4.7**). SMDC-$Gd_4$ and SMDC-$Gd_{17}$ had an approximately 1 nm difference in diameter, and their ζ potential values differed by 1.5-fold. Notably, SMDC-$Gd_4$ and PEGA-$Gd_4$ displayed similar ζ potentials. Since the physicochemical properties of drug carriers significantly influence their fate in the body, molecular design, size control, and surface charge played crucial roles. Generally, neutral to slightly negative surface charges could prevent nonspecific interactions with plasma proteins, avoiding quick clearance by the mononuclear phagocyte system. However, SMDC-$Gd_{17}$ (ζ potential = −37mV) exhibited an exceedingly negative charge, leading to proactive uptake by hepatic nonparenchymal cells, such as Kupffer cells and macrophages, through scavenger receptor-mediated endocytosis. Additionally, the low Gd concentration in the brain indicated a low risk of serious side effects towards brain (**Figure 4.8**), while low Gd concentration in muscle suggested the potential to minimize background signals in MRI (**Figure 4.9**).

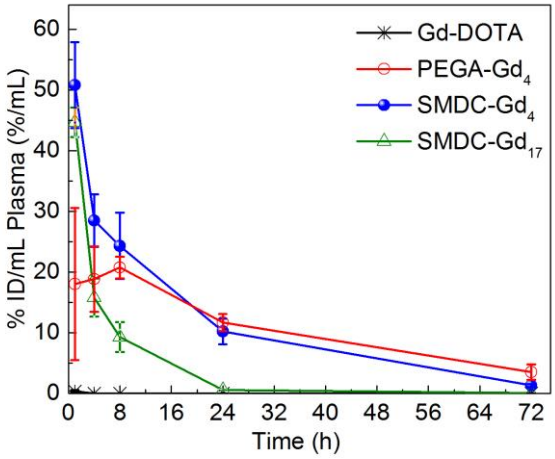


**Figure 4.3**. Time profiles of Gd concentration in the plasma after intravenous injection.

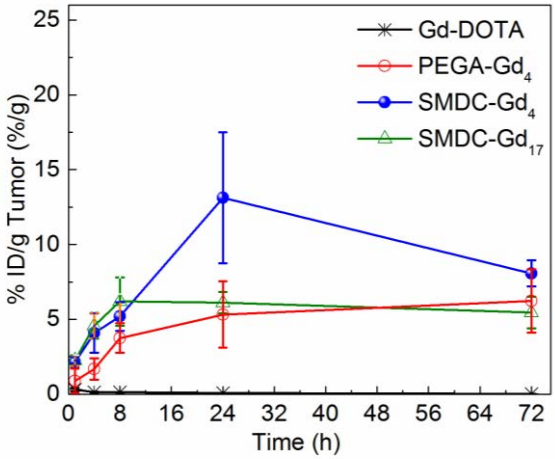


**Figure 4.4**. Time profiles of Gd concentration in the tumor after intravenous injection.

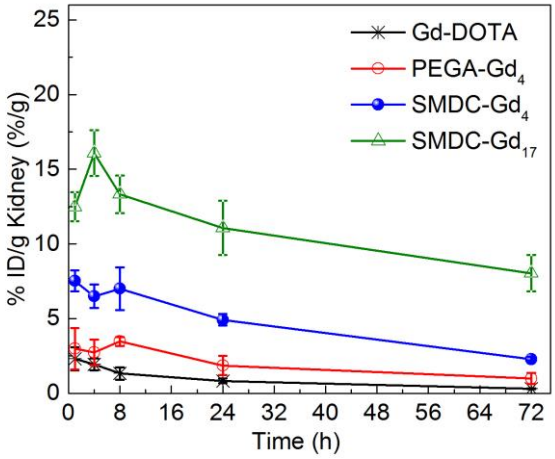


**Figure 4.5**. Time profiles of Gd concentration in the kidney after intravenous injection.

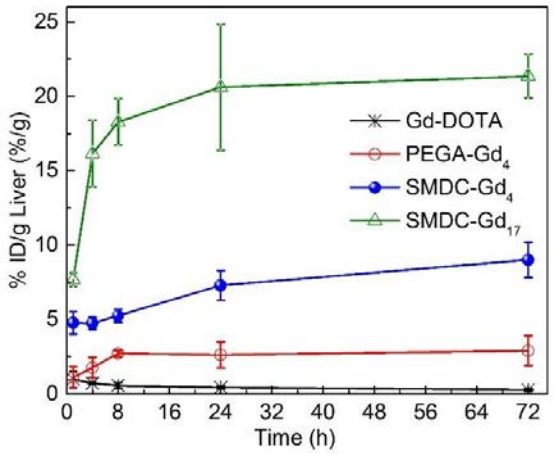


**Figure 4.6**. Time profiles of Gd concentration in the liver after intravenous injection.

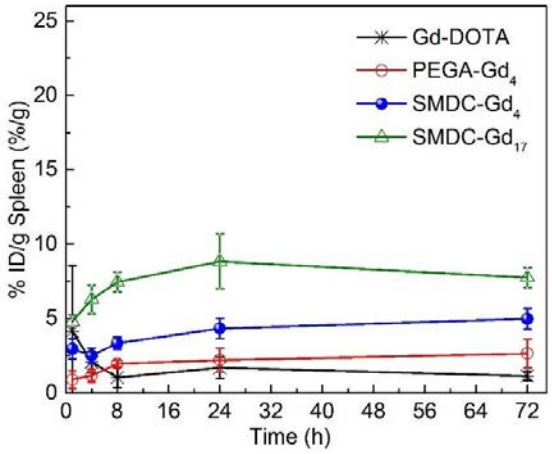


**Figure 4.7**. Time profiles of Gd concentration in the spleen after intravenous injection.

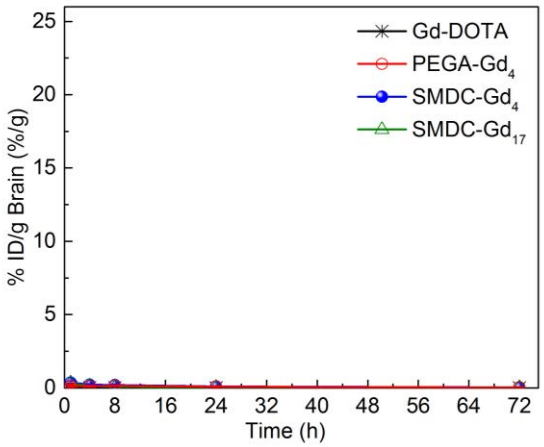


**Figure 4.8**. Time profiles of Gd concentration in the brain after intravenous injection.

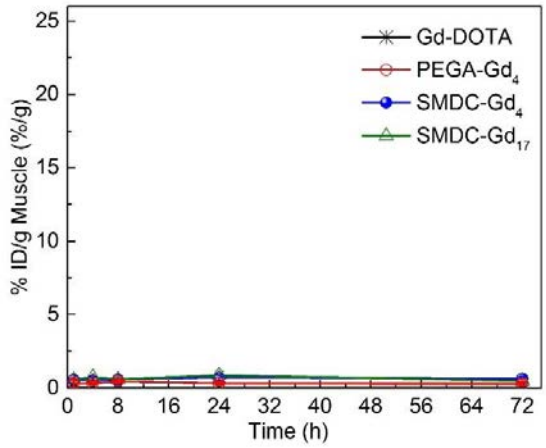


**Figure 4.9**. Time profiles of Gd concentration in the muscle after intravenous injection.

The area under the biodistribution curve (AUC) for the tumor, blood, and major organs was computed based on the biodistribution results. Ratios of the AUC for the tumor to AUC for organs within 72 hours post-injection were determined to elucidate the selective accumulation in tumors. As shown in **Figures 4.10-4.13**, results revealed that SMDC-$Gd_4$ exhibited a progressive and selective accumulation in tumors over time. The quick blood clearance of SMDC-Gds also contributed to the elevation of tumor/major organs (liver, spleen, and kidney) ratios, which are critical criteria for minimizing background signals in MRI. Notably, for SMDC-$Gd_{17}$, AUC ratios of the tumor to organs consistently remained below 1, indicating poor selectivity for tumors. The remarkably high AUC ratio of tumor/blood was attributed to the exceedingly low concentration of SMDC-$Gd_{17}$, approaching zero according to plasma clearance profiles. Consequently, SMDC-$Gd_4$ was selected for cancer imaging and therapy owing to its exceptional biodistribution performance. The 24-hour post-injection should be the optimal time point for imaging or irradiation to achieve the highest tumor-targeting accumulation.

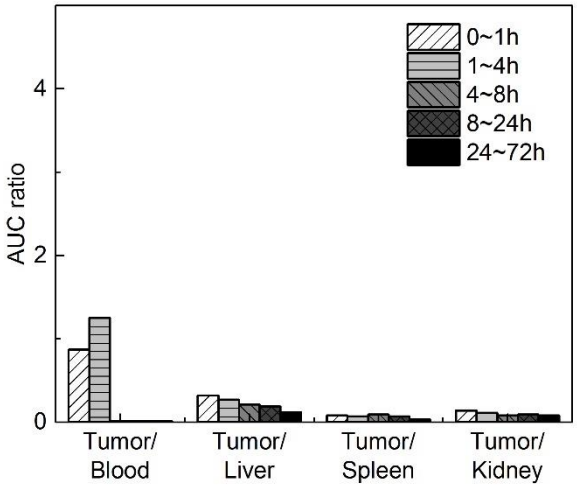


**Figure 4.10**. AUC ratios of the tumor to the main organs after the intravenous administration of Gd-DOTA.

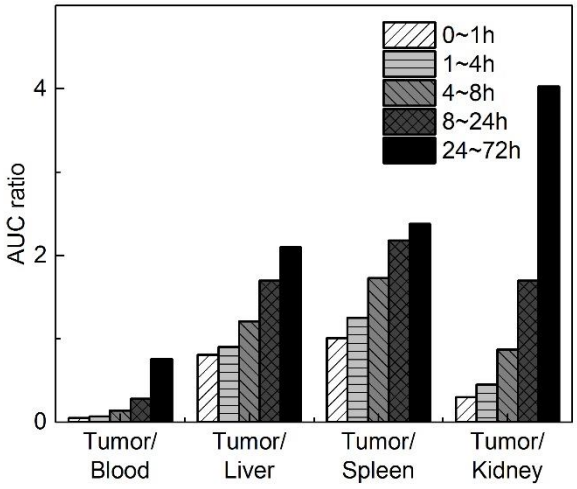


**Figure 4.11**. AUC ratios of the tumor to the main organs after the intravenous administration of PEGA-$Gd_4$.

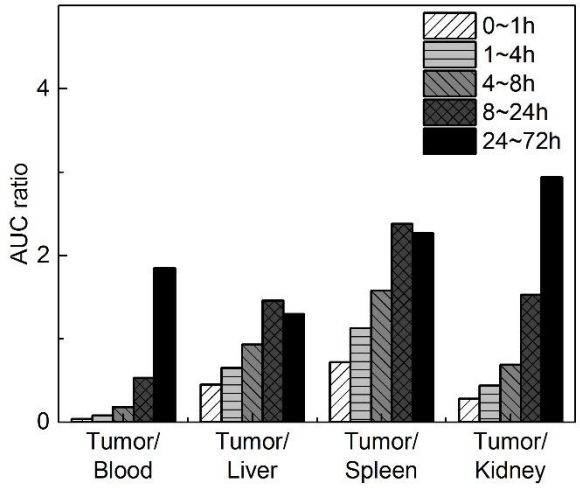


**Figure 4.12**. AUC ratios of the tumor to the main organs after the intravenous administration of SMDC-$Gd_4$.

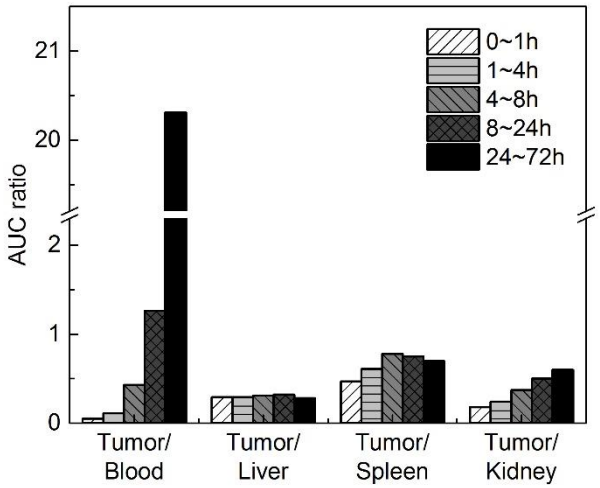


**Figure 4.13**. AUC ratios of the tumor to the main organs after the intravenous administration of SMDC-$Gd_{17}$.

### 4.4.2 Blood parameter assay

A single dose biotoxicity assay was conducted at a dose of 0.1 mmol Gd/kg through intravenous administration, assessing various blood indicators, including WBC, RBC,

HGB, HCT, and PLT, and various plasma indicators, including BUN, CRE, GPT, GOT, ALP, and TP. Given the indication that both SMDC-$Gd_4$ and PEGA-$Gd_4$ accumulated in the liver and kidney, with high concentrations in the blood during excretion, these indicators were examined to characterize the conditions of the liver, kidney, and blood as illustrated in **Figures 4.14-4.24**. Upon detailed analysis, when compared with the indicators in the PBS and Gd-DOTA groups, the insignificantly different BUN, GPT, GOT, ALP, and TP indicators suggested the non-toxicity of SMDC-$Gd_4$ and PEGA-$Gd_4$ to the liver. Similarly, BUN, CRE, and TP indicators demonstrated the non-toxicity to the kidney. Meanwhile, HGB, PLT, RBC, WBC, and HCT indicators showed the non-toxicity to blood. Therefore, this blood parameters analysis with a clinically available dosage (0.1 mmol/kg on Gd basis) revealed no acute influences on both cellular and hematological levels and could be utilized in MRI and Gd-NCT experiments.

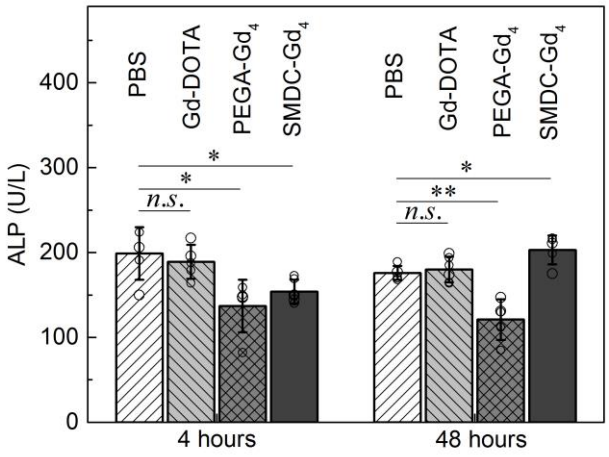


**Figure 4.14**. Effects of Gd-conjugated contrast agents on the alkaline phosphatase level in mice. *n.s.* $p \geq 0.05$, * $p < 0.05$, ** $p < 0.01$.

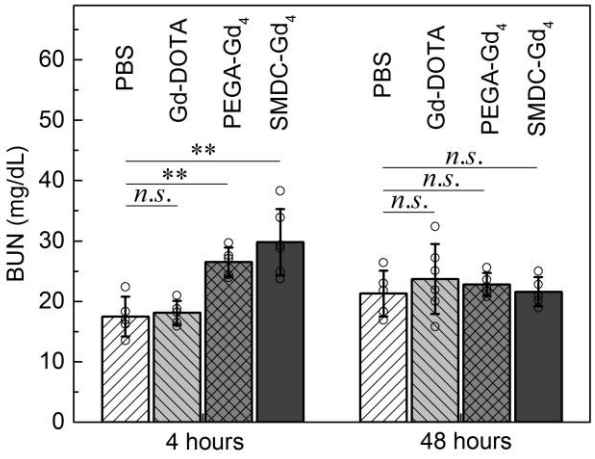


**Figure 4.15**. Effects of Gd-conjugated contrast agents on the blood urea nitrogen in mice. *n.s.* $p \geq 0.05$, ** $p < 0.01$.

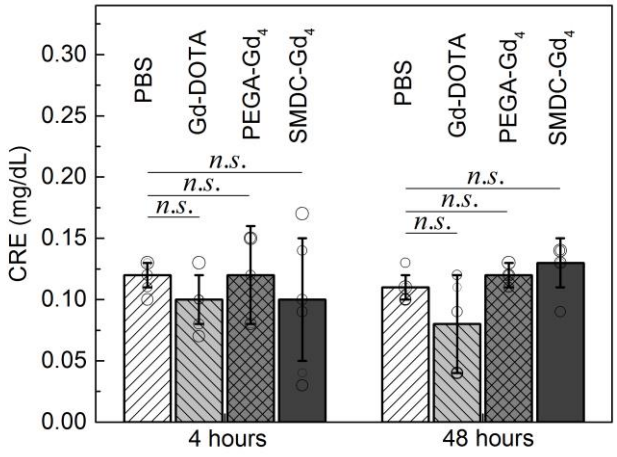


**Figure 4.16**. Effects of Gd-conjugated contrast agents on the creatinine level in mice. *n.s.* $p \geq 0.05$.

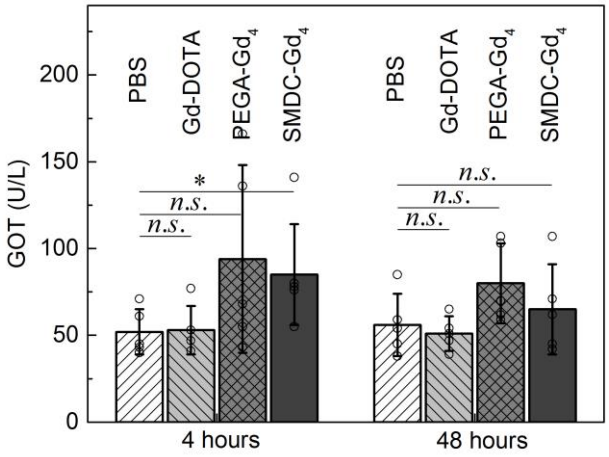


**Figure 4.17**. Effects of Gd-conjugated contrast agents on the glutamic-oxaloacetic transaminase level in mice. *n.s.* $p \geq 0.05$, * $p < 0.05$.

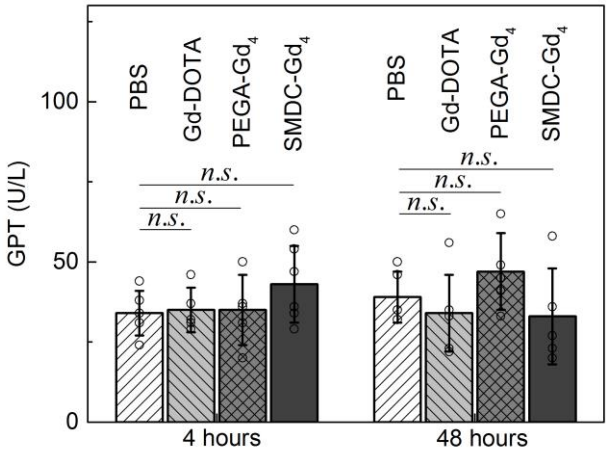


**Figure 4.18**. Effects of Gd-conjugated contrast agents on the glutamic-pyruvic transaminase level in mice. *n.s.* $p \geq 0.05$.

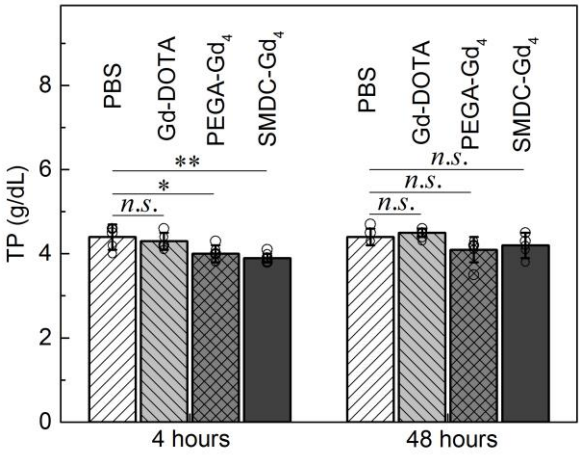


**Figure 4.19**. Effects of Gd-conjugated contrast agents on the total protein level in mice. *n.s.* $p \geq 0.05$, * $p < 0.05$, ** $p < 0.01$.

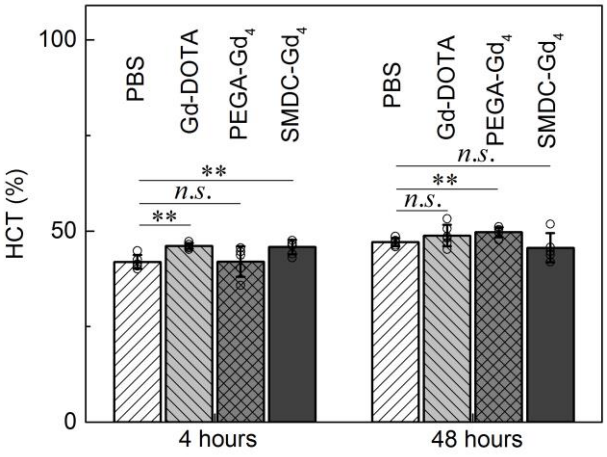


**Figure 4.20**. Effects of Gd-conjugated contrast agents on the hematocrit level in mice. *n.s.* $p \geq 0.05$, ** $p < 0.01$.

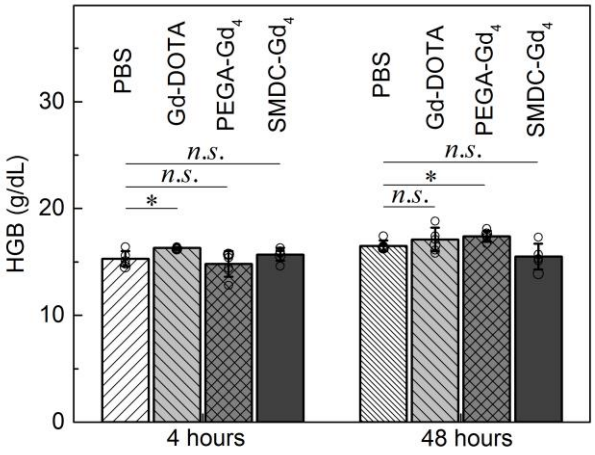


**Figure 4.21**. Effects of Gd-conjugated contrast agents on the hemoglobin level in mice. *n.s.* $p \geq 0.05$, * $p < 0.05$.

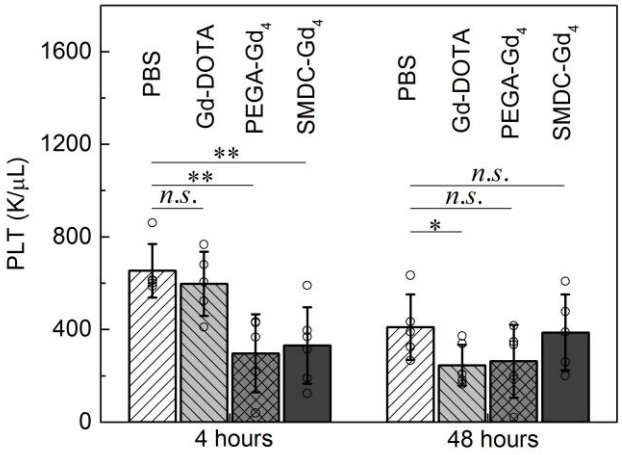


**Figure 4.22**. Effects of Gd-conjugated contrast agents on the platelet count in mice. *n.s.* $p \geq 0.05$, * $p < 0.05$, ** $p < 0.01$.

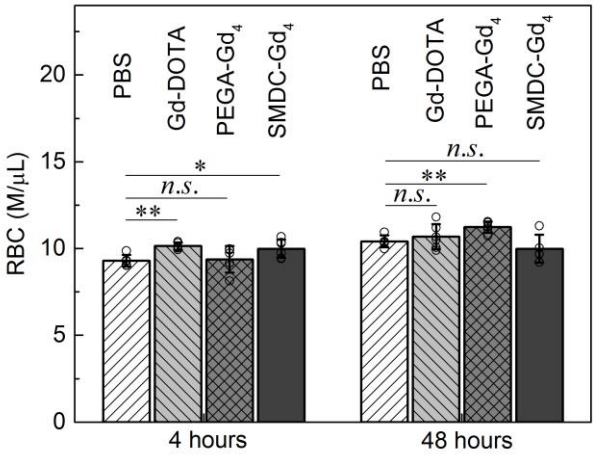


**Figure 4.23**. Effects of Gd-conjugated contrast agents on the red blood cell count in mice. *n.s.* $p \geq 0.05$, * $p < 0.05$, ** $p < 0.01$.

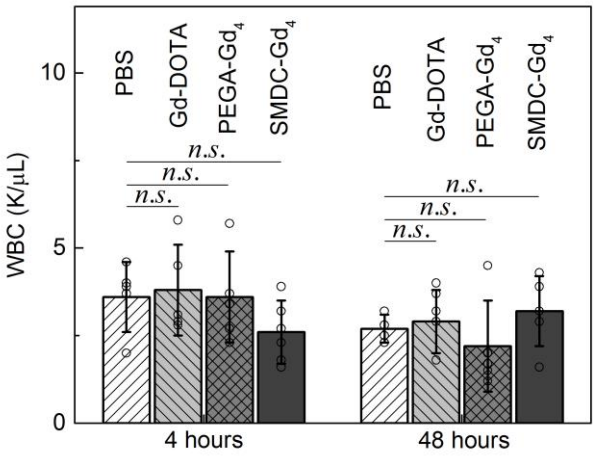


**Figure 4.24**. Effects of Gd-conjugated contrast agents on the white blood cell count in mice. *n.s.* $p \geq 0.05$.

## 4.5 Summary

In this chapter, the *in vitro* and *in vivo* performances of Gd-loaded agents, SMDC-

Gds, were investigated and compared. The cell viability assay indicated the non-cytotoxicity of SMDC-Gds and the Gd-leakage assay showed the stability and safety of SMDC-Gds. According to biodistribution results, SMDC-$Gd_4$ demonstrated superior performance over SMDC-$Gd_{17}$, showcasing high tumor targeting accumulation (13.1±4.4%ID/g at 24 h post-injection), relatively low accumulation in organs, and rapid blood clearance. Consequently, SMDC-$Gd_4$ was selected as the agent for cancer imaging and therapy in this research, the imaging and irradiation time points were determined to be 24 hours post-administration. The safety of dose at 0.1 mmol/kg on a Gd basis was confirmed by evaluating the blood and plasma indicators of mice intravenously injected by SMDC-$Gd_4$, thus it was determined to be the administration dose in MRI and Gd-NCT.

## 4.6 References

[1] Yang Z, Lin H, Huang J, Li A, Sun C, Richmond J, Gao J. A gadolinium-complex-based theranostic prodrug for *in vivo* tumour-targeted magnetic resonance imaging and therapy. Chemical Communications, **2019**, 55(31): 4546-4549.

[2] Le Fur M, Caravan P. The biological fate of gadolinium-based MRI contrast agents: a call to action for bioinorganic chemists. Metallomics, **2019**, 11(2): 240-254.

[3] Rogosnitzky M, Branch S. Gadolinium-based contrast agent toxicity: a review of known and proposed mechanisms. Biometals, **2016**, 29(3): 365-376.

[4] Ramalho J, Semelka RC, Ramalho M, Nunes RH, AlObaidy M, Castillo M. Gadolinium-based contrast agent accumulation and toxicity: an update. American Journal of Neuroradiology, **2016**, 37(7): 1192-1198.

[5] Bower DV, Richter JK, von Tengg-Kobligk H, Heverhagen JT, Runge VM. Gadolinium-based MRI contrast agents induce mitochondrial toxicity and cell death in human neurons, and toxicity increases with reduced kinetic stability of the agent. Investigative radiology, **2019**, 54(8): 453-463.

[6] Li H, Meade TJ. Molecular magnetic resonance imaging with Gd (III)-based contrast agents: challenges and key advances. Journal of the American Chemical Society, **2019**,

141(43): 17025-17041.

[7] Pellico J, Ellis CM, Davis JJ. Nanoparticle-based paramagnetic contrast agents for magnetic resonance imaging. Contrast Media & Molecular Imaging, **2019**, 2019: 1845637.

[8] Uchino H, Matsumura Y, Negishi T, Koizumi F, Hayashi T, Honda T, Nishiyama N, Kataoka K, Naito S, Kakizoe T. Cisplatin-incorporating polymeric micelles (NC-6004) can reduce nephrotoxicity and neurotoxicity of cisplatin in rats. British Journal of Cancer, **2005**, 93: 678-687.

[9] Hamaguchi T, Matsumura Y, Suzuki M, Shimizu K, Goda R, Nakamura I, Nakatomi I, Yokoyama M, Kataoka K, Kakizoe T. NK105, a paclitaxel-incorporating micellar nanoparticle formulation, can extend in vivo antitumour activity and reduce the neurotoxicity of paclitaxel. British Journal of Cancer, **2005**, 92: 1240-1246.

[10] Takahashi A, Yamamoto Y, Yasunaga M, Koga Y, Kuroda J, Takigahira M, Harada M, Saito H, Hayashi T, Kato Y, Kinoshita T, Ohkohchi N, Hyodo I, Matsumura Y. NC-6300, an epirubicin-incorporating micelle, extends the antitumor effect and reduces the cardiotoxicity of epirubicin. Cancer Science, **2013**, 104: 920-925.

# Chapter 5. Performance of SMDC-Gd in MRI for cancer

## 5.1 Introduction

MRI is a widely employed medical imaging technique based on the principle of nuclear magnetic resonance [1]. This method determines the type and location of the substance by detecting the different relaxation times ($T_1$ and $T_2$) of protons under the magnetic field and radio frequency pulse, ultimately producing images of the internal structure of the object [2]. Contrast agents (CAs) are frequently utilized to improve the visibility of internal body structure during MRI [3]. Gadolinium chelates, as commonly used in $T_1$-weighted MRI contrast agents, reduce the $T_1$ value of surrounding $H_2O$ molecules, thereby enhancing their visibility in images [4-5]. In the realm of MRI cancer diagnosis, recent findings suggest that targeting Gd to tumors via Gd-loaded DDS can effectively improve tumor visibility while reducing biotoxicity [6-7]. Therefore, the development of Gd-loaded DDS with enhanced tumor-targeting properties has become a prominent focus in MRI cancer diagnosis.

Given that SMDC-$Gd_4$ was specifically designed and confirmed as a Gd-based contrast agent for tumor-targeting MRI, this chapter investigated the feasibility of utilizing SMDC-$Gd_4$ in MRI for tumor diagnosis. The relaxivity ($r_1$ and $r_2$) of SMDC-$Gd_4$ and control groups (PEGA-$Gd_4$ and Gd-DOTA) were measured and discussed to assess the availability for $T_1$-weighted MRI. Subsequently, $T_1$-weighted MRI scans were conducted according to the schedule established in the preceding chapter. $R_1$ maps of tumor cross-section were observed at various time points, including pre-injection, 1 h, and 24 h post-injection to investigate the tumor-targeting contrast enhancement effect.

Moreover, $R_1$ maps of kidney and bladder cross-sections were observed within the first hour after injection to explore renal excretion properties. The contrast enhancement effect in tumor tissues with lower administration doses was studied to explore dose-dependence and the potential for controlling the enhancement effect by adjusting the dosage.

## 5.2 Materials and methods

### 5.2.1 Relaxivity characterization

The longitudinal and transverse relaxation time $T_1$ and $T_2$ values were measured by Bruker minispec mq20 (0.47 T) and mq60 (1.5 T) (Bruker Corporation, Billerica, Massachusetts, USA). Each sample with four concentrations (1, 0.5, 0.25, and 0.125 mM) with or without BSA (10 mg/mL) was prepared prior to the measurement. Parameters of the NMR system were as follows; temperature = 37 °C, receiver gain = 80-82, recycle delay = 2. The least squares method was used for linear fitting of the $r_1$, $r_2$, and $r_1/r_2$ values.

### 5.2.2 MRI of CT26 tumor-bearing mice

All *in vivo* MRI experiments were approved by the Animal Experiment Committee of the National Institutes for Quantum Science and Technology (14-1006-14). BALB/c nu/nu mice (5 weeks old, female, Japan SLC Inc., Hamamatsu, Japan) were inoculated subcutaneously with CT26 ($1 \times 10^6$ cells/mouse) cells in Hanks′ balanced salt solution (Sigma-Aldrich, Japan). One-week post-inoculation, the mice were randomly separated into three groups (n = 4), intravenously injected with Gd-DOTA, PEGA-$Gd_4$, and SMDC-$Gd_4$ (0.1 mmol/kg on Gd basis) *via* the tail vein (doses of PEGA-$Gd_4$ and SMDC-$Gd_4$ in dose-dependence investigation were 0.1, 0.05, 0.03, and 0.01 mmol Gd/kg, n = 2-4). Each mouse was anesthetized with isoflurane (3% for initial induction and 1%-2% during MRI scan) and placed in a prone position on a custom-made MRI bed with a bite bar and gas mask. The respiration rate was monitored using a respiration sensor (SA Instruments, Inc., NY, USA) and regulated at 80-120 breaths per min. The core body temperature was monitored using a rectal probe (FOT-L and FTI-10, FISO Technologies Inc., Germany) and regulated at 37.0° ± 1.0° using a water circulation pad and warm circulating air system.

MRI data were acquired using a horizontal 1.0 T Bruker ICON MRI system (Bruker biospin, Bruker Corporation, Ettlingen, Germany) with a dedicated solenoid coil for the mouse body. Following standard adjustment procedures, a pilot scan was used to accurately locate the animal's body within the magnet. Subcutaneous CT26 tumor-bearing BALB/c nude mice were scanned before and after the intravenous injection of samples. After 24 h of injection, the mice were scanned once again. For quantitative $T_1$ mapping, a rapid acquisition with relaxation enhancement (RARE)-based inversion recovery sequence was used, and the following parameters were adopted: RARE factor, 4; repetition time, 10000 ms; effective echo time, 10 ms; inversion time, 100, 300, 500, 700, 900, 1300, 1700, 1900, 2100, 2500, 2900, 3300, and 3700 ms; number of excitations, 1; slice thickness, 2 mm; field of view (FOV), 28 × 16 $mm^2$; matrix size, 70 × 40; in-plane resolution, 0.4 × 0.4 $mm^2$. The fat suppression mode was off, and FOV saturation was on. Total scanning time for a single timepoint for $T_1$ mapping was 20 min. For $T_1$-weighted imaging, a spin-echo sequence was used, and the following parameters were adopted: repetition time, 400 ms; effective echo time, 7 ms; number of excitations, 4; number of slices, 20; slice thickness, 1 mm; slice gap, 1 mm; FOV, 30 × 30 $mm^2$; matrix size, 150 × 150; in-plane resolution, 0.2 × 0.2 $mm^2$. The fat suppression mode was off, and FOV saturation was off. Total scanning time for a single timepoint for $T_1$-weighted imaging was 4 min. $T_1$ maps and $T_1$-weighted images were reconstructed and analyzed using a ParaVision (Bruker) and MATLAB software (Mathworks, Natiek, MA).

## 5.3 Relaxivity of SMDC-Gd

This investigation focused on the correlation between relaxivity and SMDC formation. Generally, incorporating CAs, such as Gd complexes, to the surface of nanosized particles/micelles can maintain positive signal enhancement in $T_1$-weighted imaging, although the increase in longitudinal relaxivity ($r_1$) is limited. On the other hand, binding Gd complexes to the interior of nanosized particles/micelles induces relaxivity, however, this compromises the ability to achieve positive signal enhancement on MRI

images due to hydrophobicity and increased transverse relaxivity ($r_2$). For SMDC-Gds and PEGA-Gds, the observed relaxation parameters, including $r_1$, $r_2$, and relaxometric ratio, $r_1/r_2$, at two different magnetic fields were summarized in **Table 5.1** and **5.2**. Compared to the clinically approved Gd-DOTA, SMDC-Gds and PEGA-Gds exhibited higher $r_1$ and $r_2$ values due to slowed down rotation resulting from conjugation of polymer and CAs, leading to increased molecular weight [8-9]. Additionally, SMDC-Gds showed higher $r_1$ and $r_2$ values compared to PEGA-Gds.

Recent studies have indicated that tethering of Gd complexes onto the polymer increases the relaxivities due to slow tumbling effect [10-11], however, the effect of an increasing amount of Gd is negligible due to fast segmental or internal motion [8-9]. Here, notably, the self-folding process of SMDC-Gds created a crowded complex environment, facilitating the rise in relaxivities because of possible restrictions of internal/segmental motion around the interface of SMDC-Gds (**Figure 5.1**). Little effect was attributed to the increasing number of Gd-DOTA molecules within the same formulation, suggesting that SMDC-Gd could potentially induce high relaxivities with a minimal Gd payload. To utilize SMDC-Gd as systemically injectable CAs, the anti-fouling property and the maintenance of positive effects (high $r_1/r_2$) in the bloodstream are crucial. Tests with BSA (10 mg/mL) showed imperceptible effects on $r_1$, $r_2$, and $r_1/r_2$ of SMDC-Gds and PEGA-Gds, illustrating minimal protein interactions due to PEG shielding.

Moreover, the influence of the magnetic field on relaxation parameters was confirmed. Generally, $r_1$ of Gd-chelates peaks around 0.5 T and decreases at higher field strengths [1]. At 1.5 T, SMDC-Gds exhibited slight decreases in $r_1$ values, as expected. While $r_2$ typically increases at higher magnetic fields, and this tendency might be enhanced in case of nanoparticle applications. However, $r_2$ of SMDC-Gds showed almost no change at 1.5 T, suggesting the suppression of $r_2$ elevation with the molecular structure of SMDC-Gds. Therefore, the results supported the performance of SMDC-Gd as a positive macromolecule contrast agent.

**Table 5.1**. Relaxivities and relaxometric ratios of Gd-conjugated contrast agents in water and bovine serum albumin (BSA) aqueous solution at 0.47 T magnetic field.

| | $r_1$[a)] [$s^{-1}mM^{-1}$] | $r_2$[b)] [$s^{-1}mM^{-1}$] | $r_1/r_2$[c)] | $r_1$ with BSA[d)] [$s^{-1}mM^{-1}$] | $r_2$ with BSA[e)] [$s^{-1}mM^{-1}$] | $r_1/r_2$ with BSA[f)] |
|---|---|---|---|---|---|---|
| Gd-DOTA[12] | 3.4 | 4.1 | 0.83 | -- | -- | -- |
| PEGA-$Gd_4$ | 19.6 ± 0.1 | 23.6 ± 0.1 | 0.83 | 21.4 ± 0.1 | 25.9 ± 0.1 | 0.83 |
| PEGA-$Gd_{12}$ | 20.4 ± 0.1 | 23.0 ± 0.1 | 0.89 | -- | -- | -- |
| SMDC-$Gd_4$ (**TP4**) | 25.9 ± 0.1 | 31.1 ± 0.1 | 0.83 | 26.6 ± 0.1 | 32.1 ± 0.1 | 0.83 |
| SMDC-$Gd_9$ (**TP5**) | 22.8 ± 0.1 | 28.0 ± 0.1 | 0.81 | -- | -- | -- |
| SMDC-$Gd_{17}$ (**TP6**) | 24.7 ± 0.1 | 29.6 ± 0.1 | 0.83 | 25.5 ± 0.1 | 30.8 ± 0.1 | 0.83 |

[a)] Longitudinal relaxivity in water at 37 °C; [b)] Transverse relaxivity in water at 37 °C; [c)] Relaxometric ratio in water at 37 °C; [d)] Longitudinal relaxivity in 10 mg/mL BSA aqueous solution at 37 °C; [e)] Transverse relaxivity in 10 mg/mL BSA aqueous solution at 37 °C; [f)] Relaxometric ratio in 10 mg/mL BSA aqueous solution at 37 °C.

**Table 5.2**. Relaxivities and relaxometric ratios of Gd-conjugated contrast agents in water and bovine serum albumin (BSA) aqueous solution at 1.5 T magnetic field.

| | $r_1$[a)] [$s^{-1}mM^{-1}$] | $r_2$[b)] [$s^{-1}mM^{-1}$] | $r_1/r_2$[c)] | $r_1$ with BSA[d)] [$s^{-1}mM^{-1}$] | $r_2$ with BSA[e)] [$s^{-1}mM^{-1}$] | $r_1/r_2$ with BSA[f)] |
|---|---|---|---|---|---|---|
| Gd-DOTA[12] | 2.9 | 3.2 | 0.91 | -- | -- | -- |
| PEGA-$Gd_4$ | 15.1 ± 0.1 | 20.4 ± 0.1 | 0.74 | 15.0 ± 0.1 | 20.9 ± 0.1 | 0.72 |
| PEGA-$Gd_{12}$ | 14.7 ± 0.1 | 19.9 ± 0.1 | 0.74 | -- | -- | -- |
| SMDC-$Gd_4$ (**TP4**) | 17.8 ± 0.1 | 30.3 ± 0.1 | 0.59 | 18.3 ± 0.1 | 31.8 ± 0.1 | 0.58 |
| SMDC-$Gd_9$ (**TP5**) | 17.8 ± 0.1 | 29.9 ± 0.1 | 0.60 | -- | -- | -- |
| SMDC-$Gd_{17}$ (**TP6**) | 18.3 ± 0.1 | 31.5 ± 0.1 | 0.58 | 18.3 ± 0.1 | 32.6 ± 0.1 | 0.56 |

[a] Longitudinal relaxivity in water at 37 °C; [b] Transverse relaxivity in water at 37 °C; [c] Relaxometric ratio in water at 37 °C; [d] Longitudinal relaxivity in 10 mg/mL BSA aqueous solution at 37 °C; [e] Transverse relaxivity in 10 mg/mL BSA aqueous solution at 37 °C; [f] Relaxometric ratio in 10 mg/mL BSA aqueous solution at 37 °C.

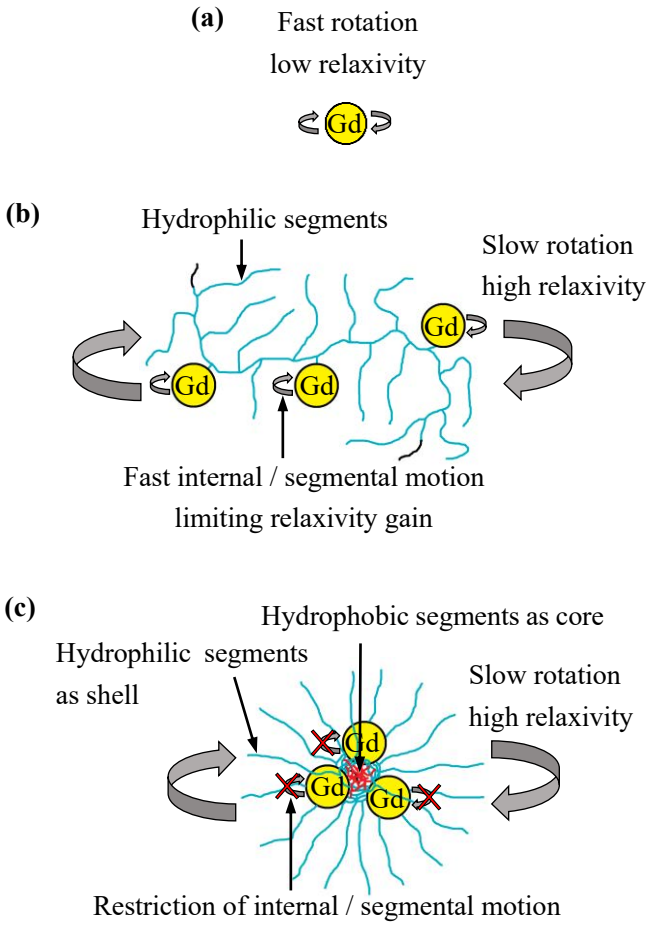


**Figure 5.1**. Strategies for increasing the relaxivity. (a) Small molecular Gd complexes performed fast rotation and thus had relatively low relaxivity. (b) Polymer conjugated Gd complexes exhibited slow rotation, but the relaxivity gain was limited by fast internal or segmental motion. (c) SMDC conjugated Gd complexes produced a crowded complex environment which enabled slow rotation while restricting internal or segmental motion, thus achieved higher relaxivities.

## 5.4 Contrast enhancement for solid tumor in MRI

To assess the viability of the designed contrast agent SMDC-$Gd_4$, a $T_1$-weighted MRI experiment was carried out, with Gd-DOTA and PEGA-$Gd_4$ serving as control groups, each administered with the same Gd dose of 0.1 mmol/kg. The $R_1$ distribution maps from $T_1$-weighted MRI were presented in **Figure 5.2**. The high-intensity signal in the center of the body cross-section, indicated by red coloration, corresponds to fatty tissues. In clinical applications, fat signal interference can be attenuated or removed by fat suppression techniques. However, since this research focused solely on exploring the feasibility of SMDC-$Gd_4$ in MRI, the fat signal was not processed.

Building on the unique characteristics and potentials of SMDC-Gds, $T_1$-weighted MR images against CT26 tumor-bearing mice were evaluated. Vertical slices on $R_1$ distribution maps highlighted the advantages of SMDC-$Gd_4$ over Gd-DOTA and PEGA-$Gd_4$ concerning time-dependent tumor accumulation and clear imaging. At 1 h post-administration, SMDC-$Gd_4$ exhibited substantial contrast enhancement in tumor tissues, with the $R_1$ value of 1.87 $s^{-1}$ and a tumor-to-muscle $R_1$ ratio (T/M) of 1.17. This contrast enhancement surpassed that of PEGA-$Gd_4$ ($R_1$ = 1.67 $s^{-1}$, T/M = 1.11) and Gd-DOTA ($R_1$ = 0.99 $s^{-1}$, T/M = 0.77). The T/M value of SMDC-$Gd_4$ increased up to 1.36 within 24 hours post-administration, and the tumor $R_1$ value reached 2.39 $s^{-1}$, significantly higher than the value of PEGA-$Gd_4$ ($R_1$ = 2.08 $s^{-1}$). Moreover, PEGA-$Gd_4$ presented clear MR snap shots, suggesting its utility as a polymeric contrast agent. Notably, the absolute amount of Gd in tumors and the T/M ratio do not necessarily coincide when contrasts are presented in the blood. Considering the extended blood circulation properties observed in both SMDC-$Gd_4$ and PEGA-$Gd_4$, the negligible difference in T/M ratio between SMDC-$Gd_4$ and PEGA-$Gd_4$ could likely attributed to signals emanating from muscles and capillaries.

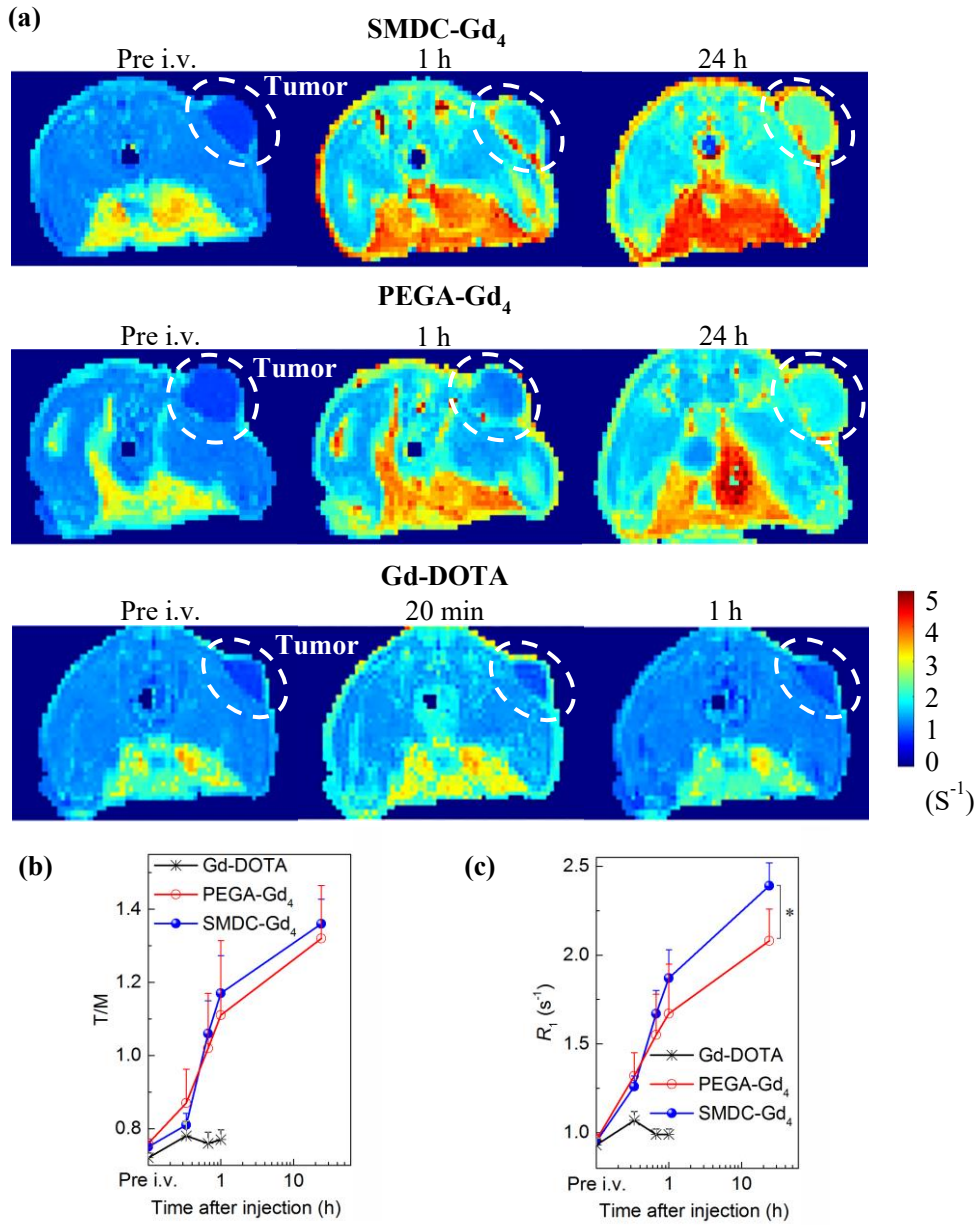


**Figure 5.2**. Contrast enhancement in MRI for cancer diagnostics (a) Quantitative longitudinal relaxation rate ($R_1$, $1/T_1$, $s^{-1}$) maps of CT26 tumor-bearing mice at 1 T MRI, $n = 4$. Compared to results of Gd-DOTA and PEGA-$Gd_4$, the contrast in the tumor (white dashed area) was selectively enhanced by using SMDC-$Gd_4$ at both 1 h and 24 h after intravenous administration. (b-c) Comparison of tumor-to-muscle $R_1$ ratios (T/M) (b) and $R_1$ values in tumor areas (c) showed the enhancement of signals in tumor areas (white dashed area in (a) by SMDC-$Gd_4$. Data are shown as mean ± s.d., $n = 4$, $^*p < 0.05$.

Following the confirmation that SMDC-Gd$_4$, administered at a dose of 0.1 mmol Gd/kg, effectively provide targeted contrast enhancement for tumors, the MRI scans at lower doses, 0.05, 0.03, and 0.01 mmol Gd/kg, was conducted to explore the dose-dependence of both SMDC-Gd$_4$ and PEGA-Gd$_4$. As depicted in **Figure 5.3**, it was evident that contrast enhancement in tumors for both samples gradually diminished with decreasing doses. Notably, the $R_1$ values in the tumor area of the SMDC-Gd$_4$ group consistently exceeded those of the PEGA-GD$_4$ group. This outcome suggested a substantial dose-dependence in the $R_1$ values of both SMDC-Gd$_4$ and PEGA-Gd$_4$, with the values consistently higher for SMDC-Gd$_4$ compared to PEGA-Gd$_4$ within 24 h post-administration.

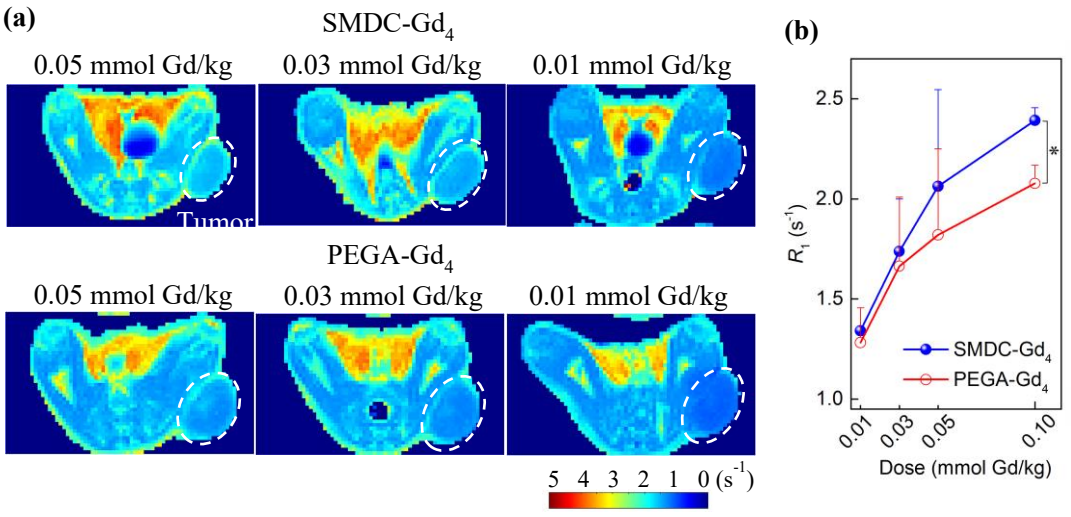


**Figure 5.3**. Contrast effect of SMDC-Gd$_4$ and PEGA-Gd$_4$ in MRI with multiple doses. (a) Longitudinal relaxation ratio ($R_1$) distribution maps of CT26 tumor bearing mice at $T_1$ MRI. (b) $R_1$ in tumor versus the dose curves of SMDC-Gd$_4$ and PEGA-Gd$_4$. Data are shown as mean ± SEM, $n$ = 2-4, $^*p < 0.05$. Comparison of $R_1$ values in tumor areas between SMDC-Gd$_4$ and PEGA-Gd$_4$. Adipose tissue showed the highest $R_1$ in all cases.

## 5.5 Excretion behavior investigated by MRI.

The renal excretion performance of SMDC-$Gd_4$ was evaluated by assessing kidney accumulation in the biodistribution study conducted over 72 hours. However, for a more precise assessment of renal excretion shortly after administration, monitoring MR signals in the kidney and bladder during the first hour post-administration was deemed necessary. As indicated in **Figure 5.4**, The accumulation profile in the kidney and its clearance during the first hour exhibited similar trends to the biodistribution results. The variation in the kidney and bladder clearance times reflected the permeation ability of SMDC-$Gd_4$ and PEGA-$Gd_4$ towards the fenestrated and negatively charged glomerular basement membrane (GBM).

These differences attributed to their distinct properties; specifically, while both SMDC-$Gd_4$ and PEGA-$Gd_4$ exhibited comparable surface charges, SMDC-$Gd_4$ was designed to display a highly dense self-folding structure with a diameter of 5-7 nm, which was within the size threshold of GBM. In contrast, PEGA-$Gd_4$ did not exhibit any SAXS signals, indicating its flexible polymer state. Thus, even within the sub-10 nm range, such chemical and morphological properties in single polymer strands could significantly impact biological behavior in GBM. It is noteworthy that CMC/CAC does not exist in the SMDC system. Many studies on nanosized CAs emphasized their imaging potential, with kidney accumulation being one of the safety parameters, there was also an influence of dissociated fractions occurring from carriers' decomposition. Although further research is needed to clarify the details of GBM-polymer filtration, these results showed the validity of fine-tuning by controlling the balance between flexibility and rigidity of a single polymer design for the rapid excretion of polymer-type CAs. Hence, optimized SMDC systems might be useful for a precise and careful tumor diagnosis even with multiple injections/trials of MRI over time.

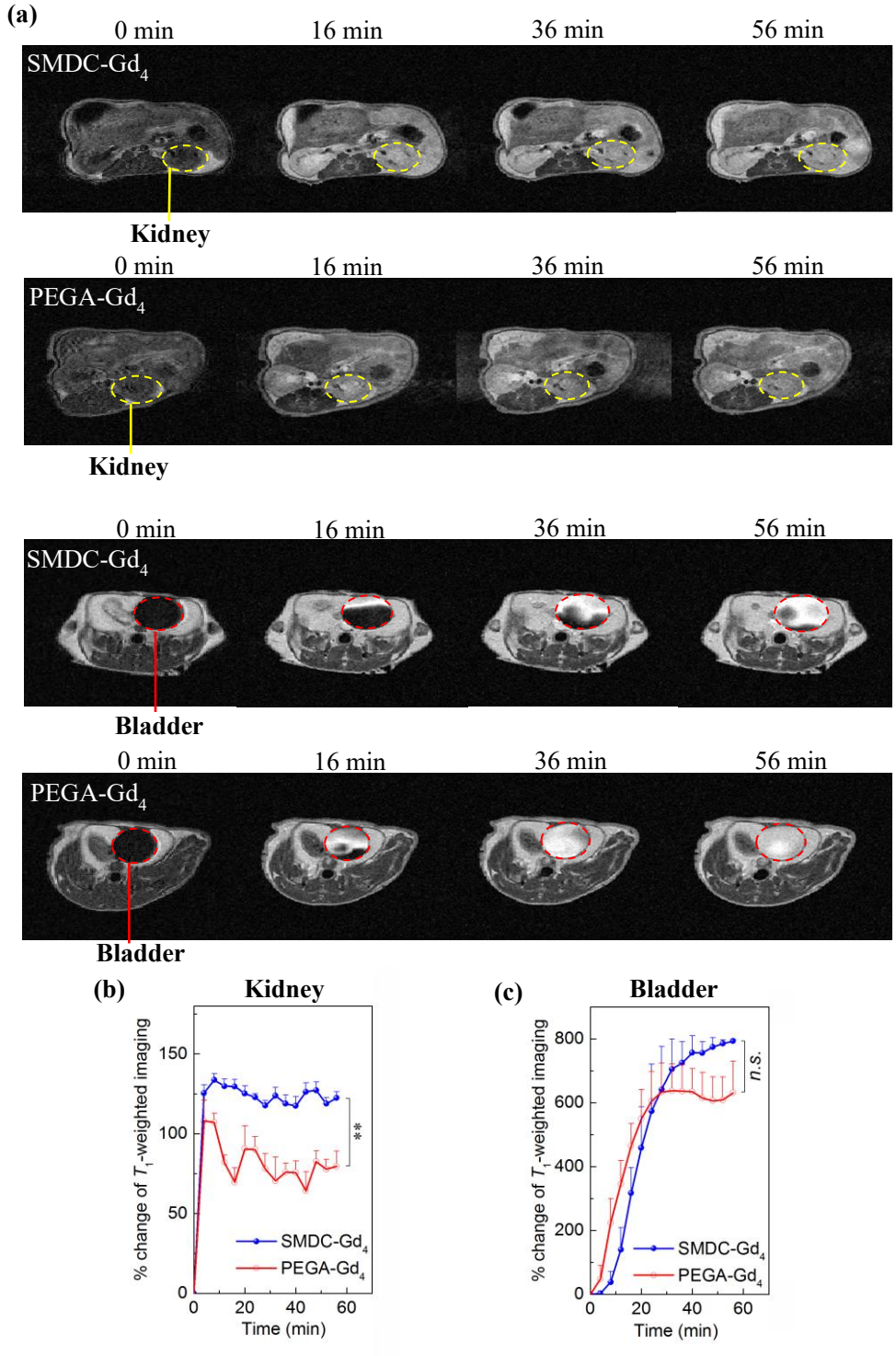


**Figure 5.4**. Renal excretion of SMDC-Gd4 and PEGA-Gd4 measured by $T_1$-weighted MRI against tumor-bearing mice. (a) MRI of kidneys and bladders within 1 h post-administration. (b-c) The comparison of longitudinal signals intensities in kidneys (b) and bladders (c) within 1 h post-administration. Data are shown as mean ± SEM, $n = 3$, $^{**}p < 0.01$, *n.s.* $p \geq 0.05$.

## 5.6 Summary

In this chapter, the potential application of the designed SMDC-$Gd_4$ as a contrast agent for MRI tumor diagnosis was explored. The higher relaxivity values, both $r_1$ and $r_2$, compared to the control groups indicated the suitability of SMDC-$Gd_4$ for $T_1$-weighted MRI. The strong tumor-targeted contrast enhancement effect of SMDC-$Gd_4$ in $R_1$ maps of $T_1$-weighted MRI was directly observed at 24 hours post-injection, affirming the viability of SMDC-$Gd_4$ in MRI. Furthermore, the dose-dependence of this enhancement effect was confirmed. This superior performance of SMDC-$Gd_4$ in $T_1$-weighted MRI, in comparison to control groups, was attributed to its demonstrated selective accumulation in tumors. Meanwhile, the renal excretion properties of both SMDC-$Gd_4$ and PEGA-$Gd_4$ were elucidated by directly observing the $R_1$ map of kidney and bladder cross-sections during the first hour post-administration. The observed differences in renal excretion properties could be a contributing factor to the notable performance of SMDC-$Gd_4$ as a contrast agent in MRI.

## 5.7 References

[1] Terreno E, Castelli DD, Viale A, Aime S. Challenges for molecular magnetic resonance imaging. Chemical reviews, **2010**, 110(5): 3019-3042.

[2] Grover VPB, Tognarelli JM, Crossey MME, Cox IJ, Taylor-Robinson SD, McPhail MJW. Magnetic resonance imaging: principles and techniques: lessons for clinicians. Journal of clinical and experimental hepatology, **2015**, 5(3): 246-255.

[3] Yan GP, Robinson L, Hogg P. Magnetic resonance imaging contrast agents: overview and perspectives. Radiography, **2007**, 13: e5-e19.

[4] Clough TJ, Jiang L, Wong KL, Long NJ. Ligand design strategies to increase stability of gadolinium-based magnetic resonance imaging contrast agents. Nature communications, **2019**, 10(1): 1-14.

[5] Blumfield E, Swenson DW, Iyer RS, Stanescu AL. Gadolinium-based contrast

agents—review of recent literature on magnetic resonance imaging signal intensity changes and tissue deposits, with emphasis on pediatric patients. Pediatric radiology, 2019, 49(4): 448-457.

[6] Hafner S, Raabe M, Wu Y, Wang T, Zuo Z, Rasche V, Syrovets T, Weil T, Simmet T. High-contrast magnetic resonance imaging and efficient delivery of an albumin nanotheranostic in triple-negative breast cancer xenografts. Advanced Therapeutics, **2019**, 2(11): 1900084.

[7] Fu S, Cai Z, Ai H. Stimulus-Responsive Nanoparticle Magnetic Resonance Imaging Contrast Agents: Design Considerations and Applications. Advanced Healthcare Materials, **2021**, 10(5): 2001091.

[8] Zhang Z, Greenfield MT, Spiller M, McMurry TJ, Lauffer RB, Caravan P. Multilocus Binding Increases the Relaxivity of Protein-Bound MRI Contrast Agents. Angewandte Chemie International Edition, **2005**, 44: 6766-6769.

[9] Caravan P, Farrar CT, Frullano L, Uppal R. Influence of molecular parameters and increasing magnetic field strength on relaxivity of gadolinium- and manganese-based T1 contrast agents. Contrast media & molecular imaging, **2009**, 4: 89-100.

[10] Tóth É, Pubanz D, Vauthey S, Helm L, Merbach AE. The role of water exchange in attaining maximum relaxivities for dendrimeric MRI contrast agents. Chemistry-A European Journal, **1996**, 2: 1607-1615.

[11] Botta M, Tei L. Relaxivity Enhancement in Macromolecular and Nanosized GdIII-Based MRI Contrast Agents. European Journal of Inorganic Chemistry, **2012**, 2012: 1945-1960.

[12] Rohrer M, Bauer H, Mintorovitch J, Requardt M, Weinmann H. Comparison of magnetic properties of MRI contrast media solutions at different magnetic field strengths. Investigative radiology, **2005**, 40: 715-724.

# Chapter 6. Performance of SMDC-Gd in Gd-NCT for cancer

## 6.1 Introduction

Neutron capture therapy (NCT) is a form of radiation therapy method including boron neutron capture therapy (BNCT) and gadolinium neutron capture therapy (Gd-NCT) [1]. During NCT, tumor-targeted drugs based on specific elements, namely $^{10}B$ or $^{157}Gd$, are administered, followed by irradiation with epi-/thermal neutrons towards the tumor area. Elements $^{10}B$ and $^{157}Gd$ can capture thermal neutrons and emit high-energy α-rays (from $^{10}B$) or γ-rays and electrons (from $^{157}Gd$), effectively eliminating cancer cells in the tumor tissue where these specific elements accumulate in sufficient concentrations [2]. At present, BNCT has been clinically applied in treating certain tumor types, such as glioblastoma, recurrent cancers of the head/neck region, and melanoma. In contrast, Gd-NCT is still under development and has not yet been applied clinically [3-4].

Compared to the commonly used BNCT, Gd-NCT boasts higher neutron capture efficiency because the $^{157}Gd$ employed in Gd-NCT has a cross section more than 60 times larger than that of $^{10}B$ utilized in BNCT [5]. Moreover, since Gd complexes are commonly employed as contrast agents in MRI examination, Gd-NCT using Gd-complex-based agents can be performed after an MRI examination, serving as a guide for treatment strategy [6-7]. However, the high bio-toxicity of Gd poses a challenge in achieving high intra-tumoral Gd concentrations without the risk of side effects. Addressing this limitation, the focus of development and application lies in the high tumor targeting ability of Gd-complex-based agents.

Given the indicated high tumor targeting ability and the confirmed viability in MRI

through contrast enhancement in tumor tissues, this research employed SMDC-$Gd_4$ in Gd-NCT to investigate the feasibility in cancer therapy. The same dose to that of MRI experiment was administered to observe the growth inhibitory effect and side effect on bodyweight. Subsequently, to increase the Gd concentration in tumor, the injection schedule was adjusted, and the therapeutic effect and side effect of SMDC-$Gd_4$ were assessed based on the tumor growth inhibitory effect and changes in bodyweight.

## 6.2 Materials and methods

### 6.2.1 Biodistribution study for Gd-NCT

BALB/c mice (6 weeks old, female, Japan SLC Inc., Hamamatsu, Japan) bearing CT26 tumors were prepared. The mice were inoculated subcutaneously with CT26 ($1 \times 10^6$ cells/mouse) cells. Ten days post-inoculation, mice were separated into two groups (n = 5), SMDC-$Gd_4$ or Gd-DOTA were injected daily intravenously for three consecutive days *via* the tail vein at the dose of 0.1 mmol/kg based on Gd for each time. The mice were sacrificed at 24 h after the last administration. Blood was collected and centrifuged to obtain the plasma. The tumor, liver and kidney were excised, washed with PBS and weighed. All samples were mixed with a nitric acid solution (concentration = 70%, 1 mL), and acid digestion was conducted using EYELA MG-2300 (Tokyo Rikakikai CO. LTD., Tokyo, Japan). Obtained solutions were diluted by Milli-Q water, and the Gd concentration in each sample was then measured by inductively coupled plasma mass spectrometry (ICP-MS) using an Agilent 7700x ICP-MS (Agilent Technologies Inc., Santa Clara, CA, USA).

### 6.2.2 Gd-NCT of CT26 tumor-bearing mice

Colon tumor-bearing BALB/c mice (4 weeks old, female, Japan SLC Inc., Hamamatsu, Japan) were prepared for Gd-NCT study. The mice were inoculated subcutaneously with CT26 ($2 \times 10^5$ cells/mouse) in the right thigh. The tumors were allowed to grow for about two weeks. For Gd-NCT with one-time injection, the mice were separated into five groups (n = 5). Gd-DOTA, PEGA-$Gd_4$, and SMDC-$Gd_4$ (0.1

mmol/kg on Gd basis) were intravenously injected to the tumor-bearing mice *via* the tail vein; mice in one group were used as a cold control group and cultivated without injection and radiation. Mice treated with PBS were also prepared as another control group. The inoculated mice were placed in acrylic holders, which were put on a 5-mm-thick thermoplastic plate that contained 40 wt % of 6LiF (96% 6Li) to block thermal neutrons and had a circular hole in the center. The thigh with the tumor was stretched over the hole, and tumor regions were irradiated by thermal neutrons (5MW, Kyoto University Research Reactor, fluence: $2.87 \times 10^{12}$ to $3.29 \times 10^{12}$ thermal neutrons/cm$^2$, $5.10 \times 10^{11}$ to $5.86 \times 10^{11}$ epithermal neutrons/cm$^2$) for 10 min at 24 h after injection. For Gd-NCT with three-times injection, the mice were separated into three groups (n = 5); Gd-DOTA, and SMDC-$Gd_4$ (0.1 mmol/kg on Gd basis) were intravenously injected to the tumor-bearing mice *via* the tail vein at 0 h, 24 h, and 48 h. PBS group was also prepared and treated with the same procedure. The mice were put on a plate as described above, and tumor regions were irradiated by thermal neutrons (5MW, Kyoto University Research Reactor, fluence: $3.27 \times 10^{12}$ to $3.80 \times 10^{12}$ thermal neutrons/cm$^2$, $5.81 \times 10^{11}$ to $6.10 \times 10^{11}$ epithermal neutrons/cm$^2$) for 10 min at 72 h after the first injection. Tumor growth suppression effects were evaluated in terms of tumor size ($V$), which was estimated by the following equation:

$$V = a \times b^2/2 \qquad \textbf{(Equation 6.1)}$$

where a and b are the major and minor axes of the tumor, respectively. The statistical significance of different findings between the experimental and control groups was determined by analysis of variance with Tukey's multiple comparison test. A $p$ value < 0.05 was considered statistically significant.

## 6.3 Anti-tumor effect of SMDC-$Gd_4$ in Gd-NCT

### 6.3.1 Biodistribution of SMDC-$Gd_4$ during Gd-NCT

Gd-based CAs have shown to be applicable for $^{157}$Gd- NCT, but their clinical success in tumor therapy remains elusive [7]. One plausible explanation is the absence of a

targeted delivery strategy for $^{157}$Gd to reach specific tumors. The optimal concentration of $^{157}$Gd is crucial for achieving the desired therapeutic efficacy with thermal neutron irradiation, and one suggested $^{157}$Gd-concentration in tumor was regarded as 50-200 ppm [8]. Although high-dosage injections are feasible for Gd-NCT to achieve the desired $^{157}$Gd-concentration, such approaches are prone to side effects and inefficient therapeutic outcomes. This inefficiency is often attributed to an excess fraction of Gd surrounding the tumor site, known as the shielding effect [9-10]. Considering clinically approved Gd complexes, a practical dose for both MRI and Gd-NCT is suggested to be in the range of 0.1-0.3 mmol/kg on a Gd basis. However, due to challenges in tumor targeting, using a single injection of low molecular weight Gd complex for Gd-NCT has seen limited success.

In this regard, SMDC-Gd$_4$ demonstrated controllable biodistribution and clearance in a murine model of solid tumors. This observation prompted further investigation into $^{157}$Gd-NCT using the SMDC system. To assess therapeutic potential, the Gd concentrations in tumors were initially evaluated by comparing the number of injections at a dose of 0.1 mmol/kg on a Gd basis for each injection (**Figures 6.1** and **6.2**). While a single administration of SMDC-Gd$_4$ delivered 41.2 ppm of Gd (6.4 ppm of $^{157}$Gd) into the tumor at 24 h after injection, three administrations (every 24 h) increased the final Gd concentration to 91.2 ppm (14.3 ppm of $^{157}$Gd) 24 h after the last injection. Therefore, the multiple injections method with SMDC-Gd$_4$ is imperative to improve the concentration of Gd at the tumor site.

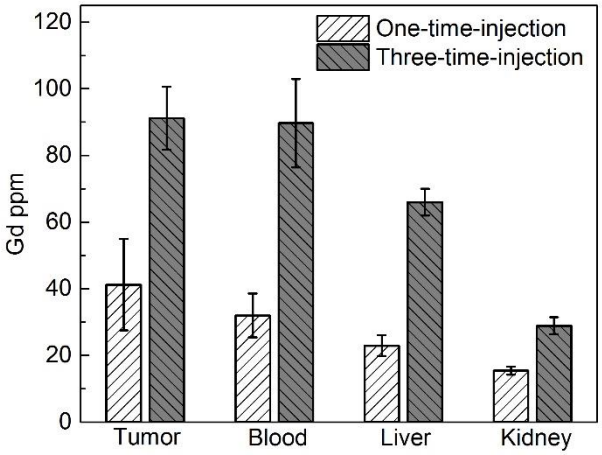


**Figure 6.1**. Gd concentrations in tumors and main organs after 24 h from last intravenous injection of SMDC-$Gd_4$.

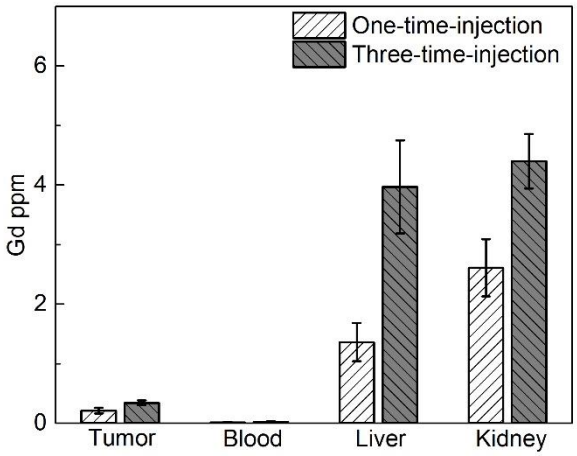


**Figure 6.2**. Gd concentrations in tumors and main organs after 24 h from last intravenous injection of Gd-DOTA.

### 6.3.2 Gd-NCT with one-time-injection against CT26-bearing mice

As illustrated in **Figure 6.3**, When compared to the control group without injection and radiation (Cold group), tumor tissues in mice with radiation exhibited a markedly

growth inhibitory effect, regardless of injected sample. This effect was attributed to the action of water molecules under radiation. However, all Gd-loaded samples did not perform a noticeable growth inhibitory effect on tumors post-radiation when compared to the PBS group. This lack of effect could be attributed to the relatively low intra-tumoral Gd concentration during radiation. Specifically, SMDC-$Gd_4$ achieved only about 41.2 ppm Gd (6.4 ppm $^{157}Gd$) in tumors, as obtained from the biodistribution study. In addition, no side effects causing changes in bodyweight were observed for all samples. To achieve a significant therapeutic effect, it is imperative to increase the Gd concentration in the tumor during irradiation. This could be accomplished by increasing the dose or number of injections.

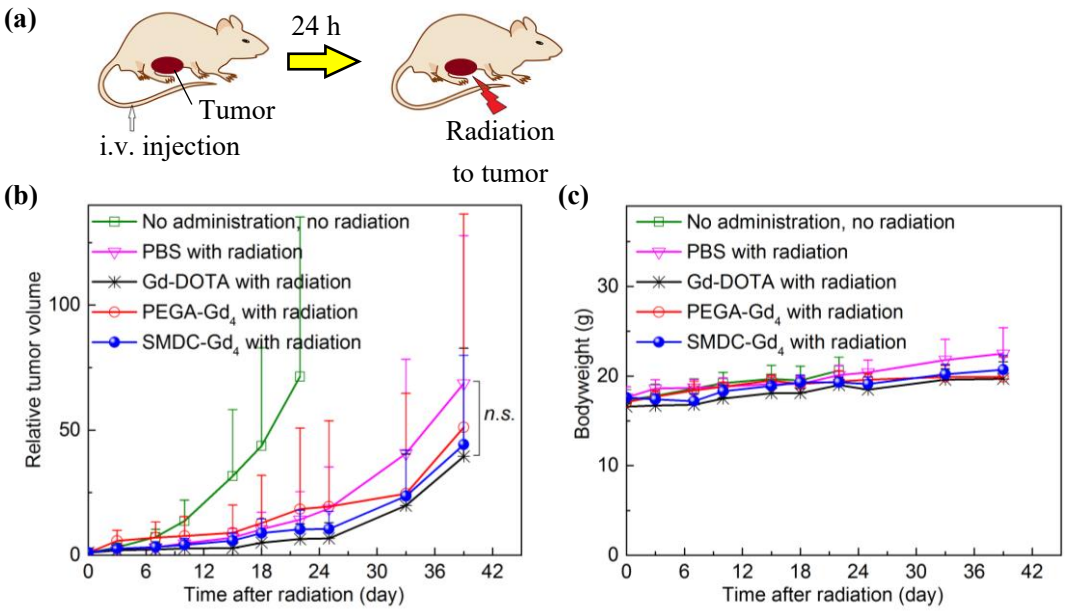


**Figure 6.3**. Anti-tumor effect of SMDC-$Gd_4$ in Gd-NCT against CT26 tumor-bearing mice with one-time-injection. (a) Schematic illustration of the therapeutic regimen for Gd-NCT. (b) Relative tumor volumes in BALB/c mice. Data are shown as mean ± s.d., $n = 5$, *n.s.* $p \geq 0.05$. (c) Bodyweight of mice. Data are shown as mean ± s.d., $n = 5$, *n.s.* $p \geq 0.05$.

### 6.3.3 Gd-NCT with three-time-injection against CT26-bearing mice

With the modification of administration strategy, the potential of Gd-NCT using the SMDC system was explored. SMDC-$Gd_4$ was evaluated against CT26 tumor-bearing mice and compared with Gd-DOTA (**Figure 6.4**). The efficacy of SMDC-$Gd_4$ in Gd-NCT became evident as it effectively suppressed tumor growth without bodyweight loss. In contrast, Gd-DOTA, PBS, and cold-group (no administration and no radiation) failed to demonstrate sufficient anti-tumor activities. This outcome underscored the successful delivery of an appropriate amount of Gd complexes into tumor tissues by SMDC-$Gd_4$, contributing to the anti-tumor effects in Gd-NCT. Although the concentration of $^{157}Gd$ delivered by SMDC in this study was still lower than the recommended range of 50-200 ppm, the fine therapeutic efficacy is noteworthy and warrants careful consideration.

It is crucial to note that the advantage of a drug delivery system using nanocarriers extends beyond the selective accumulation of therapeutic agents; it also involved improvements in the location of agents within tumors. For instance, the size of nanomedicines plays a critical role in their extravasation and penetration in tumors. Small nanomedicines, such as those with a diameter of 30 nm, exhibit superior anti-tumor activity compared to large ones (100 nm) [11]. Given that the diameter of SMDC-Gds is less than 10 nm, our results likely stem from the deep tumor penetration of SMDC, enabling the escape of the shielding effect of thermal neutrons and facilitating efficient diffusion of electrons and γ-rays after irradiation. A similar hypothesis could be adopted to the recently developed AGulX, an inorganic nanosized CA with a sufficiently small size that allows for fine MR imaging and radiotherapy treatment. Consequently, it is reasonable to conclude that the size of SMDC is a distinct advantage for delivering CAs against tumors, leading to refined MR imaging and improved therapeutic outcomes in Gd-NCT. Although further detailed studies are necessary for the development of this new SMDC as drug delivery system, results described in this research demonstrated the feasibility of a fine-tuning drug carrier through self-folding molecular design, making a significant advancement for applications in cancer diagnosis and therapy.

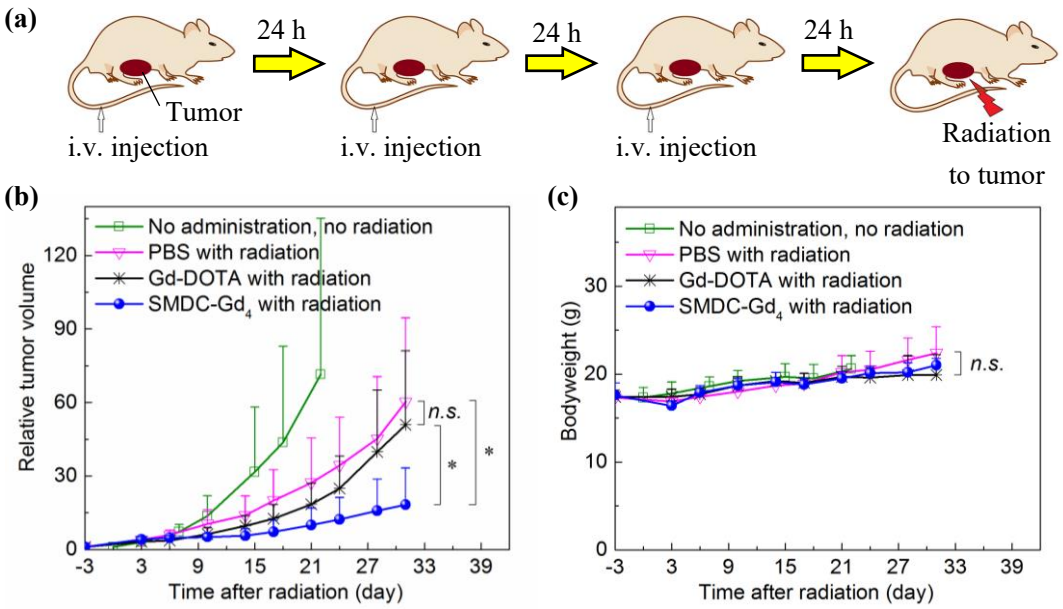


**Figure 6.4**. Anti-tumor effect of SMDC-$Gd_4$ in Gd-NCT against CT26 tumor-bearing mice with three-time-injection. (a) Schematic illustration of the therapeutic regimen for Gd-NCT. Daily injections for 3 consecutive days were given, followed by a thermal neutron irradiation directly towards subcutaneous solid tumors 24 h after the last injection. (b) Relative tumor volumes in BALB/c mice. SMDC-$Gd_4$ combined with radiation showed a significant anti-tumor effect compared with other groups within 31 days after radiation. Data are shown as mean ± s.d., $n = 5$, *n.s.* $p \geq 0.05$, $^{*}p < 0.05$. (c) Bodyweight of mice. Data are shown as mean ± s.d., $n = 5$, *n.s.* $p \geq 0.05$.

## 6.4 Summary

This chapter explored the potential of SMDC-$Gd_4$ for cancer therapy by Gd-NCT method. When administered at the same dosage used in the MRI experiment (0.1 mmol/kg on a Gd basis), SMDC-$Gd_4$ did not exhibit a notable therapeutic effect due to the low Gd concentration (41.2 ppm) in the tumor. To address this, the injection schedule was adjusted, involving three consecutive daily injections of equal doses (0.1 mmol/kg on a Gd basis). This modification resulted in an increased intra-tumoral Gd concentration, reaching 91.2 ppm. At such elevated dosage, SMDC-$Gd_4$ demonstrated a significant

tumor growth inhibitory effect. This result suggested that SMDC-$Gd_4$ could successfully deliver appropriate amount of Gd complexes into tumor tissues and contribute to the anti-tumor effects in Gd-NCT.

## 6.5 References


[1] Dymova MA, Taskaev SY, Richter VA, Kuligina EV. Boron neutron capture therapy: Current status and future perspectives. Cancer communications, **2020**, 40(9): 406-421.

[2] Nedunchezhian K, Aswath N, Thiruppathy M, Thirugnanamurthy S. Boron neutron capture therapy-a literature review. Journal of clinical and diagnostic research: JCDR, **2016**, 10(12): ZE01.

[3] Ho SL, Yue H, Tegafaw T, Ahmad MY, Liu S, Nam S, Chang Y, Lee GH. Gadolinium Neutron Capture Therapy (GdNCT) Agents from Molecular to Nano: Current Status and Perspectives. ACS omega, **2022**, 7(3): 2533-2553.

[4] Narmani A, Farhood B, Haghi-Aminjan H, Mortezazadeh T, Aliasgharzadeh A, Mohseni M, Najafi M, Abbasi H. Gadolinium nanoparticles as diagnostic and therapeutic agents: Their delivery systems in magnetic resonance imaging and neutron capture therapy. Journal of Drug Delivery Science and Technology, **2018**, 44: 457-466.

[5] Enger SA, Giusti V, Fortin MA, Lundqvist H, Rosenschöld PM. Dosimetry for gadolinium neutron capture therapy (GdNCT). Radiation measurements, **2013**, 59: 233-240.

[6] Mi P, Dewi N, Yanagie H, Kokuryo D, Suzuki M, Sakurai Y, Li Y, Aoki I, Ono K, Takahashi H, Cabral H, Nishiyama N, Kataoka K. Hybrid calcium phosphate-polymeric micelles incorporating gadolinium chelates for imaging-guided gadolinium neutron capture tumor therapy. ACS nano, **2015**, 9(6): 5913-5921.

[7] Song G, Cheng L, Chao Y, Yang K, Liu Z. Emerging nanotechnology and advanced materials for cancer radiation therapy. Advanced materials, **2017**, 29(32): 1700996.

[8] Shih JLA, Brugger RM. Gadolinium as a neutron capture therapy agent. Medical physics, **1992**, 19(3): 733-744.

[9] Le UM, Cui Z. Biodistribution and tumor-accumulation of gadolinium (Gd) encapsulated in long-circulating liposomes in tumor-bearing mice for potential neutron capture therapy. International journal of pharmaceutics, **2006**, 320(1-2): 96-103.

[10] Dewi N, Mi P, Yanagie H, Sakurai Y, Morishita Y, Yanagawa M, Nakagawa T, Shinohara A, Matsukawa T, Yokoyama K, Cabral H, Suzuki M, Sakurai Y, Tanaka H, Ono K, Nishiyama N, Kataoka K, Takahashi H. In vivo evaluation of neutron capture therapy effectivity using calcium phosphate-based nanoparticles as Gd-DTPA delivery agent. Journal of cancer research and clinical oncology, **2016**, 142: 767-775.

[11] Cabral H, Matsumoto Y, Mizuno K, Chen Q, Murakami M, Kimura M, Terada Y, Kano MR, Miyazono K, Uesaka M, Nishiyama N, Kataoka K. Accumulation of sub-100 nm polymeric micelles in poorly permeable tumours depends on size. Nature nanotechnology, **2011**, 6(12): 815-823.

# Chapter 7. Conclusion

In this research, a self-folding macromolecular drug carrier (SMDC) with a size of 5-10 nm was proposed as a novel DDS for cancer imaging and therapy. The designed macromolecules, including random copolymers $BZA_m$-$PEGA_n$ and random terpolymers $BZA_m$-$PEGA_n$-$CEA_k$, were synthesized by RAFT polymerization to form the SMDC. The polymerization process was experimentally indicated to be stable and controllable. $BZA_m$-$PEGA_n$ samples were processed in aqueous and organic solutions to investigate the relationship between SMDC formation properties (DA and size) and polymer parameters (BZA/PEGA and DP). Macromolecules for Gd chelate-loaded SMDC (SMDC-Gd) formation were synthesized based on the determined polymer parameters. Consequently, the prepared SMDC-$Gd_4$ exhibited a diameter of 5-7 nm and performed a 13.1%ID/g intra-tumoral accumulation at 24 hours post-injection without apparent biotoxicity.

The selected SMDC-$Gd_4$ was employed in $T_1$-weighted MRI and Gd-NCT for cancer to assess the feasibility and performance of the designed SMDC structure in cancer imaging and therapy. $T_1$-weighted MRI with SMDC-$Gd_4$ revealed a considerable contrast enhancement effect on tumor tissues, displaying strong and uniform contrast enhancement in tumors at 24 hours after administration. In Gd-NCT, a significant tumor growth inhibitory effect was observed at 24 hours after three consecutive daily injections of SMDC-$Gd_4$. These findings demonstrated the feasibility of the developed SMDC-$Gd_4$ in cancer imaging and therapy, furthermore, indicated the outstanding performance and developmental potential of the proposed SMDC structure as a DDS.

The innovative outcomes of this research are highlighted as follows:

(1) A self-folding macromolecular drug carrier (SMDC) structure was proposed and

realized as a DDS for cancer imaging and therapy.

(2) SMDC-Gds were successfully prepared through the synthesis of drug-loaded macromolecules, meeting design specifications with a diameter of 5-7 nm and achieving a tumor-targeted accumulation of 13.1%ID/g at 24 h post-administration.

(3) The selected SMDC-$Gd_4$ was practically used as a contrast agent in $T_1$-weighted MRI for cancer diagnosis, showcasing a substantial contrast enhancement effect on tumor tissues at a safe dosage.

(4) The development potential of SMDC-$Gd_4$ was demonstrated in Gd-NCT for cancer post-MRI diagnosis, manifesting a significant inhibitory effect on tumor growth.

# Achievement

(1) Gao S, Miura Y, Sumiyoshi A, Ohno S, Ogata K, Nomoto T, Matsui M, Honda Y, Suzuki M, Iiyama M, Osada K, Aoki I, Nishiyama N. Self-folding macromolecular drug carriers for cancer imaging and therapy. Advanced Science, 2023, DOI: 10.1002/advs.202304171.

(2) Grant-in-Aid for JSPS Fellows-特別研究員(DC2)

# Acknowledgement

I would like to thank Prof. Miura and Prof. Nishiyama from the laboratory for chemistry and life science, Tokyo Institute of Technology for the guidance of my research and kindly help in my study and life in lab.

Thanks to Prof. Nomoto, Prof. Matsui, and Prof. Honda form the laboratory for chemistry and life science, Tokyo Institute of Technology, and Prof. Aoki, Prof. Osada, and Prof. Sumiyoshi from National Institute of Radiological Sciences, National Institutes for Quantum and Radiological Science and Technology for the kindly help in my experiments.

Thanks to my wife for her company, help, and encouragement, we will have a happy future I promise. Thanks to my parents for their care and financial support, I hope they can be happy, recover and stay healthy.